Scanning tunneling spectroscopy of semiconductor quantum-well structures

Simon Perraud

THESE

Présentée par

Simon PERRAUD

Pour obtenir le grade de

Docteur de l'Université Pierre et Marie Curie

Spécialité

Physique

Etude de puits quantiques semiconducteurs par microscopie et spectroscopie à effet tunnel

soutenue le 7 Décembre 2007

au Laboratoire de Photonique et de Nanostructures (Marcoussis)

devant le jury composé de

Prof. Yves Guldner (Université Pierre et Marie Curie, Paris), président

Dr. Bruno Grandidier (IEMN, CNRS, Lille), rapporteur

Dr. Stefan Fölsch (Paul Drude Institute, Berlin, Germany), rapporteur

Dr. Gerald Bastard (Ecole Normale Supérieure, Paris)

Dr. Paul Voisin (LPN, CNRS, Marcoussis)

Dr. Zhao-Zhong Wang (LPN, CNRS, Marcoussis), directeur de thèse

Dr. Kiyoshi Kanisawa (NTT Basic Research Laboratories, Atsugi, Japan), co-directeur de thèse

Scanning tunneling spectroscopy of semiconductor quantum-well structures

Simon Perraud[1,2]

[1] *NTT Basic Research Laboratories, NTT Corporation, Atsugi, Kanagawa 243-0198, Japan*

[2] *Laboratoire de Photonique et de Nanostructures, CNRS, 91460 Marcoussis, France*

December 10, 2007

Abstract. Low-temperature scanning tunneling spectroscopy (STS) under ultrahigh vacuum was used to investigate $In_{0.53}Ga_{0.47}As/In_{0.52}Al_{0.48}As$ quantum-well (QW) structures, grown by molecular beam epitaxy on lattice-matched InP(111)A substrates. In a first part, as a preliminary step, the (111)A epitaxial surface of n-type $In_{0.53}Ga_{0.47}As$ was studied by STS. It was found that the surface Fermi level is located in the conduction band, close to the bulk Fermi level, and can be partially controlled by varying the n-type impurity density in the bulk. This result was confirmed by determining the conduction-band dispersion relation at the surface. Such partial unpinning of the surface Fermi level indicates a low density of acceptorlike surface states. It was proposed that these states originate from native point defects located at the surface. In a second part, based on the results of the first part, (111)A-oriented $In_{0.53}Ga_{0.47}As$ surface QWs grown on top of $In_{0.52}Al_{0.48}As$ barriers were studied by STS. The STS measurements were performed at the (111)A epitaxial surface of the $In_{0.53}Ga_{0.47}As$ QW, in order to probe with nanometer-scale resolution the in-plane spatial distribution of electronic local density of states. It was confirmed that electron subbands are formed in the QW, and that the electron density in the QW can be varied owing to the partial unpinning of the surface Fermi level. It was found that a phenomenon of percolation of localized states occurs in each subband tail, due to the presence of a disorder potential in the QW. The percolation thresholds were determined by using a semiclassical model. The origin of the disorder potential was ascribed to the random distribution of the native point defects at the QW surface. It was also found that a bound state splits off from each subband minimum in the vicinity of a positively charged native point defect. Both the binding energy and the Bohr radius of the bound states could be directly determined. Moreover, it was shown that the binding energy and the Bohr

radius are functions of the QW thickness, in quantitative agreement with variational calculations of hydrogenic impurity states.

Keywords. Scanning tunneling microscopy, scanning tunneling spectroscopy, molecular beam epitaxy, III-V compound semiconductor, Fermi level pinning, electronic surface state, quantum well, Anderson localization, percolation, hydrogenic impurity, binding energy, Bohr radius.

Résumé. Des puits quantiques à base d'hétérostructures $In_{0.53}Ga_{0.47}As/In_{0.52}Al_{0.48}As$, fabriqués par épitaxie par jets moléculaires sur substrats $InP(111)A$, sont étudiés par microscopie et spectroscopie à effet tunnel à basse température et sous ultra-vide. La première partie est consacrée à une étude de la surface épitaxiée $(111)A$ de $In_{0.53}Ga_{0.47}As$ de type n. Il est découvert que le niveau de Fermi de surface est positionné dans la bande de conduction, à proximité du niveau de Fermi de volume, et peut être partiellement contrôlé en variant la concentration d'impuretés de type n dans le volume. Ce résultat est confirmé en déterminant la relation de dispersion de la bande de conduction en surface. Un tel dépiégeage partiel du niveau de Fermi de surface indique que la densité d'états de surface accepteurs est faible. Il est proposé que ces états proviennent de défauts ponctuels natifs localisés à la surface. La deuxième partie, basée sur les résultats obtenus dans la première partie, est consacrée à une étude de puits quantiques $In_{0.53}Ga_{0.47}As$ de surface, déposés sur des barrières $In_{0.52}Al_{0.48}As$ selon la direction $(111)A$. Les mesures sont conduites sur la surface épitaxiée $(111)A$ du puits quantique $In_{0.53}Ga_{0.47}As$, de manière à pouvoir sonder à l'échelle du nanomètre la distribution de densité locale d'états électroniques dans le plan du puits quantique. Il est confirmé que des sous-bandes électroniques sont formées dans le puits quantique, et que la concentration d'électrons dans le puits peut être contrôlée du fait du dépiégeage partiel du niveau de Fermi de surface. Il est découvert qu'un phénomène de percolation d'états localisés survient dans la queue de chaque sous-bande, ce qui indique la présence d'un potentiel désordonné dans le puits quantique. Les seuils de percolation sont déterminés en utilisant un modèle semi-classique. L'origine du potentiel désordonné est attribuée à une distribution aléatoire des défauts ponctuels natifs à la surface du puits quantique. Il est également découvert qu'un état lié apparaît au bas de chaque sous-bande à proximité d'un défaut ponctuel natif de type donneur. L'énergie de liaison et le rayon de Bohr des états liés peuvent être directement déterminés. De plus, il est démontré que

l'énergie de liaison et le rayon de Bohr sont fonctions de l'épaisseur du puits quantique, en accord quantitatif avec des calculs variationnels d'impuretés dans le modèle de l'atome d'hydrogène.

Mots-clés. Microscopie à effet tunnel, spectroscopie à effet tunnel, épitaxie par jets moléculaires, semiconducteur III-V, piégage du niveau de Fermi, état électronique de surface, puits quantique, localisation d'Anderson, percolation, impureté, énergie de liaison, rayon de Bohr.

Contents

1 Introduction

Research in the field of two-dimensional electronic systems (2DES) [1] is at the cutting edge of modern solid-state physics. From the viewpoint of technological applications, 2DES form the core of field-effect transistors [2], which are the workhorses of today's electronic industry. From the viewpoint of fundamental science, the study of 2DES has led to the discovery of fascinating quantum-mechanical phenomena, including weak localization [3], integer quantum Hall effect [4], and fractional quantum Hall effect [5].

The most successful method to create 2DES is to employ semiconductor heterostructures [6–9] fabricated by molecular beam epitaxy (MBE) [10–13]. Using MBE growth, layers with different chemical composition can be superimposed on each other with atomically abrupt interfaces. Applying this technique to semiconductors, in particular III-V compound materials, the band structure along the growth direction can be tailored in a nearly arbitrary way [14]. In such artificial semiconductor heterostructures, it is possible to realize 2DES by restricting electron motion to a plane perpendicular to the growth direction. Two main types of semiconductor heterostructures allow the formation of 2DES, namely single-interface structures (figure 1.1) and quantum-well (QW) structures (figure 1.2).

The interest in 2DES formed in semiconductor heterostructures grown by MBE is two-fold. First, the electron mobilities are extremely high [15, 16]. This results from the purity of semiconductor materials and the smoothness of heterointerfaces obtained by MBE, as well as from the use of the technique of modulation doping [17]. Second, the main parameters of the system can be readily controlled, including quantum confinement along the growth direction (tuned by varying the thickness of grown layers) and electron density (tuned by modulation doping [17] or by an external electric field [18–23]). Owing to these remarkable properties, semiconductor heterostructures are employed in today's highest-frequency field-effect transistors [24, 25], and are indispensable for exploring the complex properties of 2DES [16].

Crystalline defects play a crucial role in solids in general and in 2DES in particular. In order to fully understand the influence of defects on the properties of 2DES, analytical tools with high

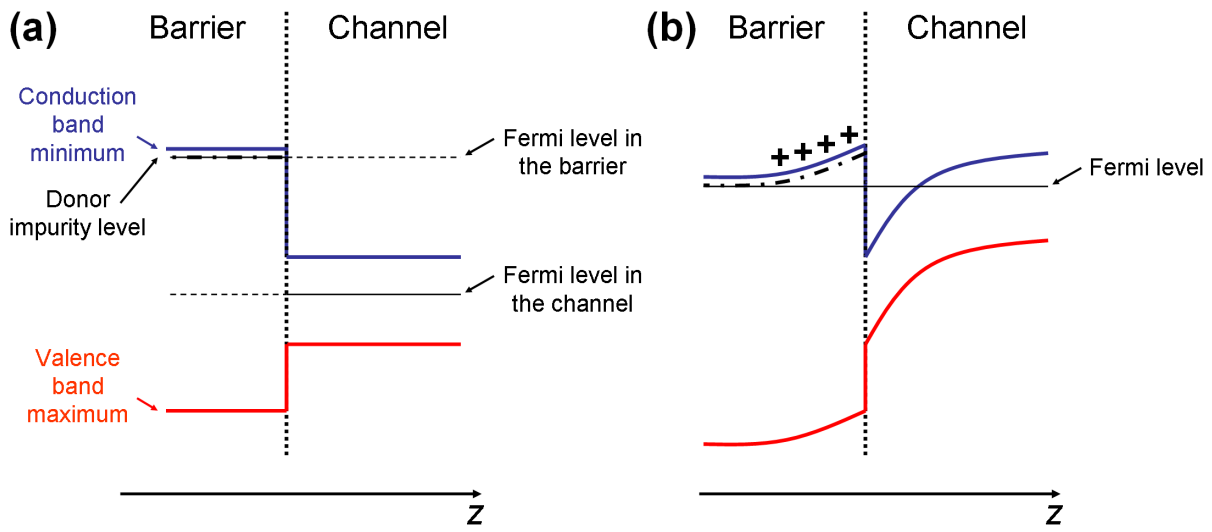

Figure 1.1: (Color) Formation of 2DES in semiconductor heterostructures: band diagrams along the growth direction z for a single-interface structure. The wide-gap layer (called the barrier) is doped with donor impurities, while the narrow-gap layer (called the channel) is undoped. Since the conduction-band minimum in the channel lies lower in energy than the impurity level in the barrier, the impurities in the barrier are ionized and the electrons are transferred to the conduction band in the channel. The conduction-band electrons in the channel are pulled against the potential step at the interface with the barrier, due to the electric field of the ionized donors from which the electrons came. Thus the conduction-band electrons in the channel are confined along z by a triangular potential. The fact that only the barrier is doped while the channel is undoped is referred to as modulation doping [17]. Modulation doping allows to spatially separate the free electrons from their parent donor impurities, leading to high electron mobilities in the channel. **(a)** Out of equilibrium (before the transfer of electrons from the barrier to the channel). **(b)** At equilibrium (after the transfer of electrons from the barrier to the channel).

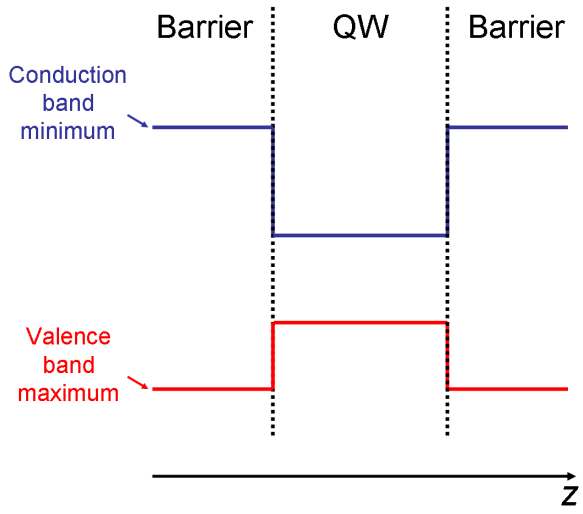

Figure 1.2: (Color) Formation of 2DES in semiconductor heterostructures: band diagram along the growth direction z for a QW structure. A narrow-gap layer (called the QW) is grown between two wide-gap layers (called the barriers). Conduction-band electrons in the QW are bounded on each side by the potential step at the interface with the barrier. Thus conduction-band electrons in the QW are confined along z by a rectangular potential.

spatial resolution are necessary. In this respect, scanning tunneling spectroscopy (STS) [26–30] is one of the most powerful methods. Using STS, it is possible to measure the electronic local density of states (LDOS) at solid surfaces with atomic-scale resolution. In other words, STS allows to map in real space the electron wave functions. Thus STS appears as an ideal technique for characterizing the local properties of 2DES in the vicinity of defects. Since STS is a surface-sensitive technique, the 2DES to be investigated should be located as close as possible to a solid surface.[1] So far, STS measurements of 2DES have been conducted mainly on metal surface states [55–67], metal thin films [68,69], $ErSi_2$ layers [70–73], highly oriented pyrolitic graphite surfaces [74–77], and the electron accumulation layer at InAs surfaces [78–81]. Several aspects of the physics of 2DES in the presence of defects have been investigated, e.g., scattering interferences [55–60,62–64,67,69–72,74,75,78,79],

[1]This contrasts with the well-known case of conventional semiconductor heterostructures, where the 2DES are buried several 10 nanometers below the epitaxial surface. Over the last decade, the buried 2DES formed in such semiconductor heterostructures have been characterized at sub-micrometer scales by various low-temperature scanning probe microscopy techniques, including near-field scanning optical microscopy [31, 32], scanning gate [33–46], subsurface charge accumulation imaging [47–51], and scanning single-electron transistor [52–54].

impurity bound states [61, 65, 66, 73], electron localization by a disorder potential [81], and the quantum Hall regime [76, 77, 80].

However, STS has been seldom used for studying 2DES formed in semiconductor heterostructures, in spite of their importance for physics and technology. In a very recent work [82], STS measurements were performed at the *cleaved* surface of QW structures, in order to probe the cross-sectional spatial distribution of LDOS [figures 1.3(a) and (b)]. Another interesting possibility is to perform STS measurements at *epitaxial* surfaces of QW structures, in order to probe the in-plane spatial distribution of LDOS [figure 1.3(c)].

In this dissertation, we report low-temperature STS measurements under ultrahigh vacuum (UHV) at the (111)A epitaxial surface of $In_{0.53}Ga_{0.47}As/In_{0.52}Al_{0.48}As$ QW structures, grown by MBE on lattice-matched InP substrates. The outline is as follows.

- In section 2 the experimental procedures are described, including the MBE growth of III-V compound semiconductor thin films and the low-temperature STS measurements.

- As a preliminary step, section 3 focuses on the electronic properties of the $In_{0.53}Ga_{0.47}As$(111)A epitaxial surface.

- Based on the results of section 3, section 4 presents a study of two-dimensional electronic states in (111)A-oriented $In_{0.53}Ga_{0.47}As$ surface QWs grown on top of $In_{0.52}Al_{0.48}As$ barriers.

- In section 5, the main results reported in this dissertation are highlighted and future experiments are proposed.

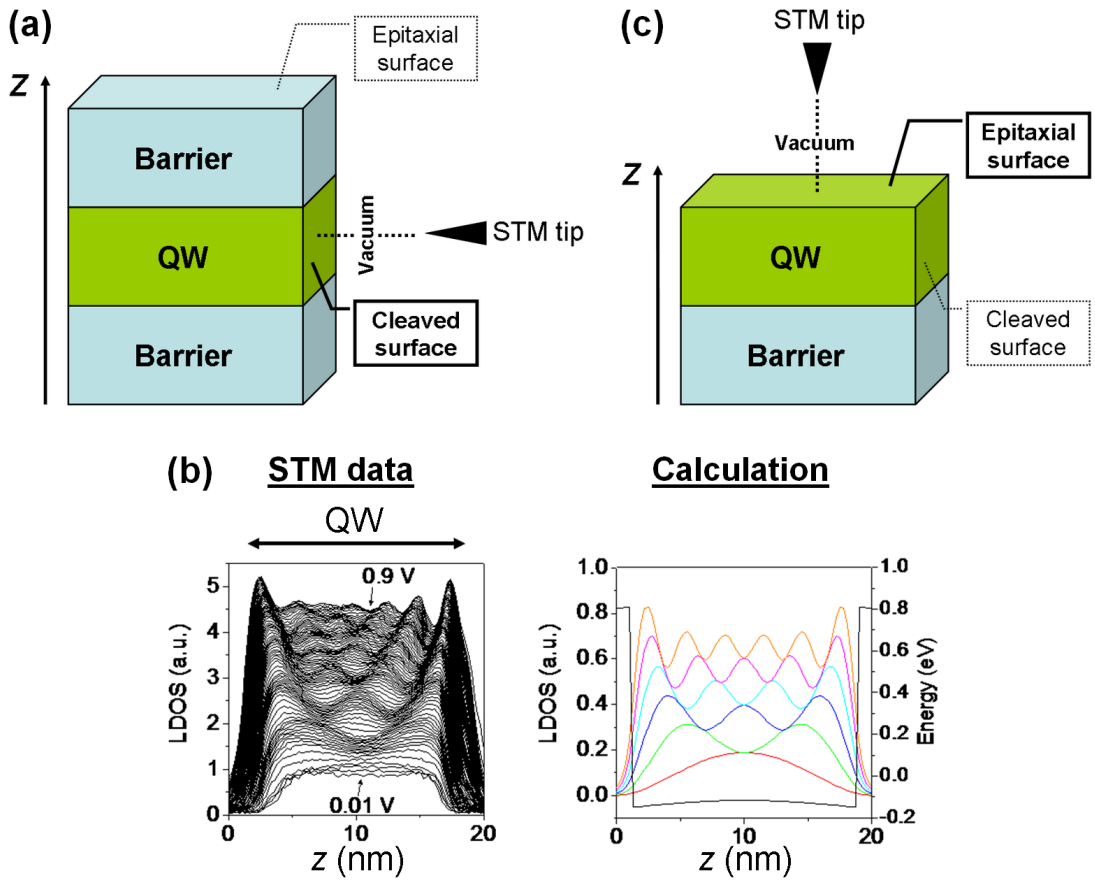

Figure 1.3: (Color) STS study of 2DES formed in semiconductor QW structures. **(a)** STS measurements at *cleaved* surfaces of QW structures, in order to probe the cross-sectional spatial distribution of LDOS. This is the type of measurement performed in Ref. [82], where the structure consists of an InAs QW between two GaSb barriers. **(b)** Cross-sectional spatial distribution of LDOS for a 17-nm-thick InAs QW between two 23-nm-thick GaSb barriers [82]: STS data and calculation. **(c)** STS measurements at *epitaxial* surfaces of QW structures, in order to probe the in-plane spatial distribution of LDOS. Vacuum plays the role of one of the two barriers, hence the configuration is referred to as a surface QW structure. This is the type of measurement reported in this dissertation, where the structure consists of a (111)*A*-oriented $In_{0.53}Ga_{0.47}As$ surface QW grown on top of an $In_{0.52}Al_{0.48}As$ barrier.

2 Experimental procedures

2.1 Overview of the experimental set-up

Experiments were carried out in a multi-chamber UHV system, shown in figure 2.1. It consists of four connected UHV chambers [process, optical analysis, MBE, and low-temperature scanning tunneling microscope (STM)], plus an entry lock. The MBE system was employed for growing III-V compound semiconductor thin films. After the growth, samples were transferred under UHV from the MBE chamber to the low-temperature STM chamber. Thus STM measurements could be performed on the clean epitaxial surfaces of the thin films.

The entry lock allows to load samples into the UHV system without breaking vacuum. It is equipped with a rotary pump and a turbomolecular pump, which enable to reach a pressure lower than 1×10^{-7} Torr before transferring samples to the UHV chambers.

The process chamber and the optical analysis chamber are dedicated for sample cleaving and photoluminescence measurements, respectively. Both chambers are equipped with a ion-getter pump and a titanium sublimation pump, and the base pressure is below 5×10^{-10} Torr. These two chambers were not directly used in this work.

The MBE chamber is equipped with a cryopump, a ion-getter pump and a titanium sublimation pump, along with a liquid nitrogen cryopanel. The base pressure is within the range of 10^{-10} Torr.

The low-temperature STM chamber is equipped with a ion-getter pump and a titanium sublimation pump, and the base pressure is within the range of 10^{-11} Torr.

Bellows with a resonance frequency lower than 10 Hz are installed between the optical analysis chamber and the process chamber, and between the process chamber and the STM chamber. The bellows help reducing the mechanical vibrations coming from the MBE chamber, and thus improve the signal on noise ratio during STM measurements.

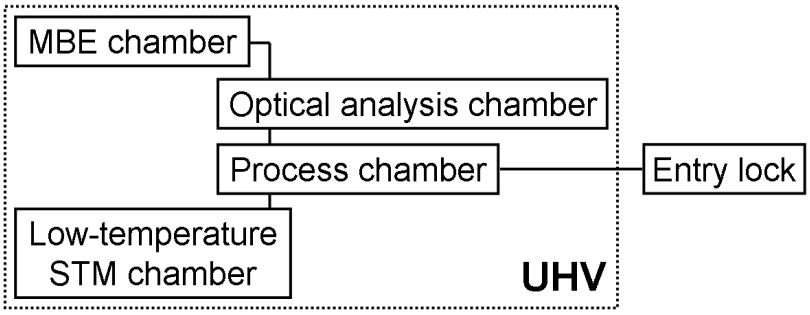

Figure 2.1: Experimental set-up: UHV system consisting of four connected chambers (process, optical analysis, MBE, and low-temperature STM), plus an entry lock. The MBE system was employed for growing III-V compound semiconductor thin films. After the growth, samples were transferred under UHV from the MBE chamber to the low-temperature STM chamber. Thus STM measurements could be performed on the clean epitaxial surfaces of the thin films.

2.2 Molecular beam epitaxy system

2.2.1 Basic principles of molecular beam epitaxy

MBE, developed by Arthur and Cho at Bell Laboratories in the early 1970s, is a technique for growing monocrystalline thin films under UHV [10–13]. During MBE growth, the constituent elements of the thin film are evaporated from separated sources. The thermal beams of atoms or molecules leaving the sources travel without collision in UHV, toward a heated single-crystal substrate, on top of which the monocrystalline thin film grows monolayer by monolayer. MBE is a versatile technique; it was first used to grow III-V compound semiconductors, but it is also able to fabricate thin films of II-VI compound semiconductors, elemental semiconductors, insulators and metals. The main advantages of MBE are the followings:

- The use of an UHV environment and of high purity source materials allow to achieve a low unintentional impurity concentration in the grown thin films (typically in the range of 10^{14} cm^{-3} for GaAs).

- Since the growth rate is slow (about one monolayer per second) and beam controllers consist of fast action shutters (operational time shorter than one second), the thickness of grown layers can be controlled with an accuracy of less than one monolayer. Therefore, layers with

different chemical compositions can be superimposed on each other, with atomically abrupt interfaces. Moreover, the substrate temperature during growth (typically between 550°C and 650°C for GaAs) is sufficiently low to consider diffusion between layers as negligible.

- Preparing clean surfaces in UHV, an indispensable step in the field of surface science, can be readily achieved by MBE. Other methods to obtain clean surfaces in UHV include ion sputtering and cleaving *in situ*. However, ion sputtering may produce defects, and cleaving is limited to particular cleavage planes [for example, the (111) plane for Si and the (110) plane for III-V compound semiconductors with a zinc-blende structure], whereas MBE is able to achieve many crystallographic orientations.

2.2.2 Description of the growth chamber

The MBE growth chamber used in this work was an Anelva system, dedicated for growing III-V compound semiconductor thin films. A valved cracker cell was used for arsenic (purity of 7 N, i.e., 99.99999%). Individual effusion cells with pyrolitic boron nitride crucibles were used for aluminum (5 N), gallium (8 N), indium (7 N) and silicon. Between growths, the Al, Ga, In and Si cells were idled at 300°C; the As crucible and the As cracker were idled at 200°C and 300°C, respectively. Before growths, sources were outgassed during one hour, at 340°C for the As crucible, 800°C for the As cracker, and 50°C more than the temperature during growth for the effusion cells. The As beam equivalent pressure was measured by an ionization gauge positioned behind the substrate holder. The substrate holder was heated by radiation and its temperature was monitored by a W-Re thermocouple located in a black-body enclosure behind the holder. The sample surface temperature was measured through a viewport by an infrared pyrometer. The crystallographic structure of the sample surface was characterized by 15-keV reflection high-energy electron diffraction (RHEED).

2.2.3 Preparation of substrates

The substrates employed in this work were semi-insulating InP single crystal wafers, grown by the liquid encapsulated Czochralski method. Two different crystal orientations were employed, namely (001) and (111)A.

The InP substrates were degreased and etched in a commercial solution (Semico 23 clean from

Furuuchi Chemical) during 3 min, rinsed in deionized water during 5 min and blown dry with filtered nitrogen gas. The substrates were then bounded on a molybdenum plate with indium solder on the back. Indium soldering ensures uniform temperature across the substrate during MBE growth. The molybdenum plate was mounted on a molybdenum block and loaded into the UHV system. The block is dedicated for the MBE chamber, the optical analysis chamber and the process chamber, while the plate is dedicated for the STM chamber.

Before MBE growth, native oxides formed on the substrate surface have to be removed by thermal desorption under UHV. In the case of InP, surface oxides are desorbed at a temperature of 500°C, which largely exceeds the congruent sublimation temperature of 363°C [83]. Therefore, InP substrates have to be stabilized by a group V element flux to avoid the formation of In droplets. It has been shown that InP(001) substrates can be stabilized by a flux of P_2 or P_4 molecules [84], but the residual pressure of phosphorus molecules is undesirable for the MBE growth of materials which do not contain phosphorus. It has also been reported that surface oxides on InP(001) substrates can be desorbed by heating to 500-530°C in a stabilizing As_4 flux of 10^{-6}-10^{-5} Torr [85]. Since the surface oxide desorption is done at a temperature much higher than the congruent sublimation temperature, surface P atoms are desorbed and replaced by the impinging As atoms [86, 87], which leads to the formation of a pseudomorphic InAs overlayer on the InP substrate. The exchange reaction between P and As is limited to the topmost layers. At 500°C, the InAs overlayer thickness ranges between 1.5 monolayers [87] and 2 monolayers [86]. It has been found that the InAs overlayer forms at the top of the surface oxides [88]. Therefore the oxide desorption rate is strongly reduced, and the complete removal of the oxide requires a temperature of at least 520°C.

In this work, a technique similar as that proposed in Ref. [85] was employed. Surface oxides on (001)- and (111)*A*-oriented InP substrates were desorbed by annealing during 10 min at 520°C under a stabilizing As_4 flux. Before annealing, the RHEED pattern showed a halo character, indicating the presence of amorphous surface oxides. After annealing, the RHEED pattern usually showed streaks, as expected for a clean and flat crystalline surface.

2.2.4 Calibration of fluxes

The MBE growth of stoichiometric films of GaAs, AlAs, InAs and their alloys was carried out under excess As_4 flux, the growth rate being simply determined by the fluxes of group III elements [10–12].

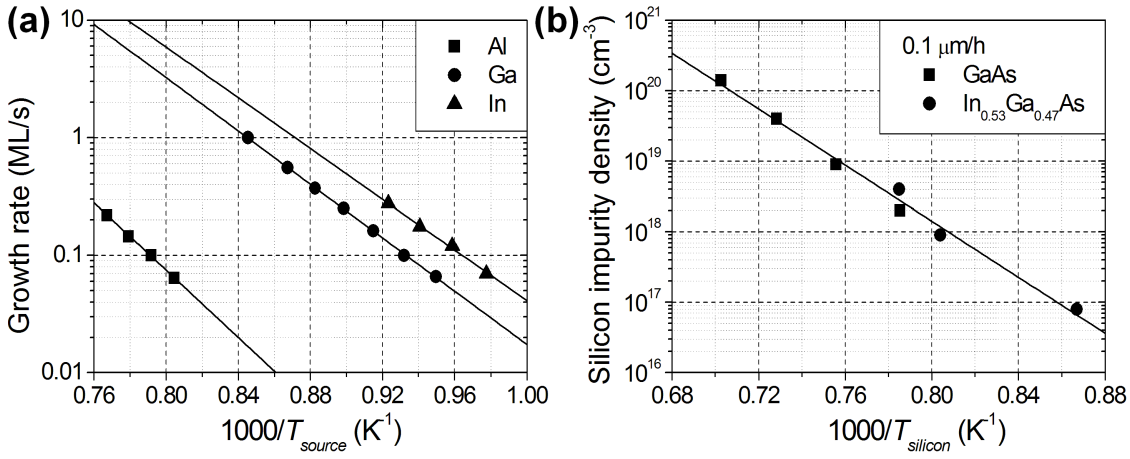

Figure 2.2: Calibration of fluxes for MBE growth. **(a)** Growth rate measured by RHEED intensity oscillations as a function of source temperature T_{source}, for aluminum (squares), gallium (circles) and indium (triangles). Linear fits of the experimental data (solid lines) are also shown. **(b)** Silicon impurity density incorporated in grown thin films, measured by SIMS depth profiling as a function of silicon source temperature $T_{silicon}$. The silicon impurity density is given for a growth rate of 0.1 μm/h. SIMS depth profile analysis was performed on GaAs thin films grown on GaAs(001) substrates at a substrate temperature of 550°C (squares), and on $In_{0.53}Ga_{0.47}As$ thin films grown on lattice-matched InP(111)A substrates at a substrate temperature between 450°C and 500°C (circles). A linear fit of the experimental data (solid line) is also shown.

The growth rate for each group III element was measured by RHEED intensity oscillations [10–12] as a function of source temperature [figure 2.2(a)]. For measuring the growth rate for aluminum and gallium, AlAs and GaAs thin films were grown on GaAs(001) substrates at a substrate temperature of 550°C, respectively. For measuring the growth rate for indium, InAs thin films were grown on InAs(001) substrates at a substrate temperature of 430°C. A CCD camera was employed to record the intensity of the specular beam of the RHEED pattern as a function of growth time. During the growth, the surface cycles between smooth and atomically rough, with a period corresponding to the time to grow a monolayer. Since the intensity of diffracted beams depends on the roughness of the surface, measuring the period of the intensity oscillations during the growth gives directly access to the growth rate.

The silicon impurity density incorporated in the grown thin films was determined by secondary-ion mass spectrometry (SIMS) depth profiling [89] as a function of silicon source temperature

[figure 2.2(b)]. SIMS depth profile analysis was performed on GaAs thin films grown on GaAs(001) substrates at a substrate temperature of 550°C, and on $In_{0.53}Ga_{0.47}As$ thin films grown on lattice-matched InP(111)A substrates at a substrate temperature between 450°C and 500°C. No significant silicon segregation effect at the surface was observed in the depth profiles.

2.3 Low-temperature scanning tunneling microscope

2.3.1 Basic principles of scanning tunneling microscopy

The STM, invented by Binnig and Rohrer at IBM Zürich Laboratories in the early 1980's, allows to investigate in real space the surfaces of electrically conductive materials (conductors, semiconductors or superconductors) [26–30]. The basic principle of the STM is the following. A metallic probe tip is brought to a few Å of the sample surface, and a bias voltage applied between the tip and the sample causes a tunneling current to flow. Measuring the tunneling current provides local information about the topographic and electronic structures of the surface.

The STM can be used for so-called constant-current topographic measurements. While the probe tip scans the (x, y) plane of the sample surface at a constant sample voltage U, the tunneling current is kept constant by using a feedback loop which adjusts the vertical position z of the tip. A topographic image represents z as a function of (x, y). The tunneling current depends mainly on two parameters: tip-sample separation and LDOS at the sample surface [equation (A.12)]. Thus a topographic image not only provides information about the topography of the surface, but also about its electronic properties.

The STM can also be employed for so-called spectroscopic measurements, referred to as STS. The tunneling current I is recorded as a function of the sample voltage U, with the position (x, y, z) of the tip fixed, the current feedback loop being disengaged. The differential conductance dI/dU at U is proportional to the LDOS at the sample surface at energy $+eU$ (where e is the elementary charge and U=0 corresponds to the sample Fermi level), if the tip-sample separation is constant [equation (A.14)]. Thus STS provides a measurement of the LDOS at the sample surface as a function of energy and position.

The spatial resolution of the STM is extremely high, owing to the exponential decay of electron

wave functions in classically forbidden regions. Specifically, the lateral resolution is sufficient for characterizing atomic-size structures, and the vertical resolution during topographic measurements is better than 1 pm for state-of-the-art instruments. The resolution is limited by the probe tip condition and mechanical vibrations. A sharp and stable tip, as well as a low level of mechanical noise, are key requirements for high-resolution STM measurements.

2.3.2 Description of the scanning tunneling microscope

The STM used in this work was an Omicron LT-STM [90], an instrument operating under UHV and at low temperature (5 K). The UHV environment is crucial for reliable STM investigations on semiconductor surfaces, which are sensitive to oxidation and contamination. The low temperature offers several advantages, such as: increased mechanical stability, increased energy resolution for STS, and increased coherence length of electron wave functions.

Let us briefly describe the design of the Omicron LT-STM. More details can be found in Ref. [90]. The UHV chamber of the LT-STM contains the STM stage, the vibration isolation elements, and the cryogenic equipment (figure 2.3).

The cryogenic equipment consists of two concentric bath cryostats. The inner cryostat, filled with about four liters of liquid helium, is used to cool down the STM stage. The outer cryostat, filled with about four liters of liquid nitrogen, serves for shielding. The STM stage and the vibration isolation elements are mounted below the liquid helium cryostat and surrounded by a radiation shield made of two concentric copper cups. The inner cup and the outer cup are screwed to the liquid helium cryostat and the liquid nitrogen cryostat, respectively. Both copper cups have three windows for optical access, and one window for changing sample plates and probe tips. The time between liquid helium refills is typically 20 h.

The vibration isolation is realized by using both spring suspension (the STM stage is suspended by three soft springs, with a resonance frequency of about 2 Hz) and eddy-current damping (the STM stage is surrounded by a ring of copper plates, which come down between permanent magnets fixed at the inner copper cup). During measurements, the STM stage is hanging free, held vertically by the suspension springs and horizontally by the eddy-current damping. Between measurements, the STM stage can be pressed against the liquid helium cryostat in order to quickly reach low temperatures. In this work, the root mean square of mechanical noise measured at 5 K during

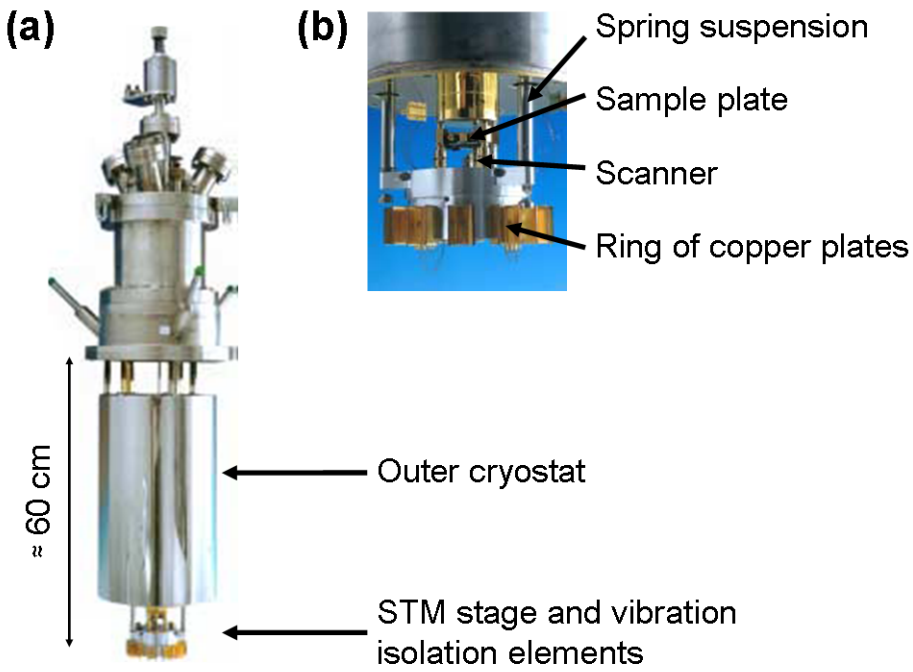

Figure 2.3: (Color) Omicron LT-STM [90]. **(a)** Picture showing the whole LT-STM. **(b)** Picture showing the STM stage and the vibration isolation elements.

constant-current topographic measurements was between 1 and 2 pm.

The STM stage includes the sample plate, the probe tip, the scanner and the piezo motor. The scanner, used for the fine movement of the tip during measurements, consists of a single piezo tube. At room temperature, the maximum scan range is about 10×10 μm^2, with a z-travel of about 1 μm. At 5 K, the maximum scan range is about 1.8×1.8 μm^2, with a z-travel of about 0.2 μm. The piezo motor, employed for a coarse positioning of the scanner before measurements, is based on a slip/stick effect: sliders, magnetically coupled to shear piezos driven in a fast/slow sequence, are transported during the slow movement of the piezos and slip during the fast movement. The maximum coarse movement is about 5×5 mm^2, with a z-travel of about 10 mm.

2.3.3 Lock-in technique

In this work, the tunneling differential conductance dI/dU was often recorded by using a lock-in technique, in order to increase the signal on noise ratio. Specifically, a sinusoidal modulation (U_{mod} = 10 mV peak-to-peak, f_{mod} = 700 Hz) was added to the sample voltage, and dI/dU was measured through a lock-in amplifier.

When the sinusoidal modulation was added to the sample voltage, a capacitive coupling between the sample voltage wire and the tunneling current wire led to a parasitic signal in the tunneling current. This cross-talk signal was compensated before feeding the lock-in amplifier, by superimposing on the tunneling current a sinusoidal signal at the frequency of the modulation, with an appropriate amplitude and phase.

2.3.4 Preparation of probe tips

Commercial probe tips from Omicron were employed in this work. The tips are made from tungsten wires prepared by vacuum annealing and electrochemical etching.

Before measurements, tips were cleaned *in situ* by applying pulsed high voltages (typically U = +10 V during about 1 s). The quality of tips was checked by STM topographic images (obtaining the resolution of atomic-scale features) and STS measurements (obtaining the expected band gap for the semiconductor material under investigation).

3 Electronic properties of the $In_{0.53}Ga_{0.47}As(111)A$ epitaxial surface

3.1 Background and motivation

The main goal of this work is to study electronic states in (111)A-oriented $In_{0.53}Ga_{0.47}As$ surface QWs. Thus, as a preliminary step, it is highly desirable to investigate in detail the electronic properties of the $In_{0.53}Ga_{0.47}As(111)A$ surface.

In this section, we report STS measurements at the (111)A epitaxial surface of $In_{0.53}Ga_{0.47}As$, grown by MBE on lattice-matched InP substrates. We focus on three important points:

- **Fermi level position at the $In_{0.53}Ga_{0.47}As(111)A$ surface**. In the bulk of a semiconductor, the Fermi level position can be precisely tuned by impurity doping [2]. However, the Fermi level position at a semiconductor surface depends not only on bulk doping, but also on electronic surface states (appendix B). In particular, in the case of a high density of surface states, the surface Fermi level is strongly pinned, i.e., the surface Fermi level remains almost constant over a wide range of impurity density in the bulk. A strong pinning of the Fermi level has been demonstrated, e.g., for the Si(111)-(2×1) [91,92], Si(001)-(2×1) [92,93], GaAs(001)-(2×4) [94,95], $In_{0.53}Ga_{0.47}As$(001)-(2×4) [96], and InAs(001)-(2×4) [97,98] surfaces. However, the case of the $In_{0.53}Ga_{0.47}As(111)A$ surface has not been studied so far. In section 3.3.1, we show that the Fermi level is partially unpinned at the (111)A surface of n-type $In_{0.53}Ga_{0.47}As$, i.e., the surface Fermi level can be partially controlled by varying the n-type impurity density in the bulk. Specifically, the surface Fermi level almost equals the bulk Fermi level at low values of the free-electron density n, while it is slightly below the bulk Fermi level at high values of n.

- **Conduction-band (CB) dispersion relation at the $In_{0.53}Ga_{0.47}As(111)A$ surface**. In section 3.3.2, we show that the CB dispersion relation measured by STS at the (111)A surface of n-type $In_{0.53}Ga_{0.47}As$ is well described by a two-band Kane model including nonparabolicity

effects (appendix C), with an effective mass at the CB minimum in agreement with a previously reported value of $0.041m_0$ [99]. In addition, we confirm the partial unpinning of the surface Fermi level.

- **Native point defects at the $In_{0.53}Ga_{0.47}As(111)A$ surface**. In section 3.3.3, we identify two types of native point defects at the $In_{0.53}Ga_{0.47}As(111)A$ surface, namely negatively charged and positively charged defects. We show that the density of negatively charged defects increases with increasing n, explaining quantitatively the n-dependence of the surface Fermi level position.

3.2 Experiment

Silicon-doped $In_{0.53}Ga_{0.47}As$ thin films were grown by MBE on lattice-matched semi-insulating InP substrates, at a growth rate of 0.1 ML/s and at a substrate temperature between 450°C and 500°C. The grown layers were in direct electrical contact with the STM sample plate, through indium deposited on the edges of the InP substrate before the growth. Both (001)- and (111)A-oriented InP substrates were used. The layer thicknesses were larger than 100 nm. During the growth, RHEED patterns indicated the (2×4) and (2×2) surface reconstructions for the (001) and (111)A orientations, respectively.

After the growth, epitaxial surfaces were kept during 3 min at the growth temperature in an As_4 flux. Substrate heating was then stopped. When the surface temperature passed below 430°C (detection limit of the infrared pyrometer), samples were rapidly taken out from the MBE chamber and transferred under UHV to the low-temperature STM chamber.

STM and STS measurements were performed at 5 K under UHV, on the clean epitaxial surfaces of the $In_{0.53}Ga_{0.47}As$ thin films. STM topographic images were acquired in the constant-current mode. For STS experiments, the tunneling current I was recorded as a function of sample voltage U, by positioning the probe tip at one point above the surface and disengaging the current feedback loop. Spectra of the differential conductance dI/dU as a function of U were obtained by numerically differentiating the I-U spectra. dI/dU spatial maps at fixed values of U were acquired simultaneously to constant-current STM topographic images, by directly recording dI/dU through a lock-in amplifier. We recall that dI/dU at U is proportional to the LDOS at the sample surface at

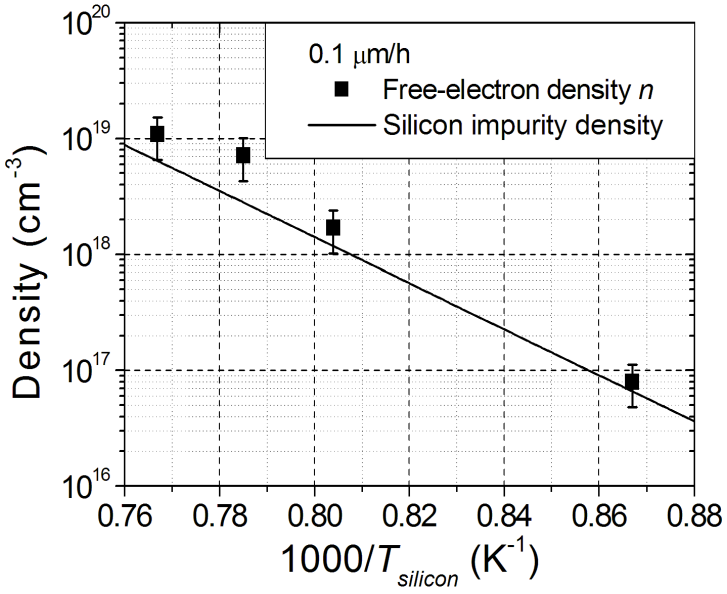

Figure 3.1: Free-electron density n in silicon-doped $In_{0.53}Ga_{0.47}As$ thin films grown on InP(111)A substrates (squares), measured by the Van der Pauw method at 4 K, as a function of silicon source temperature. The growth rate of the thin films is 0.1 μm/h. The silicon impurity density incorporated in the thin films (solid line), taken from figure 2.2(a), is also shown.

energy $+eU$ (where e is the elementary charge and $U = 0$ corresponds to the sample Fermi level), if the tip-sample separation is constant [equation (A.14)].

After the STM measurements, the epitaxial surfaces of the $In_{0.53}Ga_{0.47}As$ thin films grown on InP(111)A substrates were examined by scanning transmission electron microscopy. No dislocation line was observed, confirming that the InGaAs thin films are well matched to the InP substrates. However, stacking fault tetrahedrons [78, 100, 101] were found at the surface with a density of about 10 μm^{-2}. These defects may be formed during the cooling of the thin films after the growth.

The free-electron density n in the silicon-doped $In_{0.53}Ga_{0.47}As$ thin films grown on InP(111)A substrates was measured by the Van der Pauw method at 4 K. Ohmic contacts were made by alloying indium dots onto the grown layers at 420°C for 1 min in H_2 ambient. Results are shown in figure 3.1. It was found that all silicon impurities behave as donors for the doping levels used in this experiment, as expected from previous studies [102].

3.3 Results and discussion

3.3.1 Partial unpinning of the Fermi level

Fermi level position at the (001) surface

As a control experiment, let us first examine the Fermi level position with respect to the CB minimum at the (001) surface of n-type $In_{0.53}Ga_{0.47}As$. Figure 3.2(a) shows a STM topographic image of the (001) surface. Arsenic-dimer-vacancy rows resulting from the (2×4) reconstruction [103, 104] are observed, with a typical corrugation along the [110] direction of about 1 Å at the indicated tunneling parameters. The separation of these rows is about 1.6 nm, corresponding to the expected value of $2\sqrt{2}a$ (where $a = 0.586$ nm is the lattice constant of $In_{0.53}Ga_{0.47}As$).

Figure 3.2(c) shows a typical dI/dU spectrum acquired at the (001) surface. The measured band gap is about 0.8 eV, in agreement with previously reported values for $In_{0.53}Ga_{0.47}As$ at low temperature [99]. Thus, indium segregation effects at the surface [105] do not affect STS measurements. The surface Fermi level is found to be located close to midgap even at high doping, in agreement with a previous report [96].

The Fermi level position with respect to the CB minimum in the bulk was calculated as a function of the free-electron density n, by using Fermi-Dirac statistics (appendix B). The density of states in the CB was given by a two-band Kane model including nonparabolicity effects (appendix C). Results are shown in figure 3.3(a). It is found that the Fermi level at the (001) surface is well below the bulk Fermi level, a situation which corresponds to an upward band bending in the near-surface region, i.e., a positive space-charge layer. Overall charge neutrality requires that the charge carried by the surface states exactly compensate the space charge inside the semiconductor (appendix B). Thus, there are filled acceptorlike surface states at the (001) surface. These acceptorlike surface states are probably related to kinks in the arsenic-dimer-vacancy rows [94, 95] or step edges [106]. Furthermore, as it can be seen in figure 3.3(a), the Fermi level at the (001) surface is strongly pinned near midgap independently of n. Such strong pinning of the surface Fermi level around midgap means that there is a high density of acceptorlike surface states around midgap. Specifically, the situation can be understood in the framework of the Bardeen model (appendix B) by considering the distribution of acceptorlike surface states depicted in figure 3.3(b). The surface Fermi level

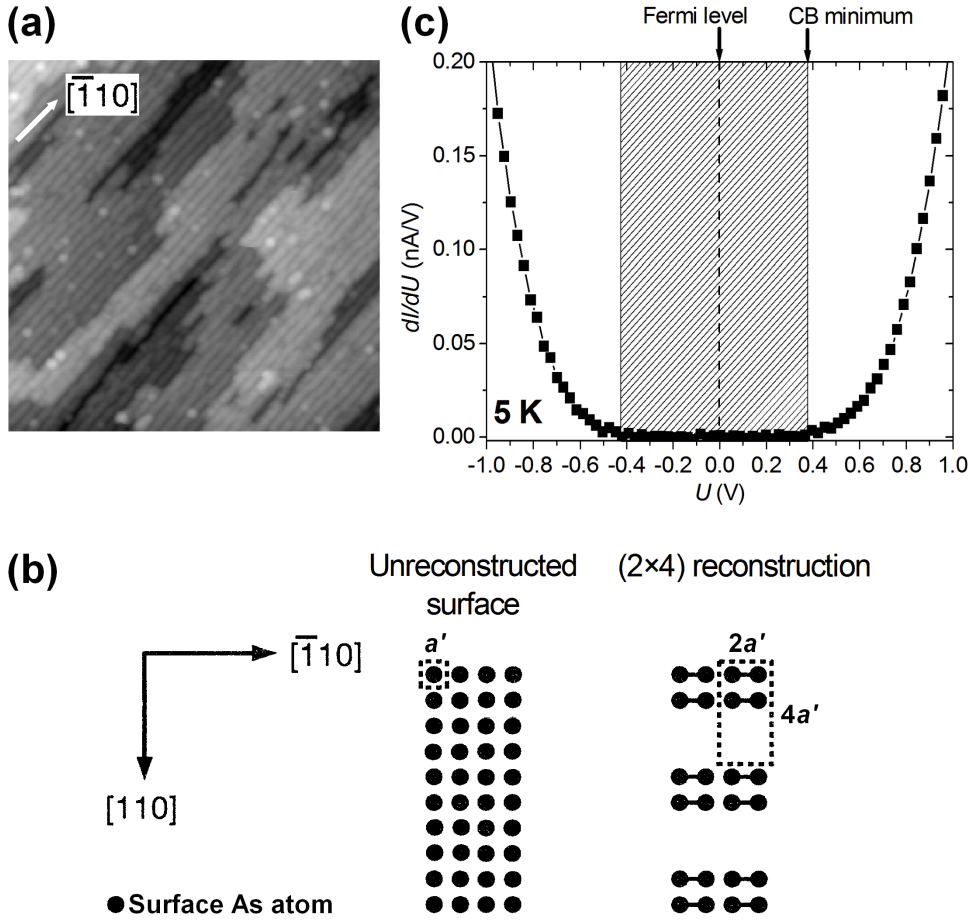

Figure 3.2: (001) surface of n-type $In_{0.53}Ga_{0.47}As$; $n = 2{\times}10^{18}$ cm^{-3}. **(a)** 67×67 nm^2 STM topographic image ($U = +2.5$ V; $I = 0.15$ nA). **(b)** Schematic of the unreconstructed (001) arsenic-rich surface and of the (2×4) reconstruction [103, 104]. a' denotes the lattice constant of the square unit cell of the unreconstructed (001) surface ($a' = \frac{a\sqrt{2}}{2}$, where a is the bulk lattice constant). **(c)** dI/dU spectrum. The Fermi level ($U = 0$) and the CB minimum are indicated. The hatched region represents the band gap.

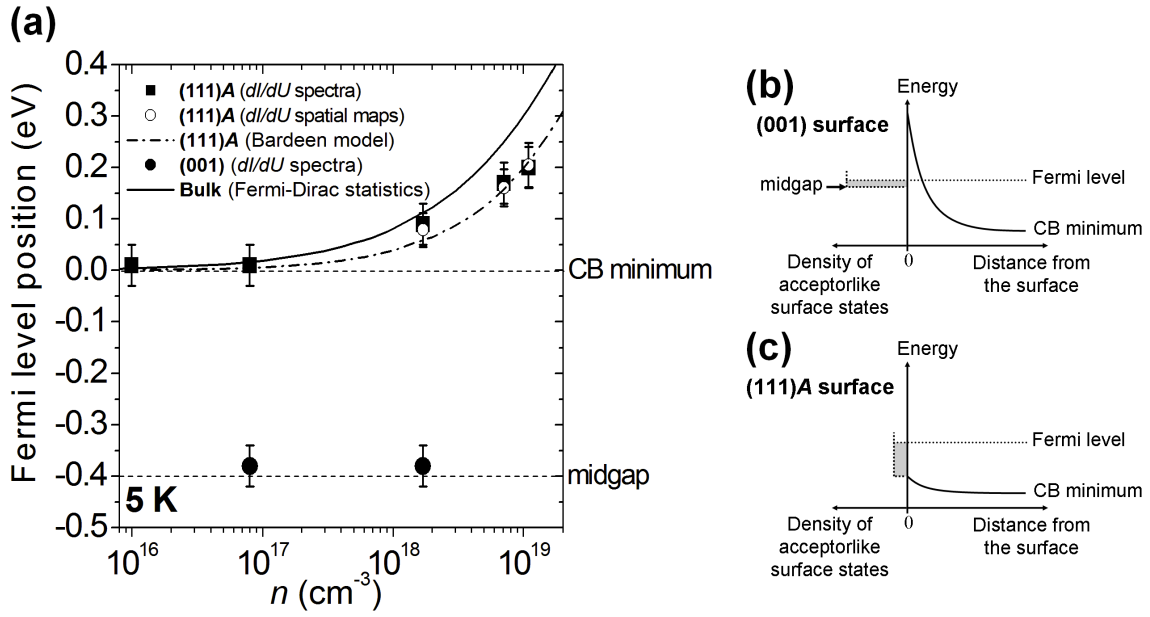

Figure 3.3: **(a)** Fermi level position with respect to the CB minimum at the (111)A surface of n-type $In_{0.43}Ga_{0.47}As$, determined from dI/dU spectra (black squares) and Fourier analysis of dI/dU spatial maps (white circles), and calculated by using the Bardeen model (appendix B) with a density of acceptorlike surface states in the CB of about 2×10^{13} cm^{-2}.eV^{-1} (dash-dotted line). Also shown are the Fermi level at the (001) surface determined from dI/dU spectra (black circles), and the bulk Fermi level calculated by using Fermi-Dirac statistics (appendix B) (solid line). **(b)** Schematic energy band profiles and acceptorlike surface state distributions in the Bardeen model, for high doping, at the (001) surface and **(c)** at the (111)A surface.

pinning within the 0.08 eV error bar corresponds to a density of acceptorlike surface states above midgap larger than 1×10^{14} cm^{-2}.eV^{-1}.

Fermi level position at the (111)A surface

Then, let us examine the Fermi level position with respect to the CB minimum at the (111)A surface of n-type $In_{0.53}Ga_{0.47}As$. Figure 3.4(a) shows a STM topographic image of the (111)A surface. Indium and gallium vacancies resulting from the (2×2) reconstruction [107, 108] are visible, with a typical corrugation along the ⟨110⟩ directions of about 0.1 Å at the indicated tunneling parameters. The separation of these vacancies is about 0.83 nm, corresponding to the expected value of $\sqrt{2}a$ (where $a = 0.586$ nm is the lattice constant of $In_{0.53}Ga_{0.47}As$).

It should be noted that the STM topographic image of figure 3.4(a) has a mottled appearance, with a typical corrugation of about 0.5 Å at the indicated tunneling parameters. Such a phenomenon has been observed in STM topography of InGaAs(110) cleaved surfaces [109], and is due to local inhomogeneities of the alloy composition. Bright and dark regions are believed to correspond to indium- and gallium-rich areas, respectively. The contrast has been ascribed to electronic effects [109] or strain effects [110]. The physical origin of the compositional inhomogeneities observed in figure 3.4(a) is presently unknown. These inhomogeneities could be the result of either random fluctuations [110] or a phase separation [111–113]. The mottled appearance is less clear in STM topographic images of the (001) surface [figures 3.2(a)], probably because the corrugation related to the (2×4) reconstruction is larger than that related to the compositional inhomogeneities.

Figures 3.4(c) and (d) show typical dI/dU spectra acquired at the (111)A surface. The measured band gap has the expected value of about 0.8 eV [99], similar to what is found at the (001) surface. However, in contrast with the case of the (001) orientation, the Fermi level at the (111)A surface lies in the CB. Specifically, the surface Fermi level is located near the CB minimum at low doping [figure 3.4(c)], while well above the CB minimum at high doping [figure 3.4(d)]. No significant difference in band gap or surface Fermi level position was observed between indium- and gallium-rich regions.

It is known that the presence of filled CB states in a semiconductor induces a nonzero signal in the band gap of dI/dU spectra (appendix A). Accordingly, we observe a nonzero signal in the band gap of dI/dU spectra measured at the (111)A surface [figures 3.4(c) and (d)], while we do not observe such signal at the (001) surface [figure 3.2(c)].

The Fermi level position at the (111)A surface was determined from dI/dU spectra for several values of n. Results are shown in figure 3.3(a). At low values of n, the Fermi level at the (111)A surface almost equals the bulk Fermi level, a situation which corresponds to flat bands in the near-surface region. At high values of n, the surface Fermi level is slightly below the bulk Fermi level, a situation which corresponds to an upward band bending, i.e., a positive space-charge layer. Overall charge neutrality requires that the charge carried by the surface states exactly compensate the space charge inside the semiconductor (appendix B). Thus, there are filled acceptorlike surface states at the (111)A surface. Furthermore, as it can be seen in figure 3.3(a), the surface Fermi level follows the bulk Fermi level very well. Such partial unpinning of the surface Fermi level means that the density of acceptorlike surface states is low. Specifically, the situation can be understood in

the framework of the Bardeen model (appendix B) by considering the distribution of acceptorlike surface states depicted in figure 3.3(c): acceptorlike surface states are almost absent in the band gap (thus the separation between the surface Fermi level and the bulk Fermi level is almost zero at low doping), but some are present in the CB (thus the number of filled acceptorlike surface states increases with n, meaning that the separation between the surface Fermi level and the bulk Fermi level increases with n). The dependence of the surface Fermi level position on n is well fitted by assuming a density of acceptorlike surface states in the CB of about 2×10^{13} cm^{-2}.eV^{-1}.

3.3.2 Conduction-band dispersion relation

Let us now determine the CB dispersion relation at the (111)A surface of n-type $In_{0.53}Ga_{0.47}As$. Figure 3.5(a) shows a STM topographic image of the (111)A surface, at high doping ($n = 1\times10^{19}$ cm^{-3}). Monolayer steps separating atomically-flat terraces are visible in the image. Figure 3.5(b) shows dI/dU spatial maps of this area, for two values of U corresponding to energies within the CB. It is found that the LDOS in the CB has a complex spatial distribution, with a wavelength which decreases when U increases. This LDOS spatial modulation is ascribed to electron standing waves resulting from scattering interferences [55–60, 62–64, 67, 69–72, 74, 75, 78, 79]. Scattering centers are mainly ionized silicon donors distributed in the whole thin film, as well as native point defects located at the surface (section 3.3.3). For the value of n investigated, the band-bending in the near-surface region is upward and the Fermi wavelength is much smaller than the thickness of the grown $In_{0.53}Ga_{0.47}As$ thin film. Therefore electrons in the near-surface region form a three-dimensional system. Due to the continuous depth distribution of scattering centers below the surface (the $In_{0.53}Ga_{0.47}As$ thin film is uniformly doped by silicon), the surface-plane wave number $k_{||}$ detected in dI/dU spatial maps at sample voltage U takes all values between 0 and k, where k is the electron wave number at the energy corresponding to U. Consequently, a disk-shaped distribution is observed in Fourier transforms of dI/dU spatial maps [figure 3.5(c)], and the diameter of the disk equals $4k$. Using the rotationally averaged Fourier spectra [figure 3.5(d)], k was precisely determined as a function of U. The same analysis was performed for different values of n. Results are shown in figure 3.6. The obtained CB dispersion relation is well fitted by a two-band Kane model including nonparabolicity effects (appendix C). At each value of n investigated, the fit leads to an effective mass m_C at the CB minimum in agreement (within the fit uncertainty of about 10%)

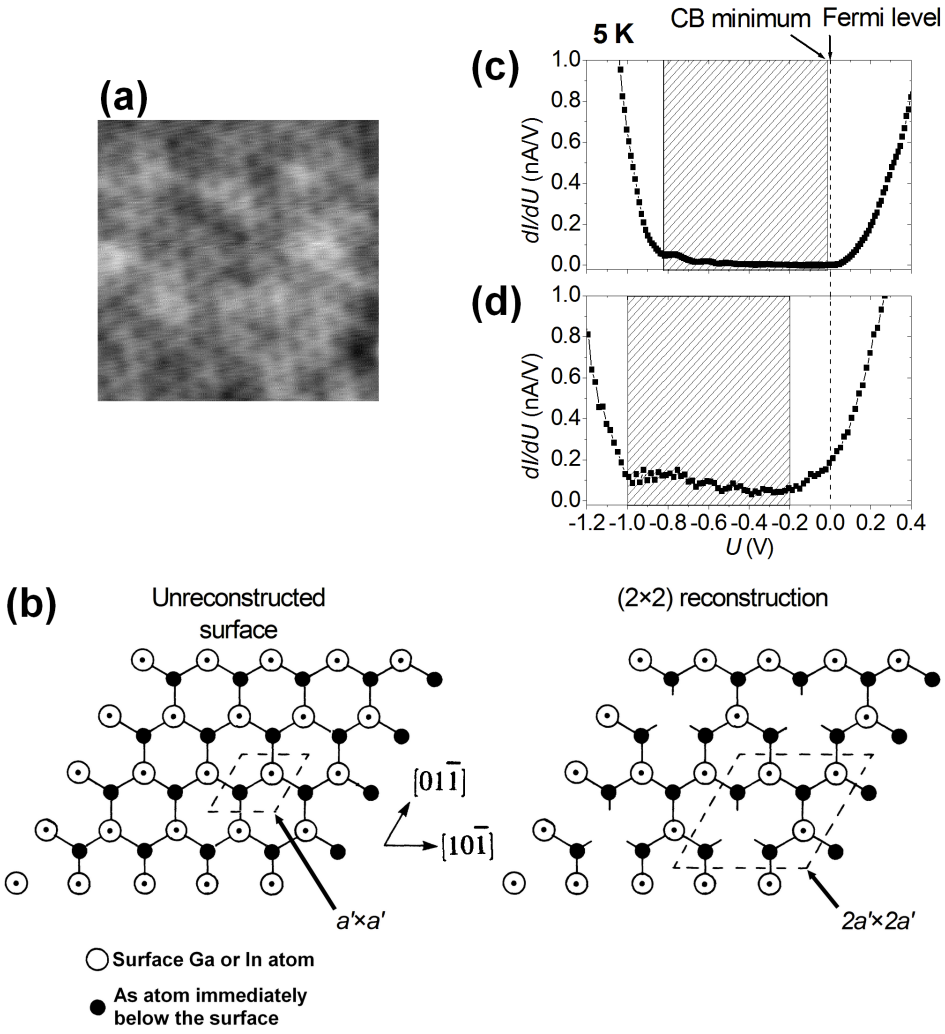

Figure 3.4: (111)A surface of n-type $In_{0.53}Ga_{0.47}As$. **(a)** 10.7×10.7 nm^2 STM topographic image (U = +2.5 V; I = 0.15 nA); $n = 1\times10^{19}$ cm^{-3}. **(b)** Schematic of the unreconstructed (111)A surface and of the (2×2) reconstruction [107, 108]. a' denotes the lattice constant of the hexagonal unit cell of the unreconstructed (111)A surface ($a' = \frac{a\sqrt{2}}{2}$, where a is the bulk lattice constant). **(c)** dI/dU spectrum for $n = 1\times10^{16}$ cm^{-3} and **(d)** $n = 1\times10^{19}$ cm^{-3}. The Fermi level ($U = 0$) and the CB minimum are indicated. The hatched region represents the band gap. The nonzero signal in the band gap of the dI/dU spectra is due to the presence of filled CB states (appendix A). The position of the CB minimum is determined by finding from which U the slope of dI/dU becomes positive.

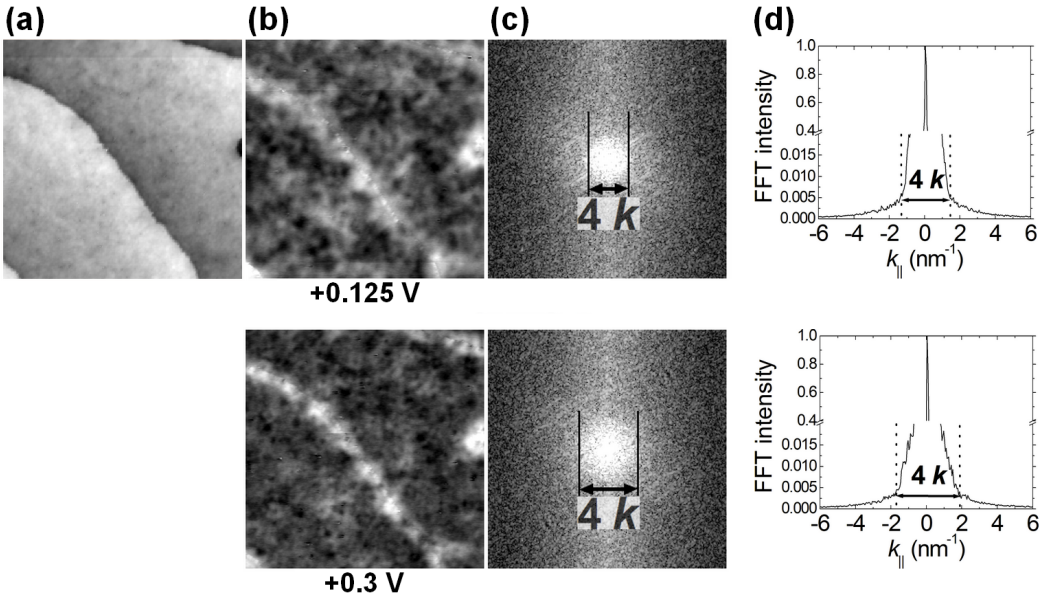

Figure 3.5: Fourier analysis of dI/dU spatial maps at the (111)A surface of n-type $In_{0.53}Ga_{0.47}As$. **(a)** 134×134 nm^2 STM topographic image ($U = +0.3$ V; $I = 0.25$ nA); $n = 1\times10^{19}$ cm^{-3}. **(b)** dI/dU spatial maps of the same area as in (a), at $U = +0.125$ V and $U = +0.3$ V. Bright regions correspond to high dI/dU signal. **(c)** Fast Fourier transforms (FFTs) of the dI/dU spatial maps of (b). In the FFT of a dI/dU spatial map at sample voltage U, the diameter of the disk-shaped distribution equals $4k$, where k is the electron wave number at the energy corresponding to U. **(d)** Rotational average of the FFTs of (c): FFT intensity as a function of the surface-plane wave number $k_{||}$. The FFT intensity is normalized by the value at $k_{||} = 0$.

with a previously reported value of $0.041m_0$ [99], and to a surface Fermi level position consistent with that extracted from dI/dU spectra [figure 3.3(a)].

We emphasize that the expected CB dispersion relation for $In_{0.53}Ga_{0.47}As$ (namely the two-band Kane model with an effective mass at the CB minimum of $0.041m_0$) is consistent with both the Fourier analysis of dI/dU spatial maps (which leads to k for values of U in the range from about +0.1 V to about +0.3 V) and the analysis of dI/dU spectra (which leads to the position of the CB minimum, corresponding to values of U in the range from about -0.2 V to about 0 V). It means that tip-induced band bending (appendix B) does not affect the STS data obtained in this work (at least for U in the range from about -0.2 V to about +0.3 V), although the density of acceptorlike surface states was found to be low (section 3.3.1).

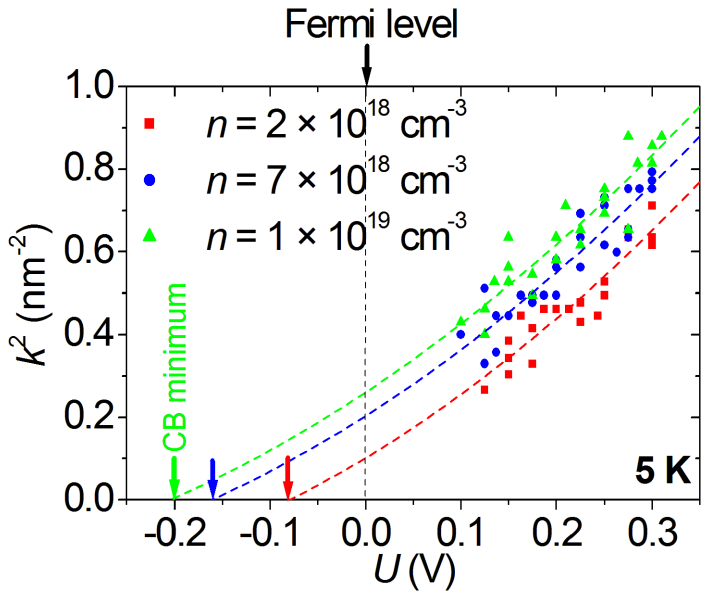

Figure 3.6: (Color) CB dispersion relation determined by Fourier analysis of dI/dU spatial maps at the (111)A surface of n-type $In_{0.53}Ga_{0.47}As$, for three different values of n (dots). Also shown is a fit by a two-band Kane model including nonparabolicity effects (appendix C) (dashed lines).

3.3.3 Native point defects

Two type of point defects are observed at the $In_{0.53}Ga_{0.47}As(111)A$ surface, as shown in figure 3.7 in the case of a nominally undoped $In_{0.53}Ga_{0.47}As$ layer.[1] The density of these defects does not increase with time. Therefore the defects are not due to surface contamination by residual gas atoms in the UHV environment of the STM chamber, but are rather native defects formed during the MBE growth.[2] The first type of defect appears as a depression in STM topography at positive sample voltage [figure 3.7(a)]. dI/dU spectra acquired close to the defect [figure 3.7(b)] have a peak near the valence-band maximum, and a large signal in the valence band. Therefore the defect is probably negatively charged, the peak near the valence-band maximum corresponding to an acceptor bound state. The second type of defect appears as a protrusion in STM topography at positive sample

[1]The last 50 nm of the $In_{0.53}Ga_{0.47}As$ layer is nominally undoped. However, the first 100 nm of the layer is doped by silicon with a density of about 7×10^{18} cm^{-3}, in order to ensure sufficient electrical conductivity for STS measurements.

[2]Surface contamination during the sample transfer under UHV from the MBE chamber to the STM chamber is unlikely, since the transfer is fast (less than 20 min) and the surface is hot (more than 400°C when the sample is taken out from the MBE chamber).

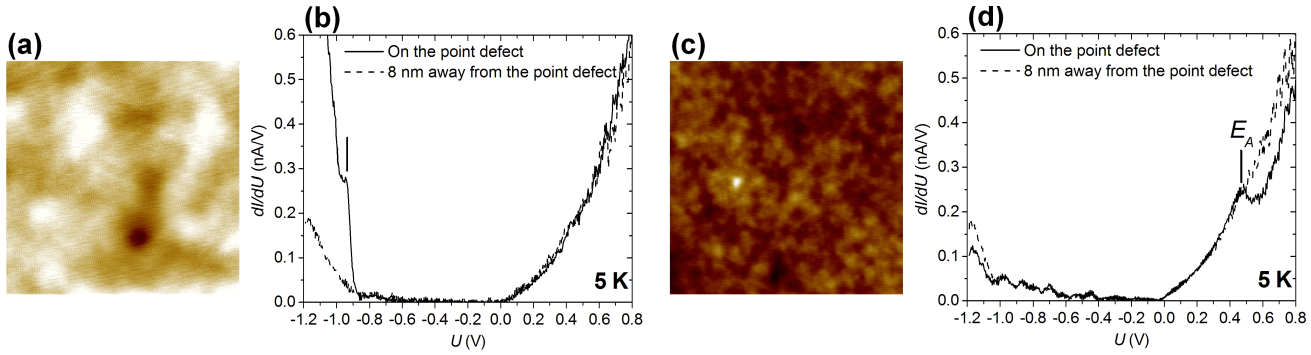

Figure 3.7: (Color) (111)A surface of nominally undoped $In_{0.53}Ga_{0.47}As$. **(a)** 10.7×10.7 nm^2 STM topographic image (U = +1.1 V; I = 0.12 nA). A native point defect appearing as a depression is visible. **(b)** dI/dU spectrum acquired on the defect of (a) (solid curve), and dI/dU spectrum acquired at a point located 8 nm away from the defect (dashed curve). In the dI/dU spectrum acquired on the defect, a peak is observed near the valence-band maximum, as indicated by a vertical line. **(c)** 29.5×29.5 nm^2 STM topographic image (U = +1.1 V; I = 0.12 nA). A native point defect appearing as a protrusion is visible. **(d)** dI/dU spectrum averaged over a 2×2 nm^2 square area centered on the defect of (c) (solid curve), and dI/dU spectrum averaged over a 2×2 nm^2 square area located 8 nm away from the defect (dashed curve). In the dI/dU spectrum acquired on the defect, a peak is observed at $U = E_A$, as indicated by a vertical line.

voltage [figure 3.7(c)]. dI/dU spectra acquired close to the defect [figure 3.7(d)] have a peak at $U = E_A$ about 0.5 eV above the CB minimum, and a weak signal in the valence band. Recent first-principle calculations and STS studies [114–116] suggest that such a defect is positively charged, and corresponds to a Ga (or In) adatom sitting on top of the surface, or to a Ga (or In) antisite located in the topmost surface layers.

It should be noted that the native point defects are observed not only on terraces (as in the case of figure 3.7), but also on step edges. The defects located on step edges cannot be clearly seen in STM topographic images, but can be unambiguously identified by using STS measurements, since a dI/dU spectrum acquired close to a defect shows a peak near the valence-band maximum (in the case of a negatively charged defect) or in the CB (in the case of a positively charged defect).

At the (111)A surface of nominally undoped $In_{0.53}Ga_{0.47}As$, the density of negatively and positively charged defects is about 2×10^{11} cm^{-2} and 1×10^{11} cm^{-2}, respectively. Therefore the net density of negative charges at the surface is about $1\times10^{11}\times e$ cm^{-2} (where e is the elementary

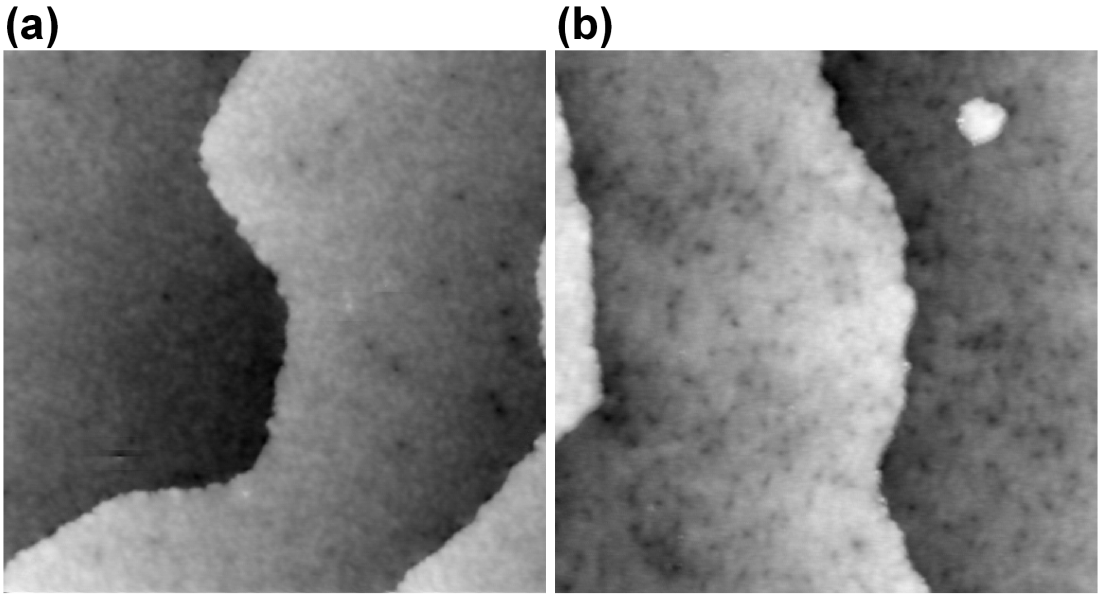

Figure 3.8: STM topographic image of a 107×107 nm^2 area of the $In_{0.53}Ga_{0.47}As(111)A$ surface (U = +1.1 V; I = 0.12 nA). **(a)** Nominally undoped layer. **(b)** Heavily doped layer ($n = 1\times10^{19}$ cm^{-3}).

charge). This corresponds to an upward band bending in the near-surface region of about 6 meV (appendix B), assuming that the nominally undoped $In_{0.53}Ga_{0.47}As$ layer is unintentionally n-type with a density of donor impurities of about 1×10^{15} cm^{-3} [117]. It means that, in the case of low n-type doping levels, the surface Fermi level almost equals the bulk Fermi level. This is in agreement with what found above (section 3.3.1). Note that the Fermi level at the $(111)A$ surface of nominally undoped $In_{0.53}Ga_{0.47}As$ is located close to the CB minimum, as seen in the dI/dU spectra of figure 3.7. This is a confirmation that the nominally undoped thin films are unintentionally n-type.

At the $(111)A$ surface of heavily doped $In_{0.53}Ga_{0.47}As$ ($n = 1\times10^{19}$ cm^{-3}), the density of positively charged defects is roughly the same as in the case of nominally undoped layers, but the density of negatively charged defects increases by at least a factor 10, as seen in figures 3.8(a) and (b). Therefore the net density of negative charges at the surface is of the order of $2\times10^{12}\times e$ cm^{-2}. This corresponds to an upward band bending in the near-surface region of the order of 70 meV (appendix B). It means that, in the case $n = 1\times10^{19}$ cm^{-3}, the surface Fermi level lies below the bulk Fermi level, the separation being of the order of 70 meV. This is in agreement with what found above (section 3.3.1).

In summary, it is found that the density of negatively charged defects at the $(111)A$ surface

of n-type $In_{0.53}Ga_{0.47}As$ increases with increasing n, explaining quantitatively the n-dependence of the surface Fermi level position found above (section 3.3.1). In other words, there is a direct link between the negatively charged defects and the acceptorlike surface states responsible for the n-dependence of the surface Fermi level position.

3.4 Summary

In this section, the (111)A epitaxial surface of n-type $In_{0.53}Ga_{0.47}As$ was studied by STS. It was shown that

- The surface Fermi level can be partially controlled by varying the n-type impurity density in the bulk. Specifically, the surface Fermi level almost equals the bulk Fermi level at low values of the free-electron density n, while it is slightly below the bulk Fermi level at high values of n. Such a partial unpinning of the Fermi level at the $In_{0.53}Ga_{0.47}As(111)A$ surface is crucial for the study of (111)A-oriented $In_{0.53}Ga_{0.47}As$ surface QWs. Indeed, the partial unpinning of the surface Fermi level means that it is possible to control the electron density in the surface QW, as demonstrated below (section 4). This would be impossible with the more conventional (001)-oriented GaAs or $In_{0.53}Ga_{0.47}As$ surface QWs, because of the strong midgap pinning of the surface Fermi level at the GaAs(001) [94, 95] and $In_{0.53}Ga_{0.47}As(001)$ [96] surfaces.

- The CB dispersion relation measured by STS is well described by a two-band Kane model including nonparabolicity effects (appendix C), with an effective mass at the CB minimum in agreement with a previously reported value of $0.041m_0$ [99]. This result will be indispensable for calculating the energy of the electronic states confined in (111)A-oriented $In_{0.53}Ga_{0.47}As$ surface QWs, as done below (section 4).

- Two types of native point defects are located at the surface, namely negatively and positively charged defects. The density of negatively charged defects increases with increasing n, explaining quantitatively the n-dependence of the surface Fermi level position. The native point defects at the $In_{0.53}Ga_{0.47}As(111)A$ surface have a considerable impact on the electronic properties of (111)A-oriented $In_{0.53}Ga_{0.47}As$ surface QWs, as demonstrated below (section 4).

First, the random distribution of the defects at the QW surface creates a disorder potential in the QW. Second, the positively charged defects induce hydrogenic bound states in the QW.

4 Electronic states in (111)*A*-oriented $In_{0.53}Ga_{0.47}As$ surface quantum wells

4.1 Background and motivation

In this section, based on the results obtained above (section 3), we report a STS study of (111)*A*-oriented $In_{0.53}Ga_{0.47}As$ surface QWs grown on top of $In_{0.52}Al_{0.48}As$ barriers. The STS measurements are performed at the (111)*A* epitaxial surface of the $In_{0.53}Ga_{0.47}As$ QWs, in order to probe with nanometer-scale resolution the in-plane spatial distribution of LDOS. Three interesting aspects of the physics of semiconductor QW structures are investigated:

- **The formation of electron subbands in a QW, due to quantum confinement along the growth direction**. STS allows to measure the LDOS as a function of energy [26–30], hence it can provide a direct evidence for quantum-size effects in semiconductor QW structures. Such an ability has been demonstrated only in a very recent work [82], in which STS measurements on InAs/GaSb QW structures show a LDOS with a step-like energy dependence, revealing the electron subbands formed in the QW. In section 4.3.1, we present similar STS results for the $In_{0.53}Ga_{0.47}As$ surface QW.

- **The effect of a disorder potential on the spatial distribution of LDOS in a QW**. As pointed out by Anderson nearly 50 years ago [118], the presence of disorder in a crystalline solid can lead to the formation of localized electronic states. The formation of the localized states is due to quantum-mechanical interference between electron waves that have undergone multiple scatterings by the disorder potential. Since localization is a general wave phenomenon relying on interference, it has been observed not only for electrons in disordered solids [3], but also in other systems exhibiting wave motion in inhomogeneous media, e.g., water waves in basins with random obstacles [119], light waves in the presence of randomly distributed optical scatterers [120, 121], and light waves in disordered photonic lattices [122]. The study of localization is therefore of paramount importance for many areas of physics.

The semiclassical model of disordered electronic systems predicts that localized states percolate with increasing energy [123]. A strong increase in electrical conductivity is expected when the Fermi level crosses over the percolation threshold, as studied in the technologically important case of 2DES [124].[1] Recently, various scanning probe microscopy techniques have been employed to improve the microscopic understanding of such a phenomenon of percolation of localized states in disordered 2DES. Near-field scanning optical microscopy has revealed strong spatial variations of electron density when the Fermi level lies below the percolation threshold [31]. In addition, using STS, the percolation of localized states with increasing energy has been directly observed in real-space maps of LDOS [81]. In section 4.3.2, we present STS measurements revealing that there is a disorder potential in the $In_{0.53}Ga_{0.47}As$ surface QW. We observe a remarkable feature in the case of a multisubband QW, namely that a phenomenon of percolation of localized states occurs in each subband tail. We determine the percolation threshold for each subband by using the semiclassical model of disordered electronic systems [123]. It was shown above (section 3.3.3) that native point defects are present at the $In_{0.53}Ga_{0.47}As(111)A$ surface. We propose that the disorder potential originates from the random distribution of these native point defects at the $(111)A$ surface of the $In_{0.53}Ga_{0.47}As$ QW.

- **The influence of quantum confinement on hydrogenic bound states formed in a QW**. Doping a semiconductor with foreign atoms called impurities allows to precisely tune the concentration of charge carriers, a principle at the basis of virtually all electronic and optoelectronic devices [2]. In the simplest approximation, an impurity inside a semiconductor is described as an hydrogen atom [2]. Thus the two essential properties of an impurity are the binding energy and the Bohr radius. Up to now, only the binding energy can be determined experimentally, by techniques such as absorption, luminescence, and Raman scattering [129]. However, it is highly desirable to also measure the Bohr radius a_B, which is a key parameter for various important phenomena, e.g.: an impurity band is formed if the mean impurity

[1] This change in electrical conductivity does not probably correspond to a true metal-insulator transition, since the scaling theory of localization predicts that all states are localized in disordered two-dimensional systems of non-interacting electrons, no matter how weak the disorder [125]. There might exist a true metallic phase in disordered two-dimensional systems of strongly interacting electrons [126, 127], but this is still a controversial topic [128].

separation becomes comparable with a_B [130]; two impurity nuclear spins interact if the distance between impurities becomes comparable with a_B [131]; impurities in QW structures are affected by the confining potential if the QW thickness becomes comparable with a_B [132]. The case of an impurity in a QW has attracted considerable attention both theoretically [132–136] and experimentally [137–143], since it is a model system for an hydrogen atom in reduced dimensionality [144]. It was shown above (section 3.3.3) that positively charged native point defects are present at the $In_{0.53}Ga_{0.47}As(111)A$ surface. In section 4.3.3, we present a detailed STS study of the behavior of these defects at the $(111)A$ surface of the $In_{0.53}Ga_{0.47}As$ QW. We are able to determine both the binding energy and the Bohr radius of single defects. Moreover, we show that the binding energy and the Bohr radius depend on the QW thickness, in quantitative agreement with the hydrogenic model. To our knowledge, this work presents the first direct measurement of the Bohr radius of an hydrogenic wave function in a semiconductor. While previous STM studies of impurities in III-V semiconductors have been mostly dedicated to acceptor states deriving from the nonspherical valence band [145–147], here we focus on donor states deriving from the spherical CB.

4.2 Experiment

$In_{0.53}Ga_{0.47}As/In_{0.52}Al_{0.48}As$ QW structures were grown by MBE on lattice-matched semi-insulating $InP(111)A$ substrates, at a growth rate of 0.1 ML/s and at a substrate temperature of 450°C. The grown layers were in direct electrical contact with the STM sample plate, through indium deposited on the edges of the InP substrate before the growth. Two different QW structures were investigated. Both structures consist of a $(111)A$-oriented $In_{0.53}Ga_{0.47}As$ surface QW of thickness l, grown on top of a 5-nm-thick $In_{0.52}Al_{0.48}As$ barrier. Electronic states in the $In_{0.53}Ga_{0.47}As$ surface QW are confined on one side by vacuum and on the other side by the $In_{0.52}Al_{0.48}As$ barrier. In the QW structure of type I [figure 4.1(a)], the barrier is doped by silicon in order to provide electrons to the QW (this is the so-called technique of modulation doping [17]). In the QW structure of type II [figure 4.2(a)], both the QW and the barrier are undoped, hence there is no electron in the QW.

After the growth, epitaxial surfaces were kept during 3 min at the growth temperature in an As_4 flux. Substrate heating was then stopped. When the surface temperature passed below 430°C

(detection limit of the infrared pyrometer), samples were rapidly taken out from the MBE chamber and transferred under UHV to the low-temperature STM chamber.

STM and STS measurements were performed at 5 K under UHV, on the (111)A clean epitaxial surface of the $In_{0.53}Ga_{0.47}As$ QW. STM topographic images were acquired in the constant-current mode. For STS experiments, the tunneling differential conductance dI/dU was directly measured through a lock-in amplifier. Spectra of dI/dU as a function of U were acquired by positioning the probe tip at one point above the surface and disengaging the current feedback loop. dI/dU spatial maps at fixed values of U were obtained by recording a dI/dU spectrum on each pixel of a grid. We recall that dI/dU at U is proportional to the LDOS at the sample surface at energy $+eU$ (where e is the elementary charge and $U = 0$ corresponds to the sample Fermi level), if the tip-sample separation is constant [equation (A.14)].

4.3 Results and discussion

4.3.1 Quantum confinement along the growth direction

Let us first demonstrate the formation of electron subbands in the $In_{0.53}Ga_{0.47}As$ QW. We investigate the structure of type I [figure 4.1(a)], where electrons are provided to the QW by modulation doping. Figure 4.1(b) shows a typical dI/dU spectrum acquired at the $In_{0.53}Ga_{0.47}As$ QW surface, for $l = 10$ nm. The measured band gap is about 0.8 eV, in agreement with what found above (section 3.3.1). The dI/dU signal in the CB has a clear step-like voltage dependence. In other words, the LDOS has a step-like energy dependence, which is the typical signature of 2DES. The steps correspond to the electron subbands formed in the QW due to quantum confinement along the growth direction. Three subbands are found.

The dI/dU spectrum of figure 4.1(b) indicates that the Fermi level ($U = 0$) is within the first subband. This was expected, considering that modulation doping is employed [figure 4.1(a)], and that the Fermi level is partially unpinned at the $In_{0.53}Ga_{0.47}As(111)A$ surface (section 3.3.1).

The energy of the subband minima was determined with respect to the CB minimum by solving the one-dimensional Schrödinger equation in the $In_{0.53}Ga_{0.47}As$ QW (appendix D), assuming the potential profile shown in figure 4.1(c). Following what found above (section 3.3.2), the CB dispersion

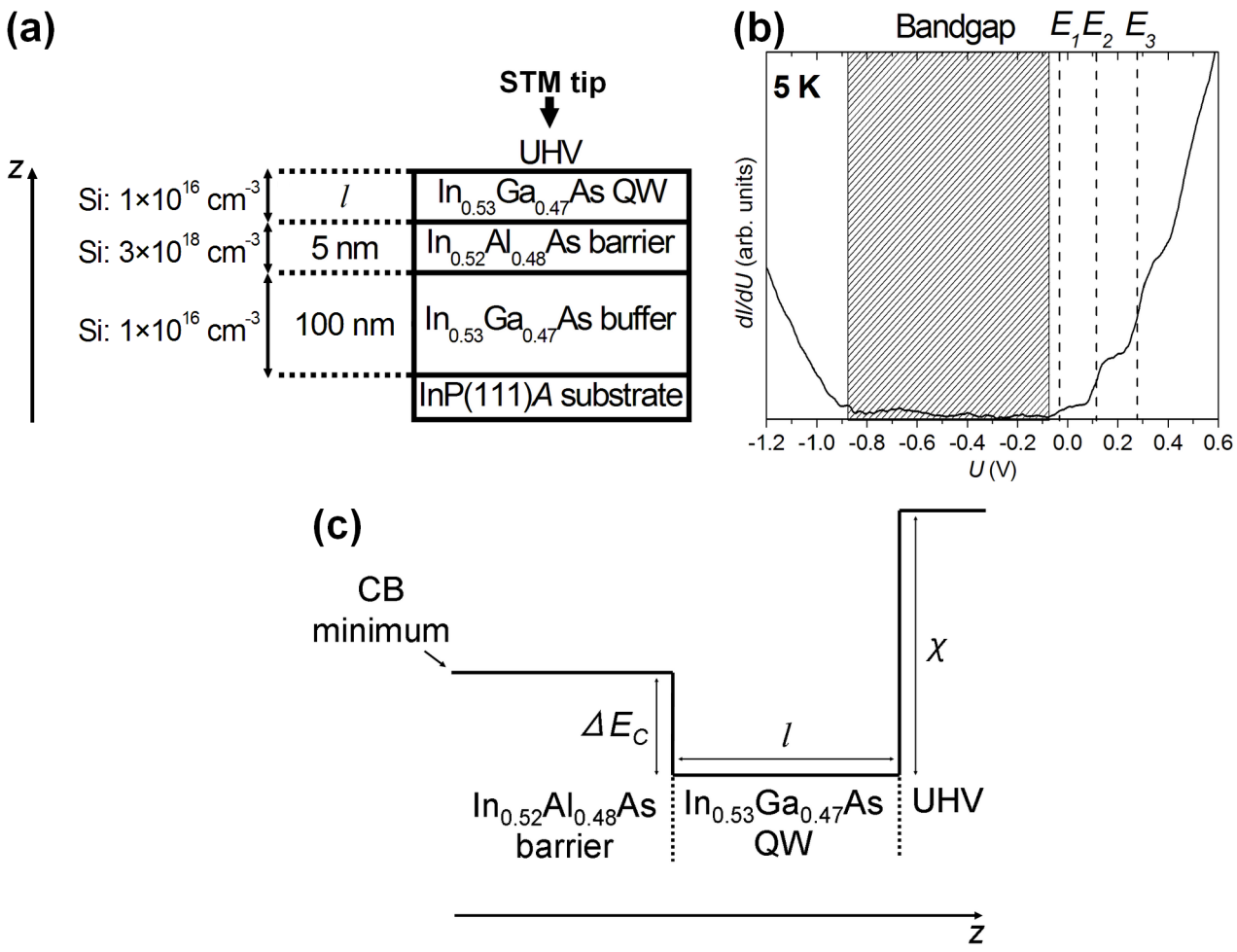

Figure 4.1: **(a)** $In_{0.53}Ga_{0.47}As/In_{0.52}Al_{0.48}As$ QW structure grown by MBE on a lattice-matched InP(111)A substrate: structure of type I. The $In_{0.52}Al_{0.48}As$ barrier is doped by silicon with a density of about 3×10^{18} cm^{-3}, in order to provide electrons to the $In_{0.53}Ga_{0.47}As$ surface QW (this is the so-called technique of modulation doping [17]). **(b)** dI/dU spectrum averaged over a 30×30 nm^2 square area at the $In_{0.53}Ga_{0.47}As$ QW surface, for a QW thickness $l = 10$ nm. The hatched region represents the band gap. The subband minima (E_1, E_2, and E_3) found from the spectrum are indicated. Note that the Fermi level ($U = 0$) is within the first subband. **(c)** Band diagram along the growth direction z for the $In_{0.53}Ga_{0.47}As/In_{0.52}Al_{0.48}As$ QW structure. l is the QW thickness. χ is the electron affinity of $In_{0.53}Ga_{0.47}As$. ΔE_C is the CB offset between $In_{0.53}Ga_{0.47}As$ and $In_{0.52}Al_{0.48}As$.

relation in the $In_{0.53}Ga_{0.47}As$ QW was given by a two-band Kane model including nonparabolicity (appendix C), with an effective mass m_C at the CB minimum of $0.041m_0$ [99]. The potential barrier was the electron affinity of $In_{0.53}Ga_{0.47}As$ on one side ($\chi = 4.48$ eV [148]), and the CB offset between $In_{0.53}Ga_{0.47}As$ and $In_{0.52}Al_{0.48}As$ on the other side ($\Delta E_C = 0.5$ eV [99]). The effective mass in the $In_{0.52}Al_{0.48}As$ barrier was $0.075m_0$ [99]. The calculation indicates that three subbands are formed in the QW for $l = 10$ nm, with the subband minima (E_1, E_2, and E_3) given by: $E_1 - E_{CBM} = 0.045$ eV (where E_{CBM} is the CB minimum), $E_2 - E_1 = 0.117$ eV, and $E_3 - E_2 = 0.150$ eV. This is in good agreement with the subband spacings found from the dI/dU spectrum of figure 4.1(b) ($E_2 - E_1 = 0.13$ eV and $E_3 - E_2 = 0.17$ eV).

If it is assumed that half of the electrons supplied by the silicon donors of the $In_{0.52}Al_{0.48}As$ barrier go to the $In_{0.53}Ga_{0.47}As$ QW (the other half going to the $In_{0.53}Ga_{0.47}As$ buffer layer), then the surface density of electrons in the QW is $n_S = \frac{1}{2} \times (3 \times 10^{18}\ \mathrm{cm}^{-3}) \times l$ [figure 4.1(a)]. Electrons in the QW occupy both the first subband [density of states above E_1 (in the simple case of a free-two dimensional electron gas): $N_C = m_C/\pi\hbar^2$] and the band of acceptorlike surface states [density of states above E_{CBM} (section 3.3.1): $N_A = 2{\times}10^{13}\ \mathrm{eV}^{-1}.\mathrm{cm}^{-2}$]. Therefore the Fermi level E_F in the QW is given by:

$$n_S = N_C(E_F - E_1) + N_A(E_F - E_{CBM}). \tag{4.1}$$

Solving this equation gives $E_F - E_1 = 0.016$ eV. This is consistent with the Fermi level position found from the dI/dU spectrum of figure 4.1(b) ($E_F - E_1 = 0.02$ eV).

4.3.2 Disorder potential

Let us now focus on the effect of a disorder potential on the spatial distribution of LDOS in the $In_{0.53}Ga_{0.47}As$ QW. We investigate the structure of type II [figure 4.2(a)], where there is no electron in the QW. The absence of electrons in the QW allows us to consider the simple case where there is no screening effect.

Percolation of localized states

Figure 4.2(b) shows a typical dI/dU spectrum acquired at a given point of the $In_{0.53}Ga_{0.47}As$ QW surface, for $l = 10$ nm. The Fermi level ($U = 0$) is within the band gap, i.e., the subbands are

empty. This is because both the $In_{0.53}Ga_{0.47}As$ QW and the $In_{0.52}Al_{0.48}As$ barrier are undoped. We emphasize that it is possible to control the electron density in the (111)*A*-oriented $In_{0.53}Ga_{0.47}As$ surface QW: the Fermi level is within the band gap in the QW structure of type II, while it was found to be within the first subband in the QW structure of type I (section 4.3.1). The control of electron density is possible owing to the partial unpinning of the Fermi level at the $In_{0.53}Ga_{0.47}As(111)A$ surface (section 3.3.1).

Note that the subband spacings found from the dI/dU spectrum of figure 4.2(b) ($E_2 - E_1 = 0.16$ eV and $E_3 - E_2 = 0.21$ eV) are larger than the values calculated above (section 4.3.1), and that the measured band gap (about 1.15 eV) is larger than the expected value of 0.8 eV.[2] Such discrepancies were not found in the case of the structure of type I (section 4.3.1).[3]

We now examine the spatial distribution of LDOS in the QW plane. Figure 4.3(a) shows a STM topography of a 214×214 nm^2 area of the QW surface, for $l = 10$ nm. A dI/dU spectrum was acquired on each pixel of a 128×128 grid of this area, for U ranging from 0 V to +1 V. Figure 4.3(b) shows a dI/dU spatial map of this area at $U = +0.376$ V. The dI/dU signal has large spatial fluctuations in the QW plane. This is because the subband minima shift rigidly with the spatial position. As an example, let us consider the two locations A and B indicated in figure 4.3(b). A rigid shift of the subband minima of 0.15 eV is found between the two locations, as shown in figure 4.3(c). $U = +0.376$ V corresponds to an energy which is within the band gap at the location A, while within the first subband at the location B. This leads to the contrast between the two locations observed in the dI/dU spatial map of figure 4.3(b). Due to such spatial variations of the subband minima, the dI/dU spectrum averaged over the whole area of figure 4.3(a) is a broaden step-like function, as shown in figure 4.3(d). This broadening corresponds to the formation of a

[2]These discrepancies can be explained as follows. The $In_{0.53}Ga_{0.47}As$ QW layer is insulating in the case of the structure of type II, since the Fermi level is within the band gap. It means that the QW layer is not at the same electrostatic potential than the STM sample plate, in spite of the presence of the indium contact between the grown layers and the STM plate (section 4.2). In other words, there may be a voltage drop between the QW layer and the STM sample plate, most probably in the $In_{0.52}Al_{0.48}As$ barrier.

[3]The $In_{0.53}Ga_{0.47}As$ QW layer is conductive in the case of the structure of type I, since the Fermi level is within the first subband (section 4.3.1). It means that the QW layer is put at the same electrostatic potential than the STM plate, through the indium contact between the grown layers and the STM plate (section 4.2). In other words, there is no voltage drop between the QW layer and the STM sample plate.

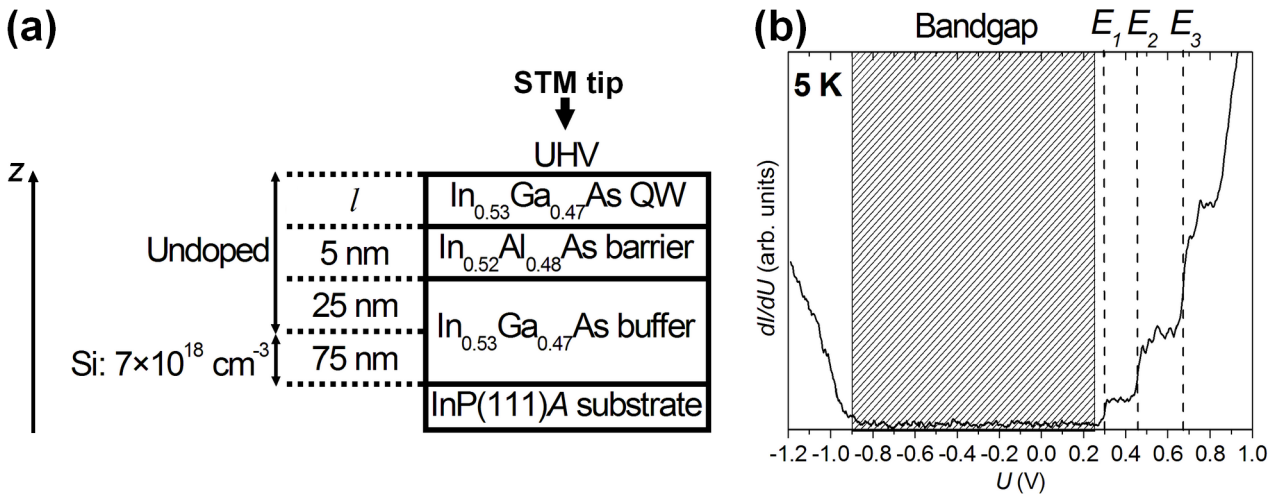

Figure 4.2: **(a)** $In_{0.53}Ga_{0.47}As/In_{0.52}Al_{0.48}As$ QW structure grown by MBE on a lattice-matched InP(111)A substrate: structure of type II. Both the $In_{0.53}Ga_{0.47}As$ surface QW and the $In_{0.52}Al_{0.48}As$ barrier are undoped, hence there is no electron in the QW. However, the first 75 nm of the $In_{0.53}Ga_{0.47}As$ buffer layer are doped by silicon with a density of about 7×10^{18} cm^{-3}, in order to ensure sufficient electrical conductivity for STS measurements. **(b)** dI/dU spectrum acquired at a given point of the $In_{0.53}Ga_{0.47}As$ QW surface, for a QW thickness $l = 10$ nm. The hatched region represents the band gap. The subband minima (E_1, E_2, and E_3) found from the spectrum are indicated. Note that the Fermi level ($U = 0$) is within the band gap.

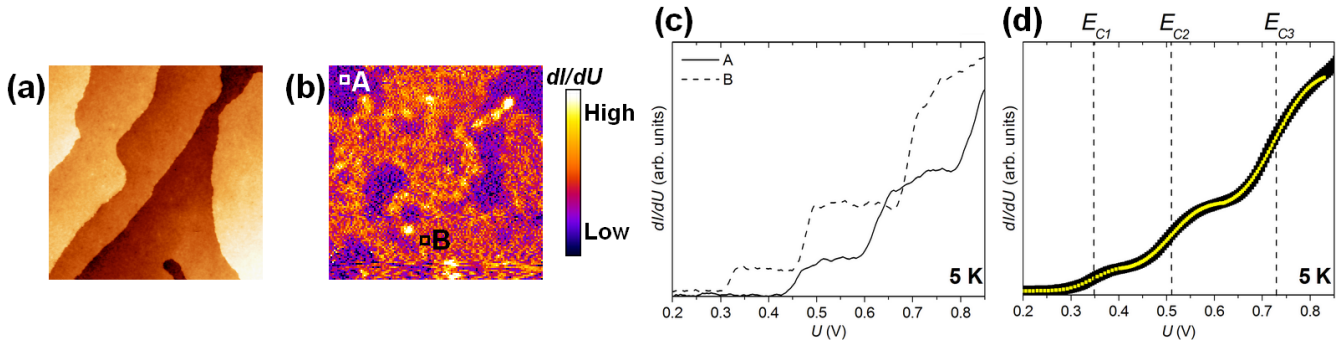

Figure 4.3: (Color) **(a)** STM topographic image of a 214×214 nm^2 area of the $In_{0.53}Ga_{0.47}As$ QW surface ($U = +1.1$ V; $I = 0.12$ nA), for the structure of type II with $l = 10$ nm. A dI/dU spectrum was acquired on each pixel of a 128×128 grid of this area, for U ranging from 0 V to +1 V. **(b)** dI/dU spatial map of the same area as in (a), at $U = +0.376$ V. **(c)** dI/dU spectra averaged over the square areas A (solid curve) and B (dashed curve) indicated in (b). **(d)** dI/dU spectrum averaged over the whole area of (a) (black curve), and fit of each subband by equation (4.2) (yellow curve). The percolation thresholds (E_{C1}, E_{C2}, and E_{C3}) determined by the fit are indicated.

band tail [130] for each subband. Note that the spatial fluctuations of the dI/dU signal observed in a particular area are reproducible for successive measurements.

In the semiclassical approximation of electron dynamics in crystalline solids [149], if a spatially varying potential $V(\mathbf{r})$ is superimposed on the periodic potential of the crystal, then the energy bands shift rigidly when $\mathbf{r}$ changes. Thus it is natural to interpret our experimental data in terms of the semiclassical approximation, i.e., by assuming that a disorder potential $V(\mathbf{r})$ induces the observed rigid shift of the subband minima.

Figure 4.4(a) shows dI/dU spatial maps of the same area as in figure 4.3(a), at several values of U covering the transition from the band gap to the first subband. In a dI/dU spatial map at a given value of U, one can easily distinguish the regions for which U is within the band gap (regions of low dI/dU), from the regions for which U is within the first subband (regions of high dI/dU). The fraction of area of high dI/dU increases with increasing U. Specifically, at low U there are only isolated clusters of high dI/dU, while at high U there is an extended cluster of high dI/dU. Thus the series of dI/dU spatial maps of figure 4.4(a) provides a real-space observation of the percolation of localized states with increasing energy.

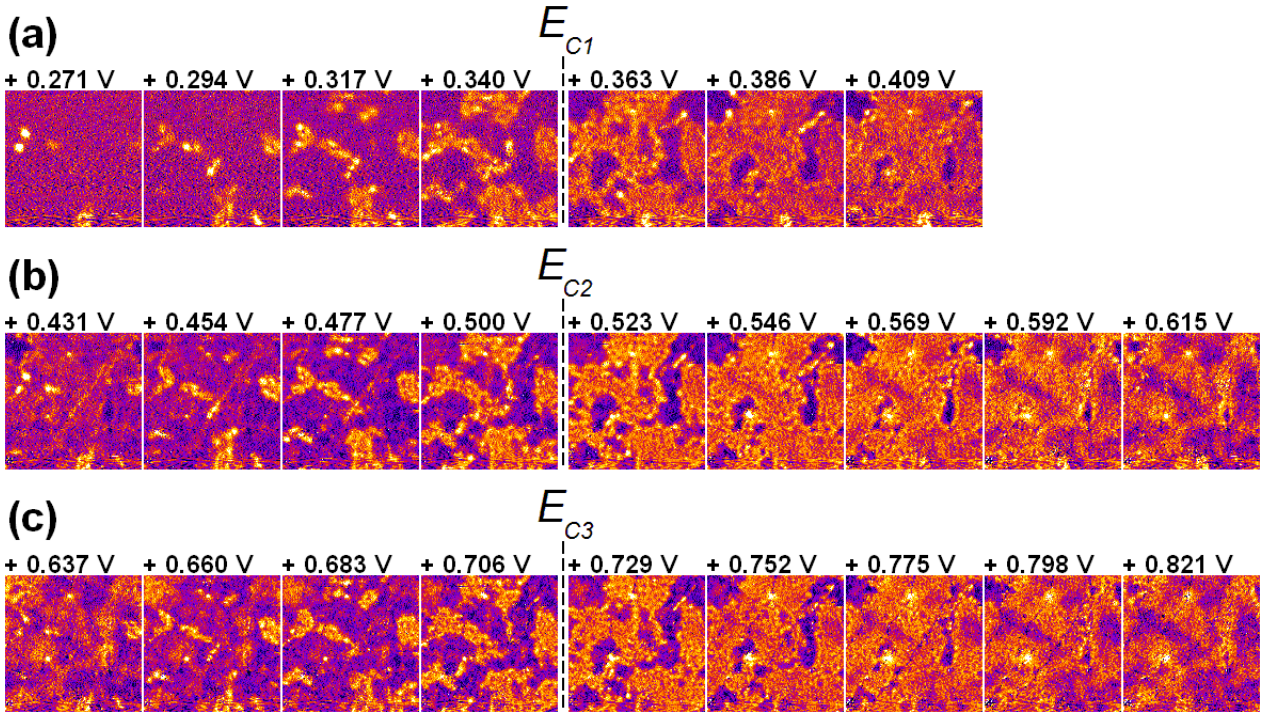

Figure 4.4: (Color) dI/dU spatial maps of the same area as in figure 4.3(a), at several values of U covering the transition **(a)** from the band gap to the first subband, **(b)** from the first to the second subband, and **(c)** from the second to the third subband. The percolation thresholds (E_{C1}, E_{C2}, and E_{C3}), determined by fitting the dI/dU spectrum of figure 4.3(d) by equation (4.2), are indicated.

Interestingly, we observe a phenomenon of percolation of localized states not only for the first subband [figure 4.4(a)], but also for the second subband [figure 4.4(b)] and the third subband [figure 4.4(c)]. We would like to stress that the evolution of dI/dU spatial maps with increasing U is mostly identical for the three figures 4.4(a), (b) and (c). This is a confirmation that there is actually a *rigid* shift of the subband minima, in agreement with the semiclassical approximation [149].

Determination of the percolation thresholds

The percolation threshold can be determined for each subband, by using a statistical characterization of the disorder potential, as described by the semiclassical model of disordered electronic systems [123]. The disorder potential $V(\mathbf{r})$ induces spatial variations of the nth subband minimum: $E_n(\mathbf{r}) = E_n + V(\mathbf{r})$, as depicted in figure 4.5(a). The LDOS of the nth subband at point $\mathbf{r}$ and energy E is nonzero if $E > E_n(\mathbf{r})$ and zero if $E < E_n(\mathbf{r})$. Associated with $V(\mathbf{r})$ is the statistical distribution function $\psi(V)$ [$\psi(V)dV$ is the probability of occurrence, at an arbitrary location $\mathbf{r}$, of a potential value in the range $V \leftrightarrow V+dV$]. The knowledge of $\psi(V)$ allows to determine the function $\phi_n(E) = \int_{-\infty}^{E-E_n} \psi(V)dV$, defining the fraction of area for which $E > E_n(\mathbf{r})$, i.e., the fraction of area of nonzero LDOS for a given subband n at energy E. $\phi_n(E)$ increases with increasing E [figure 4.5(b)]. At low E there are only isolated clusters of nonzero LDOS, while at high E there is an extended cluster of nonzero LDOS [figure 4.5(c)]. The extended cluster is formed at a critical value $E = E_{Cn}$, corresponding to the percolation threshold for the nth subband.

In the high-disorder limit, $\psi(V)$ obeys a Gaussian distribution [123, 130]. In this case, it immediately follows that

$$\phi_n(E) = \frac{1 + \mathrm{erf}[(E - E_n - \bar{V})/\sqrt{2}V_{rms}]}{2}. \tag{4.2}$$

Here, erf is the error function, $\bar{V}$ is the mean of $V(\mathbf{r})$, and V_{rms} is the root mean square of $V(\mathbf{r})$. The critical percolation density is 1/2 for a 2DES subject to a disorder potential with a Gaussian distribution [123]. Therefore E_{Cn} is given by $\phi_n(E_{Cn}) = 1/2$, i.e., $E_{Cn} = E_n + \bar{V}$.

If the LDOS of the nth subband at a given point $\mathbf{r}$ is assumed to be a Heavyside function of the energy E, as for a free two-dimensional electron gas, then the spatially averaged LDOS is simply proportional to $\phi_n(E)$. Therefore each subband in the spatially averaged dI/dU spectrum of figure 4.3(d) was fitted by equation (4.2). The fit of the dI/dU spectrum is excellent, which means that assuming a Gaussian distribution for the disorder potential is a correct choice. The fit leads to the

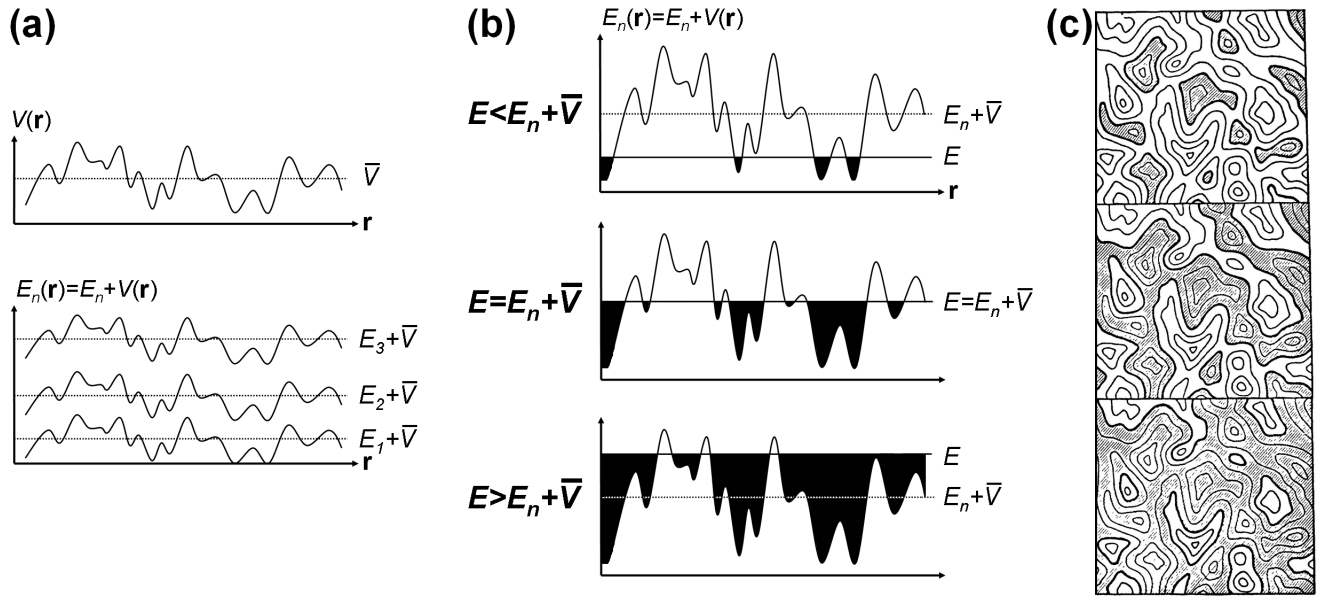

Figure 4.5: Semiclassical model of disordered electronic systems [123]: case of multisubband 2DES. **(a)** The disorder potential $V(\mathbf{r})$ induces spatial variations of the nth subband minimum: $E_n(\mathbf{r}) = E_n + V(\mathbf{r})$. **(b)** For a given subband n, the fraction of area for which $E > E_n(\mathbf{r})$ (i.e., the fraction of area of nonzero LDOS) increases with increasing energy E. **(c)** At low E there are only isolated clusters of nonzero LDOS, while at high E there is an extended cluster of nonzero LDOS. The extended cluster is formed at a critical value $E = E_{Cn}$, corresponding to the percolation threshold for the nth subband. In the case of a disorder potential with a Gaussian distribution, $E_{Cn} = E_n + \bar{V}$.

percolation thresholds (E_{C1} = +0.35 V, E_{C2} = +0.51 V, and E_{C3} = +0.72 V), as well as to the root mean square of the disorder potential [V_{rms} = 0.05 ($\pm$ 0.01) eV]. The percolation thresholds are indicated in the series of dI/dU spatial maps of figure 4.4. It can be checked that, for a given subband, the percolation threshold corresponds to the value of U at which the extended cluster of high dI/dU is formed.

Origin of the electronic disorder

We now discuss the physical origin of the electronic disorder observed in the $In_{0.53}Ga_{0.47}As$ QW. A first possible cause of electronic disorder is related to spatial fluctuations of the QW thickness, l. Monolayer steps separating atomically-flat terraces are visible in the STM topography of figure 4.3(a). The height of a monolayer step measured in STM topographic images is 0.34 nm, corre-

sponding to the expected value of $a/\sqrt{3}$ for the (111) surface of a crystal with a zincblende structure (where a is the lattice constant). Solving the one-dimensional Schrödinger equation in the QW (appendix D) indicates that the shift of E_1 due to a variation of l by 0.34 nm is 2 meV, which is much smaller than the V_{rms} found above. Therefore the spatial variations of l are not the main cause of electronic disorder. To confirm this point, let us compare the STM topography of figure 4.3(a) with the dI/dU spatial maps of figures 4.3(b) and 4.4. It can be seen that the spatial fluctuations of the dI/dU signal are irrelevant to the position of the terraces.

A second possible cause of electronic disorder is related to spatial fluctuations of the CB offset between $In_{0.53}Ga_{0.47}As$ and $In_{0.52}Al_{0.48}As$, ΔE_C. Spatial fluctuations of ΔE_C may arise due to phase separation in the ternary alloys $In_{0.53}Ga_{0.47}As$ and $In_{0.52}Al_{0.48}As$ [111–113]. The band gap was measured by STS in both the $In_{0.53}Ga_{0.47}As$ QW and the $In_{0.52}Al_{0.48}As$ barrier.[4] In both cases, the spatial variations of the band gap were found to be less than 0.08 eV. It is known that ΔE_C is equal to about 70% of the difference in band gap between $In_{0.53}Ga_{0.47}As$ and $In_{0.52}Al_{0.48}As$ [99]. Therefore the spatial variations of ΔE_C are less than $0.7\times2\times0.08$ eV=0.11 eV. Solving the one-dimensional Schrödinger equation in the QW (appendix D) indicates that the corresponding shift of E_1 is less than 1 meV. Again, this is much smaller than the V_{rms} found above. Therefore the spatial variations of ΔE_C are not the main cause of electronic disorder.

A third possibility is a disorder potential created by a random distribution of charged impurities [124, 150]. The QW and the barrier are nominally undoped. However, native point defects are present at the $In_{0.53}Ga_{0.47}As(111)A$ surface, as discussed above (section 3.3.3). These defects are observed at the $(111)A$ surface of the $In_{0.53}Ga_{0.47}As$ QW [figures 4.6(a) and (c)]. The dI/dU spectra acquired close to the defects exhibit the same features as found above (section 3.3.3), namely a peak near the valence-band maximum and a large signal in the valence band for the negatively charged defect [figure 4.6(b)], and a peak located at $U = E_A$ about 0.5 eV above the CB minimum for the positively charged defect [figure 4.6(d)]. In addition, for the positively charged defect, a peak is observed near each subband minimum [figure 4.6(d)]. These peaks are interpreted as bound states splitting off from the subband minima, due to the attractive potential created by the defect.[5]

[4] In order to measure by STS the band gap in the $In_{0.52}Al_{0.48}As$ barrier, we used a reference sample without the $In_{0.53}Ga_{0.47}As$ QW.

[5] The formation of bound states in the vicinity of the positively charged defects is a breaking-down of the semi-classical approximation used in the analysis of the percolation phenomenon. However, the bound states are observed

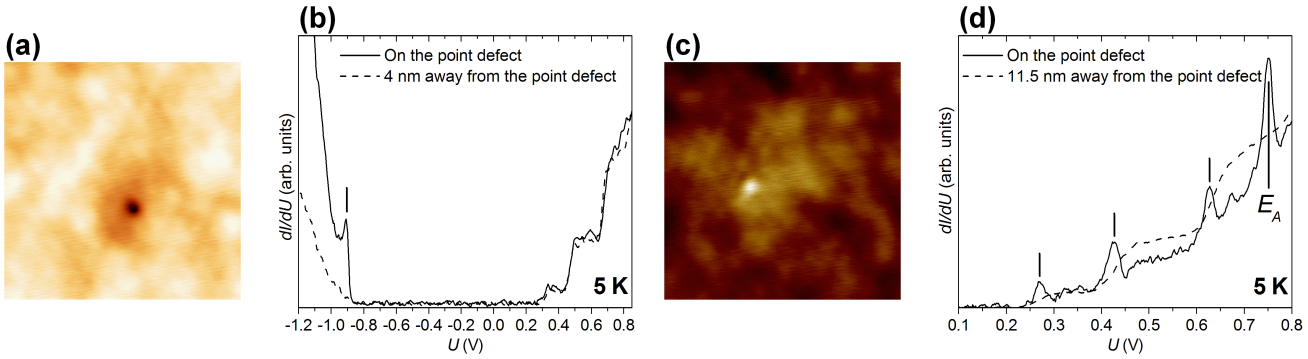

Figure 4.6: (Color) **(a)** STM topographic image of a 10.7×10.7 nm^2 area of the $In_{0.53}Ga_{0.47}As$ QW surface ($U = +1.2$ V; $I = 0.12$ nA), for the structure of type II with $l = 10$ nm. A negatively charged native point defect (dark spot) is visible. **(b)** dI/dU spectrum acquired on the defect of (a) (solid curve), and dI/dU spectrum acquired at a point located 4 nm away from the defect (dashed curve). In the dI/dU spectrum acquired on the defect, a peak is observed near the valence-band maximum, as indicated by a vertical line. **(c)** STM topographic image of a 10.7×10.7 nm^2 area of the $In_{0.53}Ga_{0.47}As$ QW surface ($U = +1.1$ V; $I = 0.12$ nA), for the structure of type II with $l = 10$ nm. A positively charged native point defect (bright spot) is visible. **(d)** dI/dU spectrum acquired on the defect of (c) (solid curve), and dI/dU spectrum averaged over points located 11.5 nm away from the defect (dashed curve). In the dI/dU spectrum acquired on the defect, a peak is observed at $U = E_A$, as indicated by a vertical line. In addition, a peak is observed near each subband minimum, as also indicated by vertical lines.

The root mean square of the bare Coulomb potential created in a 2DES by a plane of randomly distributed point charges is given by [124]

$$V_{rms} = \sqrt{2\pi}\frac{e^2\sqrt{C}}{4\pi\epsilon}\sqrt{\ln\frac{L}{2s}}. \tag{4.3}$$

Here, C is the density of point charges, ϵ is the dielectric constant, L is the size of the area under consideration in the 2DES plane, and s is the distance between the plane containing the point charges and the 2DES plane. In our case, $C = 3{\times}10^{11}$ cm^{-2} (total density of native point defects, as discussed in section 3.3.3), $\epsilon = \frac{\epsilon_0+\epsilon_{bulk}}{2}$ [dielectric constant for a point charge at the interface between $In_{0.53}Ga_{0.47}As$ and vacuum (appendix E), with $\epsilon_{bulk} = 13.75\epsilon_0$ dielectric constant of $In_{0.53}Ga_{0.47}As$ [2]], $L = 214$ nm [size of the area of figure 4.3(a)], and $s = l/4 = 2.5$ nm (if we consider, e.g., the case of the second subband[6]). The result of the calculation is $V_{rms} = 0.052$ eV, which is in good agreement with the value found above.[7] Thus the origin of the electronic disorder is ascribed to the native point defects located at the QW surface.

To confirm this point, let us compare the spatial fluctuations of the dI/dU signal with the position of the native point defects found at the QW surface. Figure 4.7(a) shows a STM topography of a 96×96 nm^2 area of the QW surface, for $l = 10$ nm. A dI/dU spectrum was acquired on each pixel of a 64×64 grid of this area, for U ranging from -1.2 V to +1 V. 31 defects (20 negatively charged defects and 11 positively charged defects) were found in this area by examining the dI/dU spectrum of each pixel of the grid. As an example, figure 4.7(b) shows the dI/dU spectrum for one of the negatively charged defects [which is labeled AD in figure 4.7(a)], and the dI/dU spectrum for one of the positively charged defects [which is labeled DD in figure 4.7(a)]. The bare Coulomb

only in a small fraction (less than 10%) of the surface. A detailed study of the bound states is presented below (section 4.3.3).

[6]In the ideal case of a QW with infinite barrier height, the distribution of LDOS along the growth direction is given by $|\psi_n(z)|^2 \propto \sin^2\left(\frac{n\pi z}{l}\right)$, where z is the distance from the QW surface. The distance between the QW surface and the closest maximum of LDOS is $l/2n$. Thus the disorder Coulomb potential $V(\mathbf{r})$, created by the native point defects located at the QW surface, would be different for each subband. However, this difference is small [according to equation (4.3), V_{rms} changes only by 20% between the first and the third subband], in agreement with the semiclassical approximation.

[7]The length scale at which the disorder potential was characterized experimentally [i.e., $L = 214$ nm, the size of the area of figure 4.3(a)] is large enough. Indeed, equation (4.3) indicates that, for $L = 214$ nm, V_{rms} at $2L$ is only 10% larger than V_{rms} at L.

potential $V(\mathbf{r})$ created in the QW by the native point defects found in the area of figure 4.7(a) is given by

$$V(\mathbf{r}) = \sum_a \frac{e^2}{4\pi\epsilon\sqrt{(\mathbf{r}-\mathbf{r}_a)^2+s^2}} - \sum_d \frac{e^2}{4\pi\epsilon\sqrt{(\mathbf{r}-\mathbf{r}_d)^2+s^2}}. \quad (4.4)$$

Here, $\mathbf{r}_a$ and $\mathbf{r}_d$ are the positions in the QW plane of the negatively and positively charged defects, respectively. The dielectric constant ϵ is taken to be $\frac{\epsilon_0+\epsilon_{bulk}}{2}$, as explained above. s is taken to be $l/4 = 2.5$ nm (if we consider, e.g., the case of the second subband). The result of the calculation is shown in figure 4.7(c). As already mentioned, the LDOS of the nth subband at point $\mathbf{r}$ and energy E is nonzero if $E > E_n + V(\mathbf{r})$ and zero if $E < E_n + V(\mathbf{r})$. In this way, we can easily calculate the spatial distribution of LDOS in the area of figure 4.7(a). Calculated LDOS spatial maps are shown in figure 4.7(e). These should be compared with measured dI/dU spatial maps, shown in figure 4.7(d). It can be seen that the calculated LDOS and the measured dI/dU signal have a quite similar spatial distribution. This is remarkable, considering the simplicity of the calculation method. This is a clear confirmation that the electronic disorder observed experimentally in the QW is due to the native point defects located at the QW surface. The slight differences found between calculation and experiment are probably due to the fact that we neglect in the calculation the influence of the defects located outside of the area of figure 4.7(a).

4.3.3 Hydrogenic bound states induced by positively charged native point defects

Let us now study the influence of quantum confinement on hydrogenic bound states formed in the $In_{0.53}Ga_{0.47}As$ QW. We investigate the structure of type II [figure 4.2(a)], where there is no electron in the QW. The absence of electrons in the QW allows us to consider the simple case where there is no screening effect.

Figure 4.8(a) shows a STM topographic image of the $In_{0.53}Ga_{0.47}As$ QW surface, for $l = 10$ nm. A positively charged native point defect is visible, appearing as a protrusion. Note that for all the defects, the corrugation at $U \approx +1$ V is 0.15 ($\pm$ 0.05) nm.[8] Figure 4.8(b) shows the same defect as in figure 4.8(a), but at larger scale. It can be seen that the defect is isolated on an atomically-flat

[8]The variations of corrugation from defect to defect ($\pm$ 0.05 nm) do not correlate with variations of binding energy and Bohr radius, and are ascribed to slight changes of tip condition.

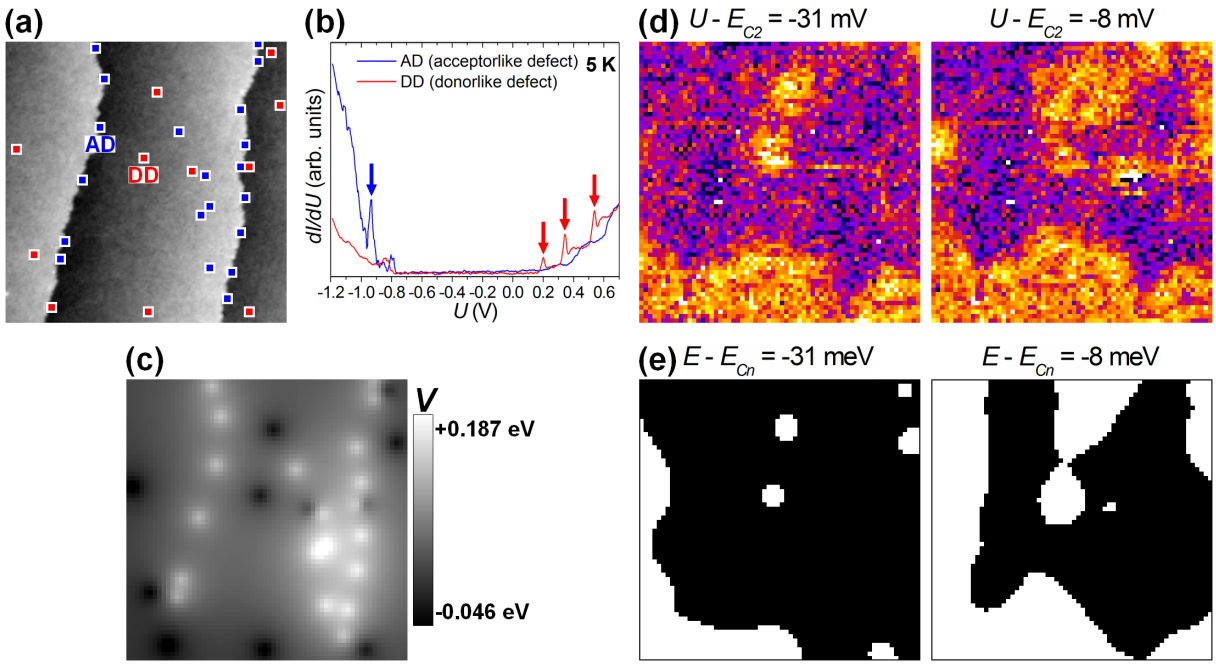

Figure 4.7: (Color) **(a)** STM topographic image of a 96×96 nm^2 area of the $In_{0.53}Ga_{0.47}As$ QW surface ($U = +2.5$ V; $I =$), for the structure of type II with $l = 10$ nm. A dI/dU spectrum was acquired on each pixel of a 64×64 grid of this area, for U ranging from -1.2 V to +1 V. The positions of the negatively and positively charged native point defects found in this area are indicated by blue and red squares, respectively. **(b)** dI/dU spectra averaged over the square areas AD (negatively charged defect, blue curve) and DD (positively charged defect, red curve) indicated in (a). **(c)** Calculated spatial map of the potential $V(\mathbf{r})$, in the same area as in (a). See the text for details about the calculation of $V(\mathbf{r})$. **(d)** dI/dU spatial maps of the same area as in (a), at two different values of U. The values of U are given with respect to the experimentally determined percolation threshold for the second subband, E_{C2}. **(e)** Calculated spatial maps of the LDOS of the nth subband, in the same area as in (a), at two different energies E. The energies E are given with respect to the theoretical percolation threshold for the nth subband, $E_{Cn} = E_n + \bar{V}$. White and black regions correspond to nonzero and zero LDOS, respectively. See the text for details about the calculation of the LDOS.

terrace, with no other defects in the vicinity (the mottled appearance of the terrace is due to local fluctuations of the InGaAs alloy composition, as explained in section 3). A dI/dU spectrum was acquired on each pixel of a 64×64 grid of the area of figure 4.8(b), for U ranging from 0 V to +1 V (CB region). Figure 4.8(c) shows the dI/dU spectra averaged over rings of thickness 1 nm and of several radii r, centered on the defect. The dI/dU spectrum at $r = 9.7$ nm has a step-like voltage dependence, as expected for a 2DES. The steps correspond to the subbands formed in the QW due to quantum confinement along the growth direction. The dI/dU spectrum at $r = 9.7$ nm also exhibits a peak below each subband minimum. The height of these peaks increases as r decreases. The peak found below the nth subband minimum is interpreted as a bound state splitting off from the nth subband, due to an attractive potential created by the defect [134]. Bound states splitting off from a two-dimensional continuum have been recently observed by STS measurements on metal surface states [61,65,66] or $ErSi_2$ layers [73]. In contrast to those works, here it is possible to study the influence of quantum confinement on the bound states, by simply varying l.

Note that the bound state peaks move to lower U when r increases, as it can be seen in figure 4.8(c). The origin of this shift is unknown. Since it has a small amplitude (about 10 mV between $r = 0.9$ nm and $r = 9.7$ nm, which is comparable to U_{mod}), it will be neglected in the following. At $r = 0.9$ nm, the bound states are located at $U = \varepsilon_1$, ε_2, and ε_3.

Note also that the peak at $U = E_A$ in figure 4.8(c) is only found for $r < 2$ nm (i.e., in the immediate vicinity of the defect), while the bound state peaks can be observed up to $r \approx 13$ nm. For all the defects, E_A is 0.5 ($\pm$ 0.05) eV above the CB minimum, independently of l.

Figure 4.8(d) shows the dI/dU spatial maps at $U = \varepsilon_1$, ε_2, and ε_3. The wave functions of the bound states are not completely isotropic, but are slightly elongated in one particular direction. The exact shape of the wave functions was found to vary from defect to defect. This is consistent with the fact that a disorder potential is present in the QW (section 4.3.2). The disorder potential, superimposed on the central potential of the defect, induces a small distortion of the wave functions of the bound states.

The spatial extension of the wave functions of the bound states can be precisely determined by plotting the height of the corresponding dI/dU peaks as a function of r. Figure 4.8(e) shows the case of the bound state attached to the first subband.[9] The obtained spatial dependence is well

[9]The dI/dU peak height is plotted for $r > 2$ nm. For $r < 2$ nm, the defect is visible in the STM topography,

fitted by an exponential decay $A \exp(-2r/a_{B1})$, representing the 1s hydrogenic wave function. The fit leads to the Bohr radius for the first subband, $a_{B1} = 6.8\ (\pm\ 1)$ nm. The Bohr radii determined in a similar way for high-order subbands are $a_{B2} = 6.1\ (\pm\ 1)$ nm and $a_{B3} = 5.4\ (\pm\ 1)$ nm.

Having shown how to determine the Bohr radius of a positively charged native point defect, we now present a method for determining the binding energy. The binding energy is defined as the difference between the energy of the bound state and that of the subband minimum. On one hand, the bound state peaks appear the most clearly in the dI/dU spectra acquired close to the defect. Therefore, the bound state energies ε_n were determined from the dI/dU spectrum at the smallest measured radius, $r = 0.9$ nm. On the other hand, the steps associated with the subband minima appear the most clearly in the dI/dU spectra acquired far from the defect. From about $r = 2a_{B1}$, the dI/dU spectra exhibit a clear step-like voltage dependence, the bound state peaks having completely vanished. Therefore the subband minima E_n were determined from the dI/dU spectrum at $r = 2a_{B1}$ (for a precise determination of the energy position of the steps, the derivative of the dI/dU spectrum at $r = 2a_{B1}$ was calculated and then fitted by Gaussian functions). Figure 4.9 illustrates this method for three different values of l.

Figure 4.10 summarizes the STS data obtained in this work. The smaller l, the larger $E_1 - \varepsilon_1$ and the smaller a_{B1}, i.e., the tighter the electron is bound to the positively charged native point defect. Thus we clearly observe the influence of quantum confinement on the bound states, as expected in the present case where l is comparable with a_{B1} [132]. Note that for a given value of l, different defects do not have exactly the same $E_1 - \varepsilon_1$ or the same a_{B1}. This can be explained by the presence of a disorder potential in the QW (section 4.3.2).

We now compare the STS data with a calculation of hydrogenic impurity states. The effect of tip-induced band bending on the bound states was neglected.[10] However, the CB nonparabolicity was taken into account, since it plays a significant role in $In_{0.53}Ga_{0.47}As$ (section 3.3.2). The method proposed in Ref. [133] was employed. It consists of two steps. In the first step, the energies E_n were determined with respect to the CB minimum by solving the one-dimensional Schrödinger equation

hence the r-dependence of dI/dU may reflect a variation of tip-sample distance (appendix A).

[10] Tip-induced band bending (appendix B) was estimated by assuming that the density of surface states is zero, and that the unintentional n-type impurity density in the nominally undoped $In_{0.53}Ga_{0.47}As$ layer is about 1×10^{15} cm^{-3} [117]. For $U > 0$, the space-charge layer thickness was found to be larger than 100 nm, hence much larger than a_{B1}.

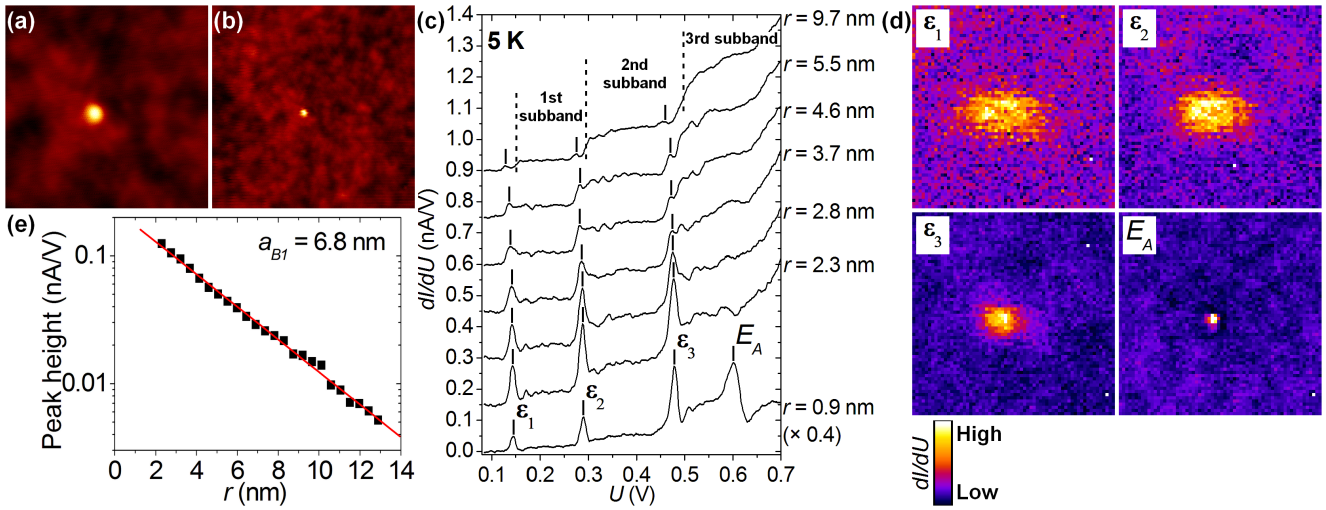

Figure 4.8: (Color) Determination of the Bohr radius of a positively charged native point defect at the $In_{0.53}Ga_{0.47}As$ QW surface, for the structure of type II with $l = 10$ nm. **(a)** 10.7×10.7 nm^2 STM topographic image ($U = +1.1$ V; $I = 0.1$ nA). A positively charged native point defect (bright spot) is visible. **(b)** 29.5×29.5 nm^2 STM topographic image ($U = +1.1$ V; $I = 0.5$ nA), showing the same defect as in (a). A dI/dU spectrum was acquired simultaneously to the STM topography, on each pixel of a 64×64 grid, for U ranging from 0 V to +1 V (CB region). **(c)** dI/dU spectra averaged over rings of thickness 1 nm and of several radii r, centered on the defect (for clarity, the spectra are offset by a constant of 0.15 nA/V, relative to the lowest curve; the ordinate axis for the spectrum at $r = 0.9$ nm is multiplied by 0.4). Three subbands are observed in the present case where $l = 10$ nm, in agreement with the calculations detailed in the text. A peak is found near each subband minimum, as indicated by vertical lines. For the dI/dU spectrum at $r = 0.9$ nm, these peaks are found at $U = \varepsilon_1$, ε_2, and ε_3. **(d)** dI/dU spatial maps of the same area as in (b), at several values of U indicated in (c). **(e)** Height of the dI/dU peak attached to the first subband as a function of distance r from the defect (squares). Also shown is a fit by an exponential decay $A\exp(-2r/a_{B1})$ (red line). The fit leads to a Bohr radius for the first subband, $a_{B1} = 6.8\ (\pm\ 1)$ nm. Note that the ordinate axis has a logarithmic scale.

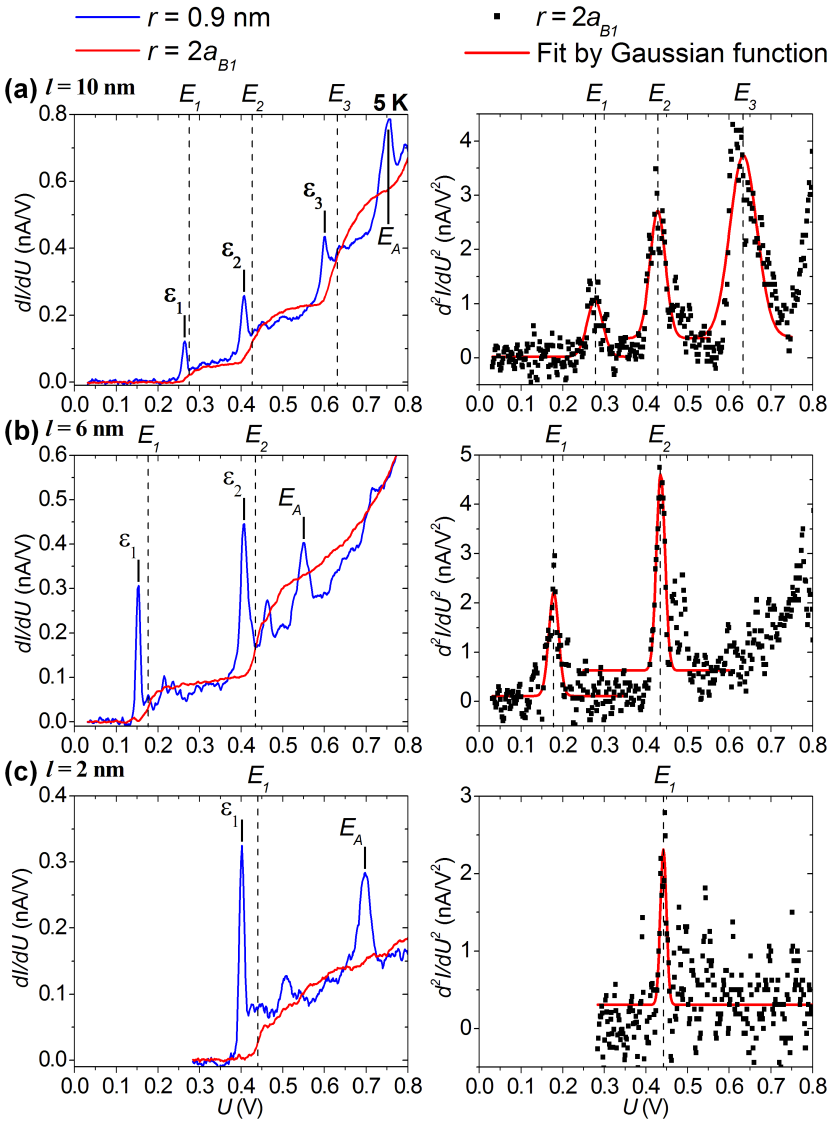

Figure 4.9: (Color) Determination of the binding energy of a positively charged native point defect at the $In_{0.53}Ga_{0.47}As$ QW surface, for the structure of type II. An analysis similar to that of figure 4.8 leads to the Bohr radius for the first subband, a_{B1}. The energy of the bound state attached to the nth subband, ε_n, is determined from the dI/dU spectrum at $r = 0.9$ nm. The nth subband minimum, E_n, is determined from the d^2I/dU^2 spectrum at $r = 2a_{B1}$. The binding energy for the nth subband is then given by $E_n - \varepsilon_n$. (a) $l = 10$ nm, for a defect with $a_{B1} = 7.3$ ($\pm$ 1) nm. (b) $l = 6$ nm, for a defect with $a_{B1} = 5.15$ ($\pm$ 1) nm. (c) $l = 2$ nm, for a defect with $a_{B1} = 4.4$ ($\pm$ 1) nm. Three subbands are observed for $l = 10$ nm, two subbands for $l = 6$ nm, and one subband for $l = 2$ nm, in agreement with the calculations detailed in the text. Note that the disorder potential in the QW induces a rigid shift of subband minima when the spatial position changes (section 4.3.2). Therefore one can only compare the subband *spacings* in dI/dU spectra for different defects.

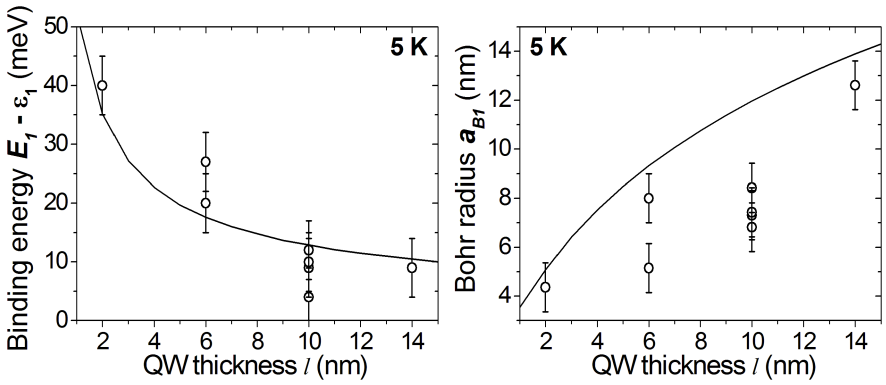

Figure 4.10: Binding energy $E_1 - \varepsilon_1$ and Bohr radius a_{B1} of positively charged native point defects as a function of the $In_{0.53}Ga_{0.47}As$ QW thickness l: STS data (each circle corresponds to a single defect), and variational calculation of hydrogenic impurity states including the CB nonparabolicity (solid curves).

in the $In_{0.53}Ga_{0.47}As/In_{0.52}Al_{0.48}As$ QW structure, as described above (section 4.3.1). For a given value of l, the number of subbands found by solving the Schrödinger equation agrees with the STS data.[11] In the second step, $E_1 - \varepsilon_1$ and a_{B1} were determined by using a variational calculation for an electron bound to a point charge $+e$ [132]. The point charge was taken to be at the QW boundary, since the defects are located at the QW surface. The dielectric constant was that for a point charge at the interface between $In_{0.53}Ga_{0.47}As$ and vacuum (appendix E), given by $\epsilon = \frac{\epsilon_0 + \epsilon_{bulk}}{2}$ ($\epsilon_{bulk} = 13.75\epsilon_0$ is the dielectric constant of $In_{0.53}Ga_{0.47}As$ [2]). The electron effective mass was given by the two-band Kane model at the energy E_1 determined in the first step. The calculation agrees well with the STS data, as shown in figure 4.10. We emphasize that this calculation has no adjustable parameters. The increase of $E_1 - \varepsilon_1$ (or, equivalently, the decrease of a_{B1}) with decreasing l is enhanced by the CB nonparabolicity. From $l = 14$ nm to $l = 2$ nm, $E_1 - \varepsilon_1$ increases by factors 2.4 and 3.3 without and with considering the CB nonparabolicity, respectively.

We point out that the distribution of LDOS along the growth direction, $|\psi_n(z)|^2$, depends on the subband index n [in the ideal case of a QW with infinite barrier height, $|\psi_n(z)|^2 \propto \sin^2\left(\frac{n\pi z}{l}\right)$ where z is the distance from the QW boundary]. The distance between the QW boundary and the closest maximum of $|\psi_n(z)|^2$ decreases with increasing n (in the case of infinite barrier height, this

[11] The measured subband spacings are between 20 and 30% larger than the calculated ones. As already mentionned (section 4.3.2), this maybe due to a voltage drop in the $In_{0.52}Al_{0.48}As$ barrier. This effect is neglected here [even for the largest measured binding energy (40 meV), a variation of 20-30% is smaller than U_{mod}].

distance is $l/2n$). Therefore the binding of the electron to a defect located at the QW boundary is expected to become tighter for larger n. This is what observed in the STS data of figures 4.8 and 4.9. Further experimental work is needed, e.g., by studying impurities at different positions along the growth direction.

4.4 Summary

In this section, electronic states in (111)A-oriented $In_{0.53}Ga_{0.47}As$ surface QWs grown on top of $In_{0.52}Al_{0.48}As$ barriers were studied by STS. It was shown that:

- Electron subbands are formed in the $In_{0.53}Ga_{0.47}As$ QW, due to quantum confinement along the growth direction. In addition, the electron density can be controlled in the QW, owing to the partial unpinning of the Fermi level at the $In_{0.53}Ga_{0.47}As(111)A$ surface.

- A disorder potential is present in the $In_{0.53}Ga_{0.47}As$ QW. In the case of a multisubband QW, a phenomenon of percolation of localized states occurs in each subband tail. The disorder potential is created by a random distribution of negatively and positively charged native point defects at the QW surface.

- A bound state splits off from each subband minimum in the vicinity of a positively charged native point defect at the $In_{0.53}Ga_{0.47}As$ QW surface. Both the binding energy and the Bohr radius of the bound states can be directly measured. The binding energy and the Bohr radius are functions of the QW thickness, in quantitative agreement with variational calculations of hydrogenic impurity states.

5 Conclusion

Low-temperature STS under UHV was used to study (111)A-oriented $In_{0.53}Ga_{0.47}As$ surface QWs grown by MBE on top of $In_{0.52}Al_{0.48}As$ barriers. The STS measurements were performed at the (111)A epitaxial surface of the $In_{0.53}Ga_{0.47}As$ QW, in order to probe with nanometer-scale resolution the in-plane spatial distribution of LDOS.

It appeared that the (111)A-oriented $In_{0.53}Ga_{0.47}As/In_{0.52}Al_{0.48}As$ materials system offers major advantages for investigating surface QWs by STS:

- The Fermi level is partially unpinned at the (111)A surface of n-type $In_{0.53}Ga_{0.47}As$. Thus the electron density in the QW could be controlled by modulation doping. This important result suggests that it would be possible to tune the electron density in the QW during STS measurements under UHV, by using an electrical gate.

- Native point defects are present at the $In_{0.53}Ga_{0.47}As$(111)A surface, creating a disorder potential in the QW. Thus a STS study of disordered 2DES could be performed, which revealed that a phenomenon of percolation of localized states occurs in each subband tail. For future experiments, it would be interesting to vary the electron density in the QW, in order to investigate many-electron phenomena in disordered 2DES, such as the crossover from linear to nonlinear screening regime [31, 124].

- Among the native point defects found at the $In_{0.53}Ga_{0.47}As$(111)A surface, some are positively charged. Thus a STS study of donor impurities located in a semiconductor QW could be performed. Both the binding energy and the Bohr radius of the bound states could be directly determined. Moreover, it was shown that the binding energy and the Bohr radius are functions of the QW thickness, in quantitative agreement with variational calculations of hydrogenic impurity states. Future experiments could investigate how the bound states are influenced by a perpendicular magnetic field applied in the QW [175, 176]. Even more challenging would be to manipulate with the STM tip the positively charged defects at the QW surface, in order to study artificial nanostructures where the bound states are coherently coupled.

Acknowledgments

Many people have contributed to this PhD thesis. First, I thank the jury members for participating to the defence: Yves Guldner (Université Pierre et Marie Curie, Paris), jury president; Bruno Grandidier (Institut d'Electronique, de Microélectronique et de Nanotechnologie, CNRS, Lille) and Stefan Fölsch (Paul Drude Institute, Berlin, Germany), reviewers; Gerald Bastard (Ecole Normale Supérieure, Paris); Paul Voisin (Laboratoire de Photonique et de Nanostructures, CNRS, Marcoussis); Zhao-Zhong Wang (Laboratoire de Photonique et de Nanostructures, CNRS, Marcoussis) and Kiyoshi Kanisawa (NTT Basic Research Laboratories, NTT Corporation, Atsugi, Japan), advisors. I am particularly indebted to Stefan Fölsch and Kiyoshi Kanisawa, who had to travel long distances in order to attend the defence, from Germany and Japan respectively.

Then, I thank the members of the Quantum Solid State Physics Research Group of the NTT Basic Research Laboratories, where I performed my PhD research from October 2004 to October 2007. I acknowledge Yoshiro Hirayama (now at Tohoku University, Sendai, Japan) and Toshimasa Fujisawa, for welcoming me in the group. I express my deep appreciation to Kiyoshi Kanisawa, my advisor in Japan. Kiyoshi Kanisawa not only taught me in detail the difficult techniques of molecular beam epitaxy and scanning tunneling spectroscopy, but also spent a lot of time and effort to help me overcoming the difficulties we met during my PhD research. Besides his great qualities as a scientist, I am grateful for his kindness and optimism. I am indebted to Kyoichi Suzuki, with whom I had the pleasure to collaborate on his project concerning the InAs/GaSb heterostructures. I wish him great success for future experiments. I am grateful to all the other past or present members, for providing me with an exceptional scientific environment: Paula Giudici, Kasper Grove-Rasmussen, Toshiaki Hayashi, Norio Kumada, Hongwu Liu, Koji Muraki, Takeshi Ota, Vincent Renard, Satoshi Sasaki, Akihito Taguchi, Kei Takashina, and Go Yusa.

I thank A. Takano and S. Mizuno from NTT Advanced Technology, for performing SIMS measurements and scanning transmission electron microscopy characterization, respectively.

I thank the members of the team working on scanning tunneling microscopy at the Laboratoire de Photonique et de Nanostructures. I acknowledge Zhao-Zhong Wang, my advisor in France, for his

continued support in my PhD studies. I am indebted to Jean-Christophe Girard and Christophe David, for helpful discussions. I am especially grateful to Christophe Brun (now at the Ecole Polytechnique Fédérale de Lausanne, Switzerland), both as a scientist and as a friend.

I express my deep appreciation to Sven Lagerwall (Chalmers University of Technology, Göteborg, Sweden) for his precious help when I came back to France in October 2007.

Finally, on a more personal side, I thank the people who made my stay in Japan very much enjoyable. I especially thank Alexander Kasper and Imran Mahboob, I think they know why. I am also grateful to Tobias Bergsten, Serge Camou, Nicolas Clement, Samir Etaki, Paula Giudici, Hideomi Hashiba, Christophe Hufnagel, Daisuke Ito, Jan Johansson, Karin Kallstrom, Wouter Naber, Masashi Ota, Vincent Renard, Jonas Rundqvist, Kei and Kristina Takashina, for all the dinners we had together; Eek Huisman for the road-trip in Kyushu; Isao Tomita and Yung-Joon Jung for keeping in touch after all this time; Ritsuya Tomita, Shoko Utsunomiya, and Kyoko Kaminaga for the karaoke sessions in Shimokitazawa; Naomi Takada for the japanese lessons; Junro Matsuhashi, the owner of a legendary liquor shop in Zama; Hiroko Takeda, Satoru and Yoshiko Yoshikawa, for the wonderful week-ends in the Kansai region; Géraldine Bailly for the letters she sent me from France, Germany, Italy and England; Cyril Arnaud and David Traoré, for visiting me in Japan, where we spent two unforgettable weeks.

A Tunneling current in a perturbative approach

In order to precisely understand the principle of the scanning tunneling microscope [26–30], it is necessary to obtain an analytical expression of the tunneling current flowing between the sample and the metallic probe tip. In this section, we establish a useful formula for the tunneling current and the differential tunneling conductance, by using a simple perturbative model.

We consider that the probe tip and the sample are separated by a sufficiently thick tunneling junction, so that tunneling can be treated in a perturbative approach, as proposed by Bardeen [151]. In addition, we assume elastic tunneling. Within this framework, the probability per unit time of the transition of an electron, from a single-electron state ψ_t of energy E_t on the tip, to a single-electron state ψ_s of energy E_s on the sample, is given by the Fermi golden rule of first-order time-dependent perturbation theory:

$$P_{ts} = \frac{2\pi}{\hbar} |M_{ts}|^2 \, \delta\left(E_t - E_s\right) f(E_t - E_F - eU) \left[1 - f(E_s - E_F)\right] \tag{A.1}$$

where M_{ts} is the tunneling matrix element, $f\left(E\right) = \frac{1}{1+\exp\left(\frac{E}{k_B T}\right)}$ is the Fermi-Dirac function, E_F is the sample Fermi level, and U is the bias voltage applied between the tip and the sample (tip neutral). Note that $E_F + eU$ corresponds to the tip Fermi level. Summing the probabilities per unit time P_{ts} [equation (A.1)] over all states ψ_t and ψ_s leads to the tunneling current from the tip to the sample:

$$I_{TS} = -e \int_{-\infty}^{+\infty} \sum_t \delta\left(E - E_t\right) \sum_s \frac{2\pi}{\hbar} |M_{ts}|^2 \, \delta\left(E - E_s\right) f(E - E_F - eU) \left[1 - f(E - E_F)\right] dE. \tag{A.2}$$

The tunneling current I_{ST} from the sample to the tip is obtained in a similar way. It is then easy to calculate the net tunneling current $I = I_{ST} - I_{TS}$ from the sample to the tip. The result is

$$I = \frac{2\pi e}{\hbar} \int_{-\infty}^{+\infty} \sum_t \delta\left(E - E_t\right) \sum_s |M_{ts}|^2 \, \delta\left(E - E_s\right) \left[f(E - E_F - eU) - f(E - E_F)\right] dE. \tag{A.3}$$

Tersoff and Hamann have modeled the probe tip as a locally spherical potential well where it approaches nearest to the sample surface [152,153]. With this approximation, they have shown that

$$M_{ts} \propto \psi_s(\mathbf{r_0}) \tag{A.4}$$

where $\mathbf{r_0}$ denotes the center of curvature of the tip. The wave functions $\psi_s(x,y,z)$ obey the time-independent Schrödinger equation

$$H_S\psi_s(x,y,z) = E_s\psi_s(x,y,z) \tag{A.5}$$

where H_S is the single-electron Hamiltonian on the sample side, (x,y) are the coordinates in the sample surface plane, and z is the coordinate in the perpendicular direction. We assume that H_S can be written as $H_S = H_{S,xy} + H_{S,z}$, where $H_{S,xy}$ is an operator acting only on the the (x,y) variables, and $H_{S,z}$ an operator acting only on the z variable. In this case, we use the separation of variables $\psi_s(x,y,z) = \psi_s(x,y)\,\psi_s(z)$ and obtain

$$H_{S,xy}\psi_s(x,y) = E_{s,xy}\psi_s(x,y) \tag{A.6}$$

$$H_{S,z}\psi_s(z) = E_{s,z}\psi_s(z) \tag{A.7}$$

with $E_s = E_{s,xy} + E_{s,z}$. In addition, if the tunneling barrier is modeled by a potential step of height $\phi(U)$, then solving equation (A.7) in the tunneling barrier region ($E_{s,z} < \phi$) gives

$$\psi_s(z) \propto \exp(-\kappa z) \tag{A.8}$$

$$\phi(U) - E_{s,z} = \frac{\hbar^2\kappa^2}{2m_0} \tag{A.9}$$

where m_0 is the free-electron mass. Together, equations (A.4), (A.8) and (A.9) lead to

$$M_{ts} \propto \psi_s(x_0,y_0)\exp\left[-z_0\frac{\sqrt{2m_0\left[\phi(U)-E_{s,z}\right]}}{\hbar}\right] \tag{A.10}$$

with $\mathbf{r_0} \equiv (x_0,y_0,z_0)$, z_0 being the distance between the sample surface and the center of curvature of the tip. It is usually assumed that $E_{s,z} \simeq E_s$. With this approximation, injecting equation (A.10) into equation (A.3) gives

$$I(U,x_0,y_0,z_0) \propto \int_{-\infty}^{+\infty} N_T(E)\,N_S(E,x_0,y_0)\,D(E,U,z_0)\left[f(E-E_F-eU)-f(E-E_F)\right]dE \tag{A.11}$$

where

- $N_T(E) = \sum_t \delta(E - E_t)$ is the density of states on the probe tip,
- $N_S(E, x_0, y_0) = \sum_s \delta(E - E_s) |\psi_s(x_0, y_0)|^2$ is the local density of states at the sample surface,
- $D(E, U, z_0) = \exp\left[-2z_0 \frac{\sqrt{2m_0[\phi(U) - E]}}{\hbar}\right]$ is the transmission coefficient of the tunneling barrier.

At low temperature, equation (A.11) becomes

$$I(U, x_0, y_0, z_0) \propto \int_{E_F}^{E_F + eU} N_T(E)\, N_S(E, x_0, y_0)\, D(E, U, z_0)\, dE \tag{A.12}$$

which is actually the expression proposed by Lang [154].[1]

If N_T is independent of energy, then the differential conductance derived from equation (A.12) has a simple expression:

$$\frac{dI}{dU} \propto eD(E_F + eU, U, z_0) N_S(E_F + eU, x_0, y_0) + \int_{E_F}^{E_F + eU} \frac{dD}{dU} N_S(E, x_0, y_0) dE. \tag{A.13}$$

The tunneling barrier height is usually taken to be $\phi(U) = \frac{E_F + \phi_S + E_F + eU + \phi_T}{2}$, i.e., an average between the height $E_F + \phi_S$ (ϕ_S sample work function) on the sample side and the height $E_F + eU + \phi_T$ (ϕ_T tip work function) on the tip side. In this case, $D(E_F, U, z_0) = \exp\left[-2z_0 \frac{\sqrt{2m_0[(\phi_S + \phi_T + eU)/2]}}{\hbar}\right]$. Thus, as long as eU is small compared to ϕ_S and ϕ_T, equation (A.13) simplifies as

$$\frac{dI}{dU} \propto D(z_0) N_S(E_F + eU, x_0, y_0). \tag{A.14}$$

Equation (A.14) indicates that the differential conductance dI/dU at sample voltage U is proportional to the local density of states at the sample surface at energy $E_F + eU$, if the tip-sample separation z_0 is constant. This equation is usually employed for interpreting scanning tunneling microscopy data. However, it cannot be used in the particular case where the sample is a semiconductor, with E_F lying in the conduction band, and $E_F + eU$ lying in the band gap [155]. In such situation, the first term in equation (A.13) equals zero (because N_S at $E_F + eU$ equals zero), but

[1] In Ref. [154], the energies E_t and E_s are measured with respect to the bottom of the band on the tip side and on the sample side, respectively. Thus the formula for the tunneling current at low temperature has a slightly different form.

the second term is nonzero (because N_S is nonzero between E_F and the conduction-band minimum, and D depends on U). In other words, N_S is zero at $E_F + eU$, but dI/dU is nonzero at U. A similar situation happens if E_F lies in the valence band.

B Fermi level position in semiconductors

In this section, we present a general method for determining the Fermi level position with respect to bulk band edges in a semiconductor. We show in detail how to calculate the Fermi level position in the bulk of a semiconductor, at a semiconductor free surface, at a metal-insulator-semiconductor (MIS) junction, and at a metal-semiconductor contact.

We make the following assumptions:

- Thermal equilibrium is reached. Hence the Fermi level E_F is constant throughout the semiconductor.
- The semiconductor is uniformly doped, with ρ_D and ρ_A the volume densities of donor impurities and acceptor impurities, respectively.
- If a potential $V(z)$ is superimposed on the periodic potential of the semiconductor crystal, then single-electron energies are shifted by $+V(z)$. Specifically, the conduction-band minimum E_C becomes $E_C(z) = E_C + V(z)$, and the other energy levels experience the same shift: the valence-band maximum is written as $E_V(z) = E_C(z) - E_G$ (with E_G fundamental band gap), the donor impurity level as $E_D(z) = E_C(z) - \Delta_D$ (with Δ_D donor binding energy), and the acceptor impurity level as $E_A(z) = E_C(z) - E_G + \Delta_A$ (with Δ_A acceptor binding energy). Such an approximation corresponds to a semiclassical model [149]. In the present case where the impurity concentrations are uniform in the semiconductor, the potential $V(z)$ arises solely due to the presence of the surface. Hereafter, z denotes the distance from the surface.

B.1 Volume density of charge

The volume density of charge in the semiconductor is given by

$$\rho(z) = e\left[p(z) - n(z) + \rho_{D+}(z) - \rho_{A-}(z)\right] \tag{B.1}$$

where

- $n(z)$ and $p(z)$ are the volume densities of electrons and holes, respectively. $n(z)$ and $p(z)$ are determined by using Fermi-Dirac statistics:

$$n(z) = \int_0^{+\infty} N_C(E) \frac{1}{1 + \exp\left[\frac{E_C(z)+E-E_F}{k_B T}\right]} dE \tag{B.2}$$

$$p(z) = \int_0^{+\infty} N_V(E) \frac{1}{1 + \exp\left[\frac{E_F-E_V(z)+E}{k_B T}\right]} dE \tag{B.3}$$

where $N_C(E)$ and $N_V(E)$ are the densities of states (per volume unit) in the conduction band and in the valence band, respectively. For parabolic bands

$$N_C(E) = \frac{m_C}{\pi^2 \hbar^3} \sqrt{2 m_C E} \tag{B.4}$$

$$N_V(E) = \frac{m_V}{\pi^2 \hbar^3} \sqrt{2 m_V E} \tag{B.5}$$

where m_C and m_V are the effective masses in the conduction band and in the valence band, respectively. For a conduction-band dispersion relation given by a two-band Kane model including nonparabolicity effects [equation (C.15)]

$$N_C(E) = \frac{m_C}{\pi^2 \hbar^3} \sqrt{2 m_C E \left(1 + \frac{E}{E_G}\right)} \left(1 + \frac{2E}{E_G}\right). \tag{B.6}$$

- $\rho_{D+}(z)$ and $\rho_{A-}(z)$ are the volume densities of donor impurity states which are empty and of acceptor impurity states which are filled, respectively. In the case of nondegenerate doping levels, $\rho_{D+}(z)$ and $\rho_{A-}(z)$ are determined by using Fermi-Dirac statistics:

$$\rho_{D+}(z) = \frac{\rho_D}{1 + \exp\left[\frac{E_F-E_D(z)}{k_B T}\right]} \tag{B.7}$$

$$\rho_{A-}(z) = \frac{\rho_A}{1 + \exp\left[\frac{E_A(z)-E_F}{k_B T}\right]}. \tag{B.8}$$

In the case of degenerate doping levels, $\rho_{D+}(z)$ and $\rho_{A-}(z)$ are simply given by:

$$\rho_{D+}(z) = \rho_D \tag{B.9}$$

$$\rho_{A-}(z) = \rho_A. \tag{B.10}$$

B.2 Fermi level position in the bulk of a semiconductor

The Fermi level position in the bulk of the semiconductor, $E_F - E_C(+\infty)$, is determined by the condition of charge neutrality in the bulk

$$\rho(+\infty) = 0. \tag{B.11}$$

Solving equation (B.11) for a typical semiconductor material, it is found that the bulk Fermi level position can be precisely tuned by varying the impurity density [2].

B.3 Surface density of charge

The Fermi level position at the semiconductor surface, $E_F - E_C(0)$, is usually different from that in the bulk, $E_F - E_C(+\infty)$. If so, bulk band edges bend in the near-surface region, i.e., a space-charge layer is formed. The surface density of charge at the semiconductor surface can be written as

$$\sigma = \sigma_{space} + e(\sigma_{D+} - \sigma_{A-}) \tag{B.12}$$

where

- σ_{space} is the surface density of space charge in the near-surface region. It can be determined in a simple way if one assumes a rectangular profile for the volume density of space charge, i.e., $\rho(z) = \rho(0)$ for $0 < z < Z_0$, where Z_0 is the thickness of the space-charge layer. Solving the Poisson equation in this case leads to

$$Z_0 = \sqrt{\frac{2\epsilon_S [E_C(0) - E_C(+\infty)]}{e\rho(0)}} \tag{B.13}$$

  where ϵ_S is the dielectric constant in the semiconductor, and $E_C(+\infty) - E_C(0)$ corresponds to the band bending in the space-charge layer. σ_{space} is then simply given by

$$\sigma_{space} = \rho(0) Z_0. \tag{B.14}$$

- σ_{D+} and σ_{A-} are the surface densities of donorlike surface states which are empty and of acceptorlike surface states which are filled, respectively. In the model proposed by Bardeen [159], one assumes that the donorlike (acceptorlike) surface states lie below (above) $E_{CNL}(0)$, where $E_{CNL}(z) = E_C(z) - \Delta_{CNL}$ is the so-called charge neutrality level and Δ_{CNL} is an energy characteristic of the semiconductor.[1] Thus, if $E_F - E_C(0)$ is larger (smaller) than $-\Delta_{CNL}$, then surface states carry a negative (positive) charge. In the Bardeen model [159], σ_{D+} and σ_{A-} are determined by using Fermi-Dirac statistics:

$$\sigma_{D+} = \int_0^{+\infty} N_D(E) \frac{1}{1 + \exp\left[\frac{E_F - E_C(0) + \Delta_{CNL} + E}{k_B T}\right]} dE \tag{B.15}$$

$$\sigma_{A-} = \int_0^{+\infty} N_A(E) \frac{1}{1 + \exp\left[\frac{E_C(0) - \Delta_{CNL} + E - E_F}{k_B T}\right]} dE \tag{B.16}$$

where $N_D(E)$ and $N_A(E)$ are the densities of states (per surface unit) in the bands of donorlike surface states and of acceptorlike surface states, respectively.

B.4 Fermi level position at a semiconductor free surface

At a semiconductor free surface, the Fermi level position $E_F - E_C(0)$ is determined by the condition of charge neutrality

$$\sigma = 0, \tag{B.17}$$

i.e., the space charge in the near-surface region must compensate the charge carried by surface states.

Employing such a method for calculating the surface Fermi level position, Bardeen [159] has shown that the surface Fermi level tends to be pinned to energies where the density of surface states is high.[2]

[1] In models based on virtual-induced gap states [160, 161], E_{CNL} corresponds to the effective center of the bulk band gap. In models based on disorder-induced gap states [162] or amphoteric defects [163], E_{CNL} corresponds to the average energy of the sp^3 hybrids. In the three types of model, the obtained E_{CNL} is located about 5 eV below the vacuum level, and lies in the band gap for most semiconductors (i.e., Δ_{CNL} is usually positive).

[2] Fermi level pinning is a general phenomenon, which is not limited to the case of semiconductor surfaces. In any

Two extreme cases can be considered depending on the density of surface states. If the density of surface states is low [figure B.1(a)], then the surface Fermi level is weakly pinned, thus the surface Fermi level position can be readily controlled by changing the impurity density. On the contrary, if the density of surface states is high [figure B.1(b)], then the surface Fermi level is strongly pinned, thus the surface Fermi level position remains almost constant over a wide range of impurity density.

The Fermi level pinning phenomenon has been observed experimentally at the following clean crystalline surfaces in ultrahigh vacuum (UHV)[3]:

- Si(111)-(2×1) cleaved surface. The surface Fermi level is strongly pinned in the band gap by intrinsic surface states originating from the (2×1) reconstruction [91, 92].
- Si(001)-(2×1) surface prepared by annealing. The situation is similar to the case of the Si(111)-(2×1) cleaved surface [92, 93].
- (001)-(2×4) epitaxial surfaces of $In_xGa_{1-x}As$. The surface Fermi level is strongly pinned by extrinsic surface states, i.e., surface states related to defects (adatoms, vacancies, steps, dislocations, etc.). At the GaAs(001)-(2×4) surface, the Fermi level is pinned around midgap by kinks in the As-dimer-vacancy rows of the (2×4) reconstruction [94, 95]. At the $In_{0.53}Ga_{0.47}As$(001)-(2×4) surface, the Fermi level is also pinned around midgap [96], probably for the same reasons as for GaAs. At the InAs(001)-(2×4) surface, the surface Fermi level is pinned in the conduction band [97, 98], but the exact nature of the defects responsible for Fermi level pinning has not been identified so far.

A noticeable exception is the (110) clean surface of III-V compound semiconductors cleaved in UHV. Since the density of surface states is very low in the band gap, the surface Fermi level is mostly unpinned [164].

---

electronic system, if the Fermi level is located in a region where the density of electronic states is high, then even a large change in the amount of charge carried by the states corresponds to only a slight shift in the Fermi level position. Therefore the Fermi level is pinned to energies where the density of states is high.

[3]Crystalline surfaces in a UHV environment are model systems with a well-defined atomic structure, and thus are often used in the field of surface science.

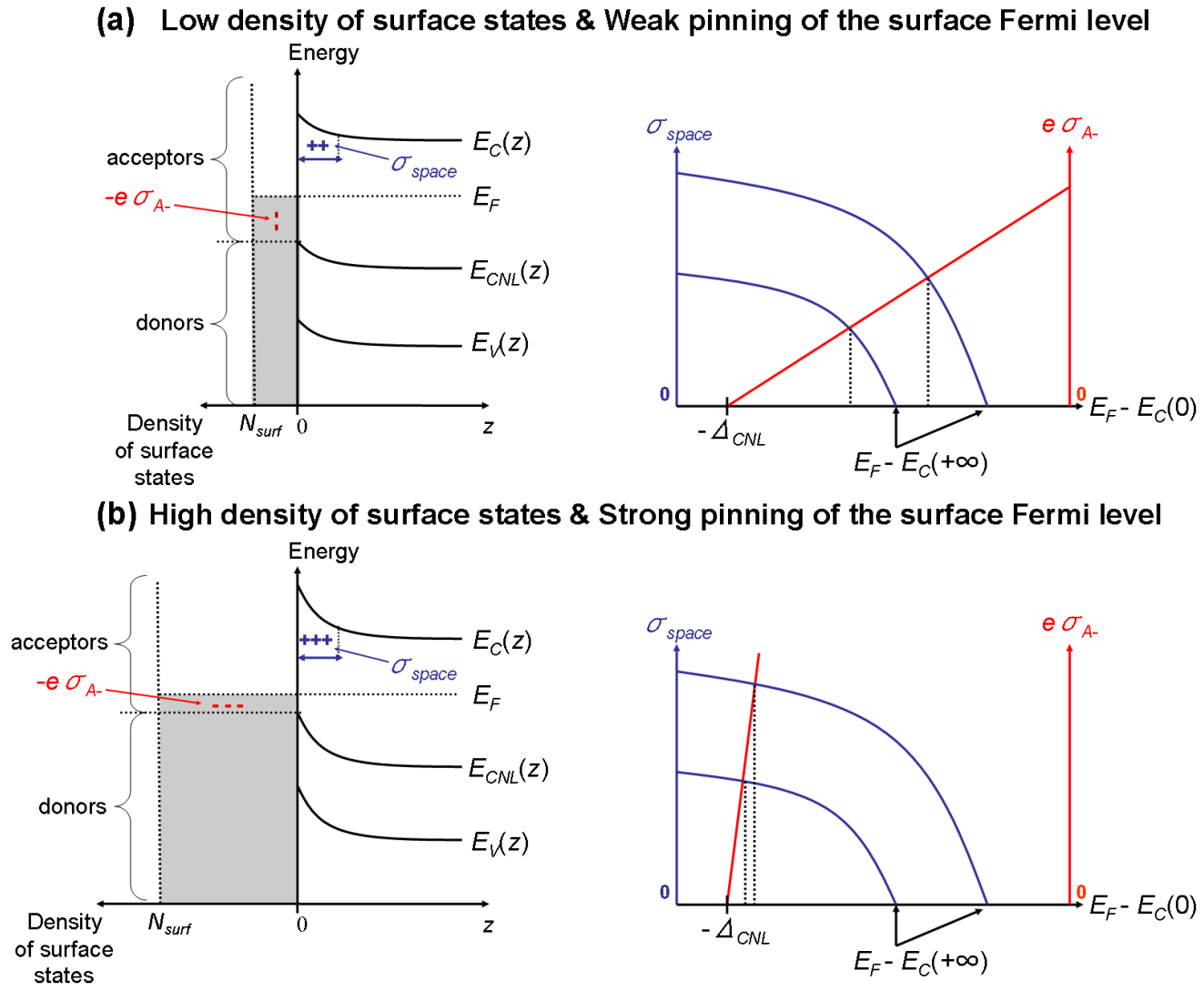

Figure B.1: (Color) Determination of the Fermi level position at a semiconductor free surface, $E_F - E_C(0)$, in the Bardeen model [159]. The method is illustrated in the case where E_F lies in the band of acceptorlike surface states [i.e., E_F lies above the charge neutrality level $E_{CNL}(0) = E_C(0) - \Delta_{CNL}$]. Furthermore, it is assumed that the density of states in the band of acceptorlike surface states is independent of energy [$N_A(E) = N_{surf}$], hence the density of filled acceptor surface states is simply given by $\sigma_{A-} = [E_F - E_C(0) + \Delta_{CNL}]\, N_{surf}$. The density of space charge in the near-surface region, σ_{space}, is given by equation (B.14). $E_F - E_C(0)$ is given by equation (B.17). **(a)** If N_{surf} is low, then varying the impurity density [i.e., varying the bulk Fermi level position $E_F - E_C(+\infty)$] allows to vary $E_F - E_C(0)$. **(b)** If N_{surf} is high, then varying the impurity density has almost no effect on $E_F - E_C(0)$.

B.5 Fermi level position at a MIS junction

Let us consider the MIS junction shown in figure B.2. At the semiconductor-insulator interface, the Fermi level position $E_F - E_C(0)$ is determined by the condition of charge neutrality

$$\sigma + \sigma_M = 0, \tag{B.18}$$

where σ_M is the surface density of charge on the metal surface. Equation (B.18) means that the charge on the metal must compensate the total charge on the semiconductor. σ_M is given by

$$\sigma_M = C_I \left[\Phi(-z_0) - \Phi(0)\right], \tag{B.19}$$

where $C_I = \epsilon_I / z_0$ is the insulator capacitance per unit area, ϵ_I is the dielectric constant in the insulator, z_0 is the thickness of the insulator, and $\Phi(-z_0) - \Phi(0)$ is the drop of electrostatic potential across the insulator. $\Phi(-z_0) - \Phi(0)$ is related to the bias voltage U applied between the metal and the semiconductor (figure B.2):

$$e\left[\Phi(0) - \Phi(-z_0)\right] = eU + e\phi - e\chi + E_F - E_C(0), \tag{B.20}$$

where $e\chi$ is the electron affinity of the semiconductor, and $e\phi$ is the work function of the metal.

Again, two extreme cases can be considered depending on the density of surface states. If the density of surface states is high, then the surface Fermi level is weakly pinned, thus the surface Fermi level position remains almost constant over a wide range of bias voltage. In other words, electrons in surface states efficiently screen the charge on the metal, and most of the electrostatic potential applied between the metal and the semiconductor is dropped in the insulating layer. On the contrary, if the density of surface states is low, then the surface Fermi level is weakly pinned, thus the surface Fermi level position strongly depends on the bias voltage. In other words, electrons in surface states cannot completely screen the charge on the metal, and some of the electrostatic potential applied between tip and semiconductor is dropped in the semiconductor itself.

The strength of Fermi level pinning at the semiconductor-insulator interface of MIS junctions is an extremely important issue in semiconductor physics and technology, in particular for

- The realization of a MIS field-effect transistor. If the Fermi level pinning at the semiconductor-insulator interface is too strong, then the Fermi level position cannot be controlled by varying

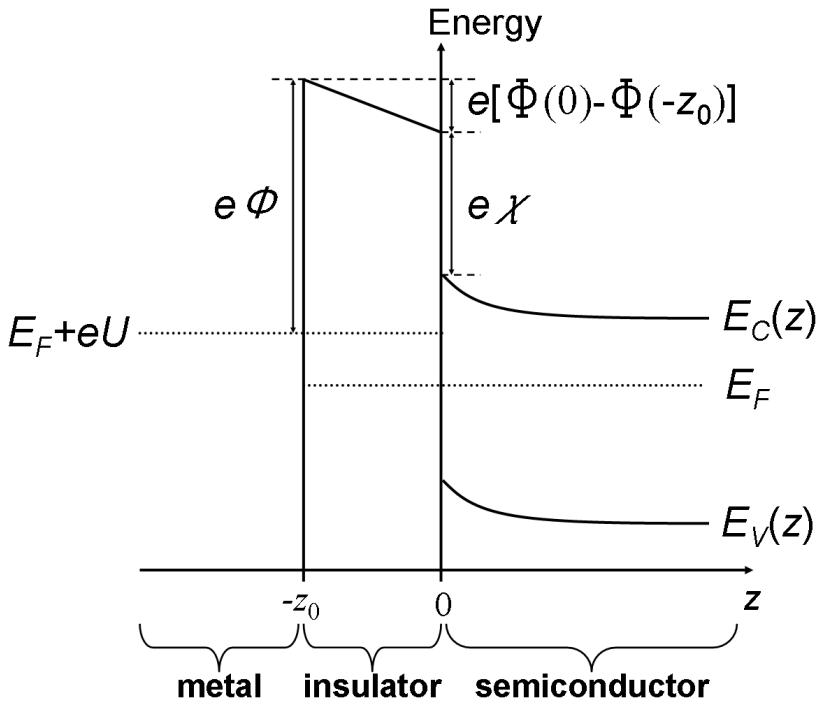

Figure B.2: Schematic band diagram of a planar metal-insulator-semiconductor (MIS) junction. E_F is the Fermi level in the semiconductor, $E_F + eU$ is the Fermi level in the metal, U is the bias voltage applied between the metal and the semiconductor, $e\chi$ is the electron affinity of the semiconductor, z_0 is the thickness of the insulator, and $e\phi$ is the work function of the metal.

the bias voltage, hence the MIS junction cannot be used for building a field-effect transistor [165]. The strength of Fermi level pinning can be reduced at Si-SiO_2 interfaces by hydrogen annealing [2], but pinning is much more difficult to suppress in the case of III-V compound semiconductors in spite of considerable effort to develop new insulating materials [166–169]. This is one of the main reason why silicon is preferred to III-V compound semiconductors for the realization of MIS field-effect transistors.

- The interpretation of data in scanning tunneling microscopy of semiconductor surfaces. If the Fermi level pinning at the semiconductor surface is too weak, then the surface Fermi level position changes with the bias voltage, an effect known as tip-induced band bending [170–173].

B.6 Fermi level position at a metal-semiconductor contact

The case of metal-semiconductor contacts can be treated in the same way as the case of MIS junctions. Specifically, following Bardeen [159], a metal-semiconductor contact is modeled as a metal-vacuum-semiconductor junction, i.e., a MIS junction where the insulator is vacuum.

An important parameter for a metal-semiconductor contact is the barrier height [2]. For a n-type semiconductor, the barrier height $e\phi_{Bn}$ is defined as the value of $E_C(0) - E_F$ at $U = 0$. Equation (B.20) immediately gives

$$\phi_{Bn} = \phi - \chi - [\Phi(0) - \Phi(-z_0)]\,. \tag{B.21}$$

In equation (B.21), the term $\phi - \chi$ corresponds to the barrier height in the Schottky-Mott model, while the term $\Phi(0) - \Phi(-z_0)$ corresponds to the interface dipole due to the presence of surface states.

C Conduction-band dispersion relation in the two-band Kane model

The conduction band of narrow-gap semiconductors departs from the simple parabolic form in the experimentally attainable range of carrier concentrations, as observed, e.g., in InSb and InAs [156]. In this section, we establish an expression for the conduction-band dispersion relation which includes such nonparabolicity effects. We consider the case of direct-gap III-V compound semiconductors and use the $\mathbf{k}\cdot\mathbf{p}$ method as introduced by Kane [7, 157, 158].

In a crystalline solid, the single-electron time-independent Schrödinger equation is

$$\left[\frac{\mathbf{p}^2}{2m_0} + V(\mathbf{r})\right]\psi(\mathbf{r}) = E\psi(\mathbf{r}) \tag{C.1}$$

where $\mathbf{p} = \frac{\hbar}{i}\nabla$ is the momentum operator, m_0 is the free-electron mass, and $V(\mathbf{r})$ is a periodic potential with the periodicity of the crystal. Spin-orbit coupling has been neglected. The solutions of equation (C.1) can be written as Bloch waves

$$\psi_{n\mathbf{k}}(\mathbf{r}) = u_{n\mathbf{k}}(\mathbf{r})\exp(i\mathbf{k}\cdot\mathbf{r}) \tag{C.2}$$

of energy $E_n(\mathbf{k})$. Here, $u_{n\mathbf{k}}(\mathbf{r})$ is a periodic function of $\mathbf{r}$ with the periodicity of the crystal, n is the band index, and $\mathbf{k}$ is the crystal wave vector. Injecting equation (C.2) into equation (C.1) gives

$$\left[\frac{\mathbf{p}^2}{2m_0} + V(\mathbf{r}) + \frac{\hbar}{m_0}\mathbf{k}\cdot\mathbf{p}\right]u_{n\mathbf{k}}(\mathbf{r}) = \left(E_n(\mathbf{k}) - \frac{\hbar^2\mathbf{k}^2}{2m_0}\right)u_{n\mathbf{k}}(\mathbf{r}). \tag{C.3}$$

The third term in equation (C.3) is referred to as the $\mathbf{k}\cdot\mathbf{p}$ interaction, and involves the momentum operator $\mathbf{p}$. We want to determine the shape of the energy bands $E_n(\mathbf{k})$ in the vicinity of some special point $\mathbf{k_0}$ of the first Brillouin zone, from the knowledge of the energies $E_n(\mathbf{k_0})$ and of the matrix elements of the momentum operator at $\mathbf{k_0}$. Such an analysis is known as the $\mathbf{k}\cdot\mathbf{p}$ formalism [7].

In the case of direct-gap III-V compound semiconductors

- The band extrema occur at the center of the first Brillouin zone, the so-called Γ point. Thus we apply the $\mathbf{k}\cdot\mathbf{p}$ formalism for $\mathbf{k}$ around $\mathbf{k_0}=0$.

- The lowest conduction band and the three topmost valence bands are close and well separated from the other bands, especially for narrow-gap semiconductors such as InSb or InAs. Thus, following the Kane model [7, 157, 158], we solve Eq. (C.3) exactly within the limited set of bands consisting of the lowest conduction band ($n=1$) and the three topmost valence bands ($n=2$,3,4). Therefore the functions $u_{n\mathbf{k}}(\mathbf{r})$ can be expressed as

$$u_{n\mathbf{k}}(\mathbf{r}) = \sum_{m=1}^{4} c_{nm}(\mathbf{k})\, u_{m0}(\mathbf{r}) \tag{C.4}$$

  where the functions $u_{n0}(\mathbf{r}) \equiv \psi_{n0}(\mathbf{r})$ are the Bloch waves at the Γ point. $u_{10}(\mathbf{r})$ is a s-wave labeled $|S\rangle$, $u_{20}(\mathbf{r})$ is a p_x-wave labeled $|X\rangle$, $u_{30}(\mathbf{r})$ is a p_y-wave labeled $|Y\rangle$, and $u_{40}(\mathbf{r})$ is a p_z-wave labeled $|Z\rangle$.

- The band structure is isotropic in the vicinity of the Γ point. Thus we solve Eq. (C.3) with the wave vector $\mathbf{k}$ along one particular axis, e.g., in the x direction.

With these simplifications, the energies $E_n(k_x)$ solutions of Eq. (C.3) are given by diagonalizing the following matrix

$$\begin{bmatrix} E_C + \frac{\hbar^2 k_x^2}{2m_0} & -i\hbar P k_x & 0 & 0 \\ i\hbar P k_x & E_V + \frac{\hbar^2 k_x^2}{2m_0} & 0 & 0 \\ 0 & 0 & E_V + \frac{\hbar^2 k_x^2}{2m_0} & 0 \\ 0 & 0 & 0 & E_V + \frac{\hbar^2 k_x^2}{2m_0} \end{bmatrix} \tag{C.5}$$

where $E_C \equiv E_1(0)$ is the conduction-band minimum, $E_V \equiv E_2(0) = E_3(0) = E_4(0)$ is the valence-band maximum, and $P \equiv \frac{-i}{m_0}\langle S|p_x|X\rangle$ is the interband matrix element of the momentum operator (all other matrix elements of the momentum operator vanish by symmetry). In practice, one has to diagonalize a 2×2 matrix. Thus this method is known as the two-band Kane model.

The eigenvalues of the matrix (C.5) are

$$E_1(k_x) = \frac{\hbar^2 k_x^2}{2m_0} + \frac{E_C + E_V}{2} + \frac{1}{2}\sqrt{E_G^2 + \hbar^2 P^2 k_x^2} \tag{C.6}$$

$$E_2(k_x) = \frac{\hbar^2 k_x^2}{2m_0} + \frac{E_C + E_V}{2} - \frac{1}{2}\sqrt{E_G^2 + \hbar^2 P^2 k_x^2} \tag{C.7}$$

$$E_3(k_x) = E_4(k_x) = E_V + \frac{\hbar^2 k_x^2}{2m_0} \tag{C.8}$$

where $E_G = E_C - E_V$ is the fundamental band gap.

The second-order Taylor series expansion of $E_1(k_x)$ leads to the parabolic approximation for the conduction-band dispersion relation:

$$E_1(k_x) \simeq E_C + \frac{\hbar^2 k_x^2}{2m_C} \tag{C.9}$$

where the effective mass m_C is given by

$$\frac{1}{m_C} = \frac{1}{m_0} + \frac{2P^2}{E_G}. \tag{C.10}$$

The fourth-order Taylor series expansion of $E_1(k_x)$ leads to the simplest nonparabolic approximation for the conduction-band dispersion relation:

$$E_1(k_x) \simeq E_C + \frac{\hbar^2 k_x^2}{2m_C} - \frac{\hbar^4 P^4 k_x^4}{E_G^3} \tag{C.11}$$

which is formally equivalent to

$$\frac{\hbar^2 k_x^2}{2m_C} \simeq (E_1 - E_C)\left[1 + \lambda(E_1 - E_C)\right]. \tag{C.12}$$

It is easy to show that $\lambda = 1/E_G$, i.e.,

$$\frac{\hbar^2 k_x^2}{2m_C} \simeq (E_1 - E_C)\left(1 + \frac{E_1 - E_C}{E_G}\right). \tag{C.13}$$

With such conduction-band dispersion relation, the effective momentum mass $[\frac{1}{m_C(E_1)} = \frac{1}{\hbar^2 k_x}\frac{dE_1}{dk_x}]$ is

$$m_C(E_1) = m_C\left(1 + 2\frac{E_1 - E_C}{E_G}\right), \tag{C.14}$$

and the density of states is

$$N_C(E_1) = \frac{m_C}{\pi^2\hbar^3}\sqrt{2m_C(E_1 - E_C)\left(1 + \frac{E_1 - E_C}{E_G}\right)}\left[1 + \frac{2(E_1 - E_C)}{E_G}\right]. \tag{C.15}$$

D Stationary states of an asymmetric quantum well

In this section, we consider the single-electron time-independent Schrödinger equation in a one-dimensional quantum well (QW)

$$\left[\frac{p_z^2}{2m\left(z\right)}+V\left(z\right)\right]\psi\left(z\right)=E\psi\left(z\right) \tag{D.1}$$

where $p_z=\frac{\hbar}{i}\frac{d}{dz}$ is the momentum operator, $m\left(z\right)$ is a position-dependent effective mass, and $V\left(z\right)$ is the confinement potential. The effective mass and the potential are given by

$$\begin{cases} m\left(z\right)=m_L \text{ and } V\left(z\right)=V_L \text{ in the left barrier } \left(-\infty<z<0\right) \\ m\left(z\right)=m_{QW} \text{ and } V\left(z\right)=0 \text{ in the QW } \left(0<z<l\right) \\ m\left(z\right)=m_R \text{ and } V\left(z\right)=V_R \text{ in the right barrier } \left(l<z<+\infty\right) \end{cases} \tag{D.2}$$

where l is the QW width.

Solving equation (D.1) separately in the three regions, one obtain the following wave functions and energies

$$\begin{cases} \psi\left(z\right)=A\exp\left(\kappa_L z\right)+B\exp\left(-\kappa_L z\right) \text{ and } V_L-E=\frac{\hbar^2\kappa_L^2}{2m_L} \text{ for } -\infty<z<0 \\ \psi\left(z\right)=C\exp\left(ikz\right)+D\exp\left(-ikz\right) \text{ and } E=\frac{\hbar^2k^2}{2m_{QW}} \text{ for } 0<z<l \\ \psi\left(z\right)=F\exp\left(\kappa_R z\right)+G\exp\left(-\kappa_R z\right) \text{ and } V_R-E=\frac{\hbar^2\kappa_R^2}{2m_R} \text{ for } l<z<+\infty \end{cases} \tag{D.3}$$

for the bound states $\left(0<E<V_L,V_R\right)$. The coefficients B and F must vanish, to avoid divergence of the wave function for $z\rightarrow-\infty$ and $z\rightarrow+\infty$, respectively. The boundary conditions [continuity of $\psi\left(z\right)$ and of $\frac{1}{m(z)}\frac{d\psi}{dz}$] then lead to the system

$$\begin{cases} A=C+D \\ \frac{1}{m_L}\kappa_L A=\frac{1}{m_{QW}}ikC-\frac{1}{m_{QW}}ikD \\ C\exp\left(ikl\right)+D\exp\left(-ikl\right)=G\exp\left(-\kappa_R l\right) \\ \frac{1}{m_{QW}}ikC\exp\left(ikl\right)-\frac{1}{m_{QW}}ikD\exp\left(-ikl\right)=-\frac{1}{m_R}\kappa_R G\exp\left(-\kappa_R l\right) \end{cases} \tag{D.4}$$

which has solutions only if

$$\begin{vmatrix} 1 & -1 & -1 & 0 \\ \frac{\kappa_L}{m_L} & \frac{-ik}{m_{QW}} & \frac{ik}{m_{QW}} & 0 \\ 0 & \exp(ikl) & \exp(-ikl) & -\exp(-\kappa_R l) \\ 0 & \frac{ik\exp(ikl)}{m_{QW}} & \frac{-ik\exp(-ikl)}{m_{QW}} & \frac{\kappa_R\exp(-\kappa_R l)}{m_R} \end{vmatrix} = 0. \tag{D.5}$$

Developing the determinant in equation (D.5) gives

$$\frac{k}{m_{QW}}\left(\frac{\kappa_L}{m_L}+\frac{\kappa_R}{m_R}\right)\cos(kl)+\left(\frac{\kappa_L\kappa_R}{m_L m_R}-\frac{k^2}{m_{QW}^2}\right)\sin(kl)=0. \tag{D.6}$$

Equation (D.6), with the dispersion relations given in (D.3), allows to determine numerically the discrete energy levels E_n of the bound states.

It is possible to take into account nonparabolicity effects for the dispersion relation in the QW. Specifically, one has to solve equation (D.6) and the equation giving the energy-dependent effective mass [equation (C.14) in the case of the two-band Kane model] in a self-consistent manner.

E Method of images in electrostatics

In this section, we present the method of images in electrostatics [174]. This method can be used to solve problems involving one (or more) point charges in the presence of interfaces on which either the electrostatic potential or the surface density of external charge is known. The method consists of considering a small number of so-called image charges, put outside of the region of interest in order to simulate the required boundary conditions. Here, we apply the method of images in two important cases, namely a dielectric-metal interface and a dielectric-dielectric interface.

E.1 Dielectric-metal interface

Let us first consider the case of a point charge q embedded in a semi-infinite dielectric of constant ϵ, at a distance d from a plane interface which separates the dielectric from a metal. The situation is depicted in figure E.1(a). In cylindrical coordinates, q is located at a point $(r = 0, \varphi = 0, z = d)$. The electrostatic potential Φ at the interface is assumed to be zero, hence the boundary condition at $z = 0$:

$$\Phi(r, \varphi, z = 0) = 0. \tag{E.1}$$

For calculating Φ for $z > 0$, an image charge q' is put at the position $(r = 0, \varphi = 0, z = -d)$:

$$\Phi(r, \varphi, z > 0) = \frac{1}{4\pi\epsilon}\left(\frac{q}{R_1} + \frac{q'}{R_2}\right) \tag{E.2}$$

where $R_1 = \sqrt{r^2 + (d - z)^2}$ and $R_2 = \sqrt{r^2 + (d + z)^2}$. Together, equations (E.1) and (E.2) lead to the image charge q':

$$q' = -q. \tag{E.3}$$

E.2 Dielectric-dielectric interface

Let us then consider the case of a point charge q embedded in a semi-infinite dielectric D_1 of constant ϵ_1, at a distance d from a plane interface which separates the dielectric D_1 from another dielectric

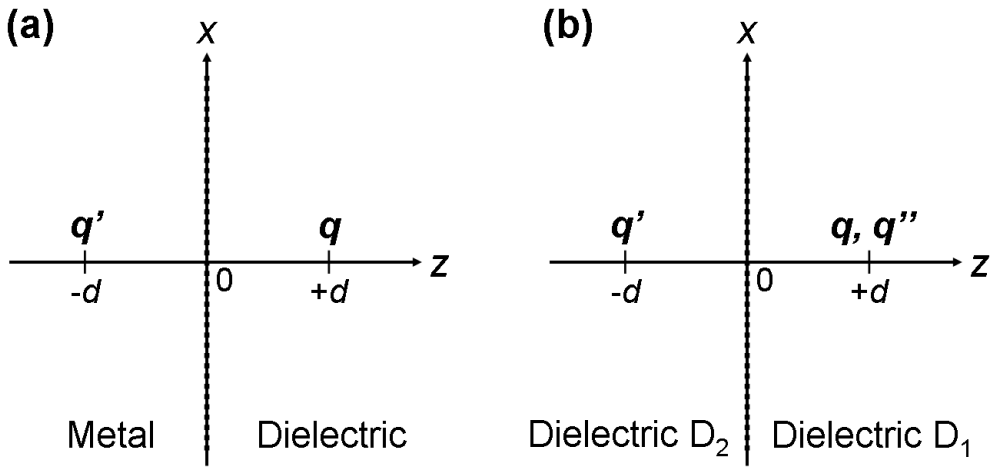

Figure E.1: Method of images in electrostatics. **(a)** Point charge q embedded in a semi-infinite dielectric, at a distance d from a plane interface which separates the dielectric from a metal. In cylindrical coordinates, q is located at a point $(r = 0, \varphi = 0, z = d)$. An image charge q' is put at the position $(r = 0, \varphi = 0, z = -d)$. **(b)** Point charge q embedded in semi-infinite dielectric D_1, at a distance d from a plane interface which separates the dielectric D_1 from another dielectric D_2. In cylindrical coordinates, q is located at a point $(r = 0, \varphi = 0, z = d)$. An image charge q' is put at the position $(r = 0, \varphi = 0, z = -d)$, and an image charge q'' is put at the position of the actual charge q.

D_2 of constant ϵ_2. The situation is depicted in figure E.1(b). In cylindrical coordinates, q is located at a point $(r = 0, \varphi = 0, z = d)$. The surface density of external charge at the interface is assumed to be zero, hence the boundary condition at $z = 0$:

$$\begin{cases} \epsilon_1 \frac{\partial \Phi}{\partial z}(z \to 0^+) = \epsilon_2 \frac{\partial \Phi}{\partial z}(z \to 0^-) \\ \frac{\partial \Phi}{\partial x}(z \to 0^+) = \frac{\partial \Phi}{\partial x}(z \to 0^-) \\ \frac{\partial \Phi}{\partial y}(z \to 0^+) = \frac{\partial \Phi}{\partial y}(z \to 0^-) \end{cases} \tag{E.4}$$

On one hand, for calculating Φ for $z > 0$, an image charge q' is put at the position $(r = 0, \varphi = 0, z = -d)$:

$$\Phi(r, \varphi, z > 0) = \frac{1}{4\pi\epsilon_1} \left(\frac{q}{R_1} + \frac{q'}{R_2} \right). \tag{E.5}$$

On the other hand, for calculating Φ for $z < 0$, an image charge q'' is put at the position $(r = 0, \varphi = 0, z = d)$ of the actual charge q:

$$\Phi(r, \varphi, z < 0) = \frac{1}{4\pi\epsilon_2} \frac{q''}{R_1}. \tag{E.6}$$

Together, equations (E.4), (E.5) and (E.6) lead to the image charges q' and q'':

$$\begin{cases} q' = \frac{\epsilon_1 - \epsilon_2}{\epsilon_1 + \epsilon_2} q \\ q'' = \frac{2\epsilon_2}{\epsilon_1 + \epsilon_2} q \end{cases} \tag{E.7}$$

If the point charge q is located at the interface between the two dielectrics, i.e., if $d = 0$, then

$$\Phi(r, \varphi, z) = \frac{2q}{4\pi(\epsilon_1 + \epsilon_2)R} \tag{E.8}$$

where $R = R_1 = R_2 = \sqrt{r^2 + z^2}$. In other words, the effective dielectric constant for a point charge located at the interface between the two dielectrics D_1 and D_2 is given by

$$\epsilon_{eff} = \frac{\epsilon_1 + \epsilon_2}{2}. \tag{E.9}$$

References

[1] T. Ando, A. B. Fowler, and F. Stern, Electronic properties of two-dimensional systems, *Rev. Mod. Phys.* **54**, 437 (1982).

[2] S. M. Sze, *Semiconductor devices*, 2nd edition (Wiley, New York, 2002).

[3] P. A. Lee and T. V. Ramakrishnan, Disordered electronic systems, *Rev. Mod. Phys.* **57**, 287 (1985).

[4] K. von Klitzing, The quantized Hall effect, *Rev. Mod. Phys.* **58**, 519 (1986).

[5] H. L. Stormer, The fractional quantum Hall effect, *Rev. Mod. Phys.* **71**, 875 (1999).

[6] M. J. Kelly and R. J. Nicholas, The physics of quantum well structures, *Rep. Prog. Phys.* **48**, 1699 (1985).

[7] G. Bastard, *Wave mechanics applied to semiconductor heterostructures* (Les Editions de Physique, Les Ulis, 1988).

[8] Z. I. Alferov, The double heterostructure concept and its applications in physics, electronics, and technology, *Rev. Mod. Phys.* **73**, 767 (2001).

[9] H. Kroemer, Quasielectric fields and band offsets: teaching electrons new tricks, *Rev. Mod. Phys.* **73**, 783 (2001).

[10] *The technology and physics of molecular beam epitaxy*, edited by E. H. C. Parker (Plenum Press, New York, 1985).

[11] B. A. Joyce, Molecular beam epitaxy, *Rep. Prog. Phys.* **48**, 1637 (1985).

[12] J. R. Arthur, Molecular beam epitaxy, *Surf. Sci.* **500**, 189 (2002).

[13] W. P. McCray, MBE deserves a place in the history books, *Nature Nanotech.* **2**, 259 (2007).

[14] F. Capasso, Band-gap engineering: From physics and materials to new semiconductor devices, *Science* **235**, 172 (1987).

[15] J. H. English, A. C. Gossard, H. L. Störmer, and K. W. Baldwin, GaAs structures with electron mobility of 5×10^6 cm^2/Vs, *Appl. Phys. Lett.* **50**, 1826 (1987).

[16] L. Pfeiffer and K. W. West, The role of MBE in recent quantum Hall effect physics discoveries, *Physica E* **20**, 57 (2003).

[17] R. Dingle, H. L. Stormer, A. C. Gossard, and W. Wiegmann, Electron mobilities in modulation-doped semiconductor heterojunction superlattices, *Appl. Phys. Lett.* **33**, 665 (1978).

[18] B. E. Kane, L. N. Pfeiffer, and K. W. West, Variable density high-mobility two-dimensional electron and hole gases in a gated GaAs/Al_xGa_{1-x}As heterostructure, *Appl. Phys. Lett.* **63**, 2132 (1993).

[19] J. Herfort and Y. Hirayama, Transport in gated undoped GaAs/Al_xGa_{1-x}As heterostructures in the high density and high mobility range, *Appl. Phys. Lett.* **69**, 3360 (1996).

[20] Y. Hirayama, Formation of two-dimensional electron and hole gases in undoped Al_xGa_{1-x}As/GaAs heterostructures, *J. Appl. Phys.* **80**, 588 (1996).

[21] U. Meirav, M. Heiblum, and F. Stern, High-mobility variable-density two-dimensional electron gas in inverted GaAs-AlGaAs heterojunctions, *Appl. Phys. Lett.* **52**, 1268 (1988).

[22] T. Sajoto, M. Santos, J. J. Heremans, M. Shayegan, M. Heiblum, M. V. Weckwerth, and U. Meirav, Use of superlattices to realize inverted GaAs/AlGaAs heterojunctions with low-temperature mobility of 2×10^6 cm^2/Vs, *Appl. Phys. Lett.* **54**, 840 (1989).

[23] Y. Hirayama, K. Muraki, and T. Saku, Two-dimensional electron gas formed in a back-gated undoped heterostructure, *Appl. Phys. Lett.* **72**, 1745 (1998).

[24] T. Mimura, S. Hiyamizu, T. Fuji, and K. Nanbu, A new field-effect transistor with selectively doped GaAs/n-Al_xGa_{1-x}As heterojunctions, *Jpn. J. Appl. Phys.* **19**, L225 (1980).

[25] D. Delagebeaudeuf, P. Delescluse, P. Etienne, M. Laviron, J. Chaplart, and N. T. Linh, Two-dimensional electron gas MESFET structure, *Electron. Lett.* **16**, 667 (1980).

[26] G. Binnig and H. Rohrer, Scanning tunneling microscopy - from birth to adolescence, *Rev. Mod. Phys.* **59**, 615 (1987).

[27] L. E. C. van de Leemput and H. van Kempen, Scanning tunnelling microscopy, *Rep. Prog. Phys.* **55**, 1165 (1992).

[28] C. Julian Chen, *Introduction to scanning tunneling microscopy* (Oxford University Press, Oxford, 1993).

[29] R. Wiesendanger, *Scanning probe microscopy and spectroscopy* (Cambridge University Press, Cambridge, 1994).

[30] G. Binnig and H. Rohrer, Scanning tunneling microscopy, *IBM J. Res. Develop.* **44**, 279 (2000).

[31] G. Eytan, Y. Yayon, M. Rappaport, H. Shtrikman, and I. Bar-Joseph, Near-field spectroscopy of a gated electron gas: a direct evidence for electron localization, *Phys. Rev. Lett.* **81**, 1666 (1998).

[32] Y. Yayon, A. Esser, M. Rappaport, V. Umansky, H. Shtrikman, and I. Bar-Joseph, Long-range spatial correlations in the exciton energy distribution in GaAs/AlGaAs quantum wells, *Phys. Rev. Lett.* **89**, 157402 (2002).

[33] M. A. Eriksson, R. G. Beck, M. Topinka, J. A. Katine, R. M. Westervelt, K. L. Campman, and A. C. Gossard, Cryogenic scanning probe characterization of semiconductor nanostructures, *Appl. Phys. Lett.* **69**, 671 (1996).

[34] R. Crook, C. G. Smith, M. Y. Simmons, and D. A. Ritchie, Imaging cyclotron orbits and scattering sites in a high-mobility two-dimensional electron gas, *Phys. Rev. B* **62**, 5174 (2000).

[35] M. A. Topinka, B. J. LeRoy, S. E. J. Shaw, E. J. Heller, R. M. Westervelt, K. D. Maranowski, and A. C. Gossard, Imaging coherent electron flow from a quantum point contact, *Science* **289**, 2323 (2000).

[36] M. A. Topinka, B. J. LeRoy, R. M. Westervelt, S. E. J. Shaw, R. Fleischmann, E. J. Heller, K. D. Maranowski, and A. C. Gossard, Coherent branched flow in a two-dimensional electron gas, *Nature* **410**, 183 (2001).

[37] M. T. Woodside, C. Vale, P. L. McEuen, C. Kadow, K. D. Maranowski, and A. C. Gossard, Imaging interedge-state scattering centers in the quantum Hall regime, *Phys. Rev. B* **64**, 041310 (2001).

[38] B. J. LeRoy, M. A. Topinka, R. M. Westervelt, K. D. Maranowski, and A. C. Gossard, Imaging electron density in a two-dimensional electron gas, *Appl. Phys. Lett.* **80**, 4431 (2002).

[39] R. Crook, C. G. Smith, W. R. Tribe, S. J. O'Shea, M. Y. Simmons, and D. A. Ritchie, Quantum-dot electron occupancy controlled by a charged scanning probe, *Phys. Rev. B* **66**, 121301 (2002).

[40] R. Crook, A. C. Graham, C. G. Smith, I. Farrer, H. E. Beere, and D. A. Ritchie, Erasable electrostatic lithography for quantum components, *Nature* **424**, 751 (2003).

[41] R. Crook, C. G. Smith, A. C. Graham, I. Farrer, H. E. Beere, and D. A. Ritchie, Imaging fractal conductance fluctuations and scarred wave functions in a quantum billiard, *Phys. Rev. Lett.* **91**, 246803 (2003).

[42] S. Kičin, A. Pioda, T. Ihn, K. Ensslin, D. C. Driscoll, and A. C. Gossard, Local backscattering in the quantum Hall regime, *Phys. Rev. B* **70**, 205302 (2004).

[43] A. Pioda, S. Kičin, T. Ihn, M. Sigrist, A. Fuhrer, K. Ensslin, A. Weichselbaum, S. E. Ulloa, M. Reinwald, and W. Wegscheider, Spatially resolved manipulation of single electrons in quantum dots using a scanning probe, *Phys. Rev. Lett.* **93**, 216801 (2004).

[44] P. Fallahi, A. C. Bleszynski, R. M. Westervelt, J. Huang, J. D. Walls, E. J. Heller, M. Hanson, and A. C. Gossard, Imaging a single-electron quantum dot, *Nano Lett.* **5**, 223 (2005).

[45] B. J. LeRoy, A. C. Bleszynski, K. E. Aidala, R. M. Westervelt, A. Kalben, E. J. Heller, S. E. J. Shaw, K. D. Maranowski, and A. C. Gossard, Imaging electron interferometer, *Phys. Rev. Lett.* **94**, 126801 (2005).

[46] R. Crook, J. Prance, K. J. Thomas, S. J. Chorley, I. Farrer, D. A. Ritchie, M. Pepper, and C. G. Smith, Conductance quantization at a half-integer plateau in a symmetric GaAs quantum wire, *Science* **312**, 1359 (2006).

[47] S. H. Tessmer, P. I. Glicofridis, R. C. Ashoori, L. S. Levitov, and M. R. Melloch, Subsurface charge accumulation imaging of a quantum Hall liquid, *Nature* **392**, 51 (1998).

[48] G. Finkelstein, P. I. Glicofridis, S. H. Tessmer, R. C. Ashoori, and M. R. Melloch, Imaging of low-compressibility strips in the quantum Hall regime, *Phys. Rev. B* **61**, 16323 (2000).

[49] G. Finkelstein, P. I. Glicofridis, R. C. Ashoori, and M. Shayegan, Topographic mapping of the quantum Hall liquid using a few-electron bubble, *Science* **289**, 90 (2000).

[50] P. I. Glicofridis, G. Finkelstein, R. C. Ashoori, and M. Shayegan, Determination of the resistance across incompressible strips through imaging of charge motion, *Phys. Rev. B* **65**, 121312 (2002).

[51] G. A. Steele, R. C. Ashoori, L. N. Pfeiffer, and K. W. West, Imaging transport resonances in the quantum Hall effect, *Phys. Rev. Lett.* **95**, 136804 (2005).

[52] N. B. Zhitenev, T. A. Fulton, A. Yacoby, H. S. Hess, L. N. Pfeiffer, and K. W. West, Imaging of localized electronic states in the quantum Hall regime, *Nature* **404**, 473 (2000).

[53] S. Ilani, J. Martin, E. Teitelbaum, J. H. Smet, D. Mahalu, V. Umansky, and A. Yacoby, The microscopic nature of localization in the quantum Hall effect, *Nature* **427**, 328 (2004).

[54] J. Martin, S. Ilani, B. Verdene, J. Smet, V. Umansky, D. Mahalu, D. Schuh, G. Abstreiter, and A. Yacoby, Localization of fractionally charged quasi-particles, *Science* **305**, 980 (2004).

[55] M. F. Crommie, C. P. Lutz, and D. M. Eigler, Imaging standing waves in a two-dimensional electron gas, *Nature* **363**, 524 (1993).

[56] Y. Hasegawa and P. Avouris, Direct observation of standing wave formation at surface steps using scanning tunneling microscopy, *Phys. Rev. Lett.* **71**, 1071 (1993).

[57] D. Fujita, K. Amemiya, T. Yakabe, H. Nejoh, T. Sato, and M. Iwatsuki, Anisotropic standing-wave formation on an Au(111)-($23\times\sqrt{3}$) reconstructed surface, *Phys. Rev. Lett.* **78**, 3904 (1997).

[58] P. T. Sprunger, L. Petersen, E. W. Plummer, E. Lægsgaard, and F. Besenbacher, Giant Friedel oscillations on the beryllium(0001) surface, *Science* **275**, 1764 (1997).

[59] Ph. Hofmann, B. G. Briner, M. Doering, H.-P. Rust, E. W. Plummer, and A. M. Bradshaw, Anisotropic two-dimensional Friedel oscillations, *Phys. Rev. Lett.* **79**, 265 (1997).

[60] B. G. Briner, Ph. Hofmann, M. Doering, H.-P. Rust, E. W. Plummer, and A. M. Bradshaw, Charge-density oscillations on Be($10\bar{1}0$): Screening in a non-free two-dimensional electron gas, *Phys. Rev. Lett.* **58**, 13931 (1998).

[61] V. Madhavan, W. Chen, T. Jamneala, M. F. Crommie, and N. S. Wingreen, Local spectroscopy of a Kondo impurity: Co on Au(111), *Phys. Rev. B* **64**, 165412 (2001).

[62] M. Ternes, C. Weber, M. Pivetta, F. Patthey, J. P. Pelz, T. Giamarchi, F. Mila, and W.-D. Schneider, Scanning-tunneling spectroscopy of surface-state electrons scattered by a slightly disordered two-dimensional dilute solid: Ce on Ag(111), *Phys. Rev. Lett.* **93**, 146805 (2004).

[63] J. I. Pascual, G. Bilhmayer, Yu. M. Koroteev, H.-P. Rust, G. Ceballos, M. Hansmann, K. Horn, E. V. Chulkov, S. Blügel, P. M. Echenique, and Ph. Hofmann, Role of spin in quasiparticle interference, *Phys. Rev. Lett.* **93**, 196802 (2004).

[64] J. Repp, G. Meyer, and K.-H. Rieder, Snell's law for surface electrons: Refraction of an electron gas imaged in real space, *Phys. Rev. Lett.* **92**, 036803 (2004).

[65] F. E. Olsson, M. Persson, A. G. Borisov and J.P. Gauyack, J. Lagoute, and S. Fölsch, Localization of the Cu(111) surface state by single Cu adatoms, *Phys. Rev. Lett.* **93**, 206803 (2004).

[66] L. Limot, E. Pehlke, J. Kröger, and R. Berndt, Surface-state localization at adatoms, *Phys. Rev. Lett.* **94**, 036805 (2005).

[67] M. Ono, Y. Nishigata, T. Nishio, T. Eguchi, and Y. Hasegawa, Electrostatic potential screened by a two-dimensional electron system: a real-space observation by scanning tunneling spectroscopy, *Phys. Rev. Lett.* **96**, 016801 (2006).

[68] C.-S. Jiang, H.-B. Yu, X.-D. Wang, C.-K. Shih, and Ph. Ebert, Scanning tunneling spectroscopy of quantum well and surface states of thin Ag films grown on GaAs(110), *Phys. Rev. B* **64**, 235410 (2001).

[69] J. Kliewer and R. Berndt, Scanning tunneling spectroscopy of Na on Cu(111), *Phys. Rev. B* **65**, 035412 (2001).

[70] I. Brihuega, P. Mallet, L. Magaud, S. Pons, O. Custance, J. M. Gomez-Rodriguez, and J. Y. Veuillen, Quantum interference patterns and electron confinement on a two-dimensional metal: a scanning tunneling microscopy study, *Phys. Rev. B* **69**, 155407 (2004).

[71] F. Vonau, D. Aubel, G. Gewinner, C. Pirri, J. C. Peruchetti, D. Bolmont, and L. Simon, Fermi contour imaging of the two-dimensional semimetal $ErSi_2$ by Fourier transform STM, *Phys. Rev. B* **69**, 081305(R) (2004).

[72] F. Vonau, D. Aubel, G. Gewinner, S. Zabrocki, J. C. Peruchetti, D. Bolmont, and L. Simon, Evidence of hole-electron quasiparticle interference in $ErSi_2$ semimetal by Fourier-transform scanning tunneling spectroscopy, *Phys. Rev. Lett.* **95**, 176803 (2005).

[73] E. Dupont-Ferrier, P. Mallet, L. Magaud, and J. Y. Veuillen, Bound states at impurities in a two-dimensional metal, *Europhys. Lett.* **72**, 430 (2005).

[74] H. A. Mizes and J. S. Foster, Long-range electronic perturbations caused by defects using scanning tunneling microscopy, *Science* **244**, 559 (1989).

[75] P. Ruffieux, M. Melle-Franco, O. Gröning, M. Bielmann, F. Zerbetto, and P. Gröning, Charge-density oscillation on graphite induced by the interference of electron waves, *Phys. Rev. B* **71**, 153403 (2005).

[76] T. Matsui, H. Kambara, Y. Niimi, K. Tagami, M. Tsukada, and H. Fukuyama, STS observations of Landau levels at graphite surfaces, *Phys. Rev. Lett.* **94**, 226403 (2005).

[77] Y. Niimi, H. Kambara, T. Matsui, D. Yoshioka, and H. Fukuyama, Real-space imaging of alternate localization and extension of quasi-two-dimensional electronic states at graphite surfaces in magnetic fields, *Phys. Rev. Lett.* **97**, 236804 (2006).

[78] K. Kanisawa, M. J. Butcher, H. Yamaguchi, and Y. Hirayama, Imaging of Friedel oscillation patterns of two-dimensionally accumulated electrons at epitaxially grown InAs(111)A surface, *Phys. Rev. Lett.* **86**, 3384 (2001).

[79] M. Morgenstern, J. Klijn, Chr. Meyer, M. Getzlaff, R. Adelung, R. A. Römer, K. Rossnagel, L. Kipp, M. Skibowski, and R. Wiesendanger, Direct comparison between potential landscape and local density of states in a disordered two-dimensional electron system, *Phys. Rev. Lett.* **89**, 136806 (2002).

[80] M. Morgenstern, J. Klijn, Chr. Meyer, and R. Wiesendanger, Real-space observation of drift states in a two-dimensional electron system at high magnetic fields, *Phys. Rev. Lett.* **90**, 056804 (2003).

[81] J. Wiebe, Chr. Meyer, J. Klijn, M. Morgenstern, and R. Wiesendanger, From quantized states to percolation: Scanning tunneling spectroscopy of a strongly disordered two-dimensional electron system, *Phys. Rev. B* **68**, 041402 (2003).

[82] K. Suzuki, K. Kanisawa, C. Janer, S. Perraud, K. Takashina, T. Fujisawa, and Y. Hirayama, Spatial imaging of two-dimensional electronic states in semiconductor quantum wells, *Phys. Rev. Lett.* **98**, 136802 (2007).

[83] C. E. C. Wood, in *GaInAsP alloy semiconductors*, edited by T. P. Pearsall (Wiley, New York, 1982).

[84] R. F. C. Farrow, Stabilization of surfaces of III-V compound crystals by molecular beams, *J. Phys. D* **8**, L87 (1975).

[85] G. J. Davies, R. Heckingbottom, H. Ohno, C. E. C. Wood, and A. R. Calawa, Arsenic stabilization of InP substrates for growth of $Ga_xIn_{1-x}As$ layers by molecular beam epitaxy, *Appl. Phys. Lett.* **37**, 290 (1980).

[86] J. M. Moison, M. Bensoussan, and F. Houzay, Epitaxial regrowth of an InAs surface on InP: an example of artificial surfaces, *Phys. Rev. B* **34**, 2018 (1986).

[87] G. Hollinger, D. Gallet, M. Gendry, C. Santinelli, and P. Victorovitch, Structural and chemical properties of InAs layers grown on InP(001) surfaces by arsenic stabilization, *J. Vac. Sci. Technol. B* **8**, 832 (1990).

[88] R. Averbeck, H. Riechert, H. Schlötterer, and G. Weimann, Oxide desorption from InP under stabilizing pressures of P_2 or As_4, *Appl. Phys. Lett.* **59**, 1732 (1991).

[89] S. Hofmann, Sputter depth profile analysis of interfaces, *Rep. Prog. Phys.* **61**, 827 (1998).

[90] T. Becker, H. Hövel, M. Tschudy, and B. Reihl, Applications with a new low-temperature UHV STM at 5 K, *Appl. Phys. A* **66**, S27 (1998).

[91] F. G. Allen and G. W. Gobeli, Work function, photoelectric threshold, and surface states of atomically clean silicon, *Phys. Rev.* **127**, 150 (1962).

[92] H. Lüth, *Solid surfaces, interfaces and thin films*, 4th edition (Springer, Berlin, 2001).

[93] W. Mönch, P. Koke, and S. Krueger, On the electronic structure of clean, 2×1 reconstructed silicon (001) surfaces, *J. Vac. Sci. Technol.* **19**, 313 (1981).

[94] M. D. Pashley and K. W. Haberern, Compensating surface defects induced by Si doping of GaAs, *Phys. Rev. Lett.* **67**, 2697 (1991).

[95] M. D. Pashley, K. W. Haberern, R. M. Feenstra, and P. D. Kirchner, Different Fermi-level pinning behavior on *n*- and *p*-type GaAs(001), *Phys. Rev. B* **48**, 4612 (1993).

[96] S. Kasai, N. Negoro, and H. Hasegawa, Conductance gap anomaly in scanning tunneling spectra of MBE-Grown (001) surfaces of III-V compound semiconductors, *Appl. Surf. Sci.* **175-176**, 255 (2001).

[97] M. Noguchi, K. Hirakawa, and T. Ikoma, Intrinsic electron accumulation layers on reconstructed clean InAs(100) surfaces, *Phys. Rev. Lett.* **66**, 2243 (1991).

[98] L. Ö. Olsson, C. B. M. Andersson, M. C. Håkansson, J. Kanski, L. Ilver, and U. O. Karlsson, Charge accumulation at InAs surfaces, *Phys. Rev. Lett.* **76**, 3626 (1996).

[99] *Properties of Lattice-Matched and Strained Indium Gallium Arsenide*, edited by P. Bhattacharya, INSPEC-EMIS Datareview Series No. 8 (London, 1993).

[100] D. Hull and D. J. Bacon, *Introduction to dislocations*, fourth ed. (Butterworth-Heinemann, Oxford, 2001).

[101] K. Kanisawa, M. J. Butcher, Y. Tokura, H. Yamaguchi, and Y. Hirayama, Local density of states in zero-dimensional semiconductor structures, *Phys. Rev. Lett.* **87**, 196804 (2001).

[102] T. Fujii, T. Inata, K. Ishii, and S. Hiyamizu, Heavily Si-doped InGaAs lattice-matched to InP grown by MBE, *Electron. Lett.* **22**, 191 (1986).

[103] D. J. Chadi, Atomic structure of GaAs(100)-(2×1) and (2×4) reconstructed surfaces, *J. Vac. Sci. Technol. A* **5**, 834 (1987).

[104] M. D. Pashley, K. W. Haberern, W. Friday, J. M. Woodall, and P. D. Kirchner, Structure of the GaAs(001) (2×4)-c(2×8) determined by scanning tunneling microscopy, *Phys. Rev. Lett.* **60**, 2176 (1988).

[105] J. M. Moison, C. Guille, F. Houzay, F. Barthe, and M. Van Rompay, Surface segregation of third-column atoms in group III-V arsenide compounds: ternary alloys and heterostructures, *Phys. Rev. B* **40**, 6149 (1989).

[106] K. Kanisawa, H. Yamaguchi, and Y. Horikoshi, Electronic properties of monolayer steps on (2×4)/c(2×8) reconstructed GaAs(001) surfaces, *Phys. Rev. B* **54**, 4428 (1996).

[107] S. Y. Tong, G. Xu, and W. N. Mei, Vacancy-buckling model for the (2×2) GaAs(111) surface, *Phys. Rev. Lett.* **52**, 1693 (1984).

[108] K. W. Haberern and M. D. Pashley, GaAs(111)A-(2×2) reconstruction studied by scanning tunneling microscopy, *Phys. Rev. B* **41**, 3226 (1990).

[109] J. F. Zheng, D. F. Ogletree, J. Walker, M. Salmeron, and E. R. Weber, Cross-sectional scanning tunneling microscopy of semiconductor vertical-cavity surface-emitting laser structure, *J. Vac. Sci. Technol. B* **12**, 2100 (1994).

[110] H. A. McKay, H. Chen, R. M. Feenstra, and P. J. Poole, Scanning tunneling microscopy images of III-V semiconductor alloys: strain effects, *J. Vac. Sci. Technol. B* **21**, 18 (2003).

[111] G. B. Stringfellow, Miscibility gaps in quaternary III/V alloys, *J. Cryst. Growth* **58**, 194 (1982).

[112] K. Onabe, Unstable regions in III-V quaternary solid solutions composition plane calculated with strictly regular solution approximation, *Jpn. J. Appl. Phys.* **21**, L323 (1982).

[113] T. L. McDevitt, S. Mhajan, D. E. Laughlin, W. A. Bonner, and V. G. Keramidas, Two-dimensional phase separation in $In_{1-x}Ga_xAs_yP_{1-y}$ epitaxial layers, *Phys. Rev. B* **45**, 6614 (1992).

[114] A. Taguchi, Stable adsorption sites and potential-energy surface of a Ga adatom on a GaAs(111)*A* surface, *Phys. Rev. B* **60**, 11509 (1999).

[115] A. Taguchi and K. Kanisawa, Stable reconstruction and adsorbates of InAs(111)A surface, *Appl. Surf. Sci.* **252**, 5263 (2006).

[116] K. Kanisawa *et al.*, unpublished.

[117] W. Lee and C. G. Fonstad, The growth of high mobility InGaAs and InAlAs layers by molecular beam epitaxy, *J. Vac. Sci. Technol. B* **4**, 536 (1986).

[118] P. W. Anderson, Absence of diffusion in certain random lattices, *Phys. Rev.* **109**, 1492 (1958).

[119] P. E. Lindelof, J. Nørregard, and J. Hanberg, *Phys. Scr. T* **14**, 317 (1986).

[120] D. S. Wiersma, P. Bartolini, A. Lagendijk, and R. Righini, Localization of light in a disordered medium, *Nature* **390**, 671 (1997).

[121] A. A. Chabanov, M. Stoytchev, and A. Z. Genack, Statistical signatures of photon localization, *Nature* **404**, 850 (2000).

[122] T. Schwartz, G. Bartal, S. Fishman, and M. Segev, Transport and Anderson localization in disordered two-dimensional photonic lattices, *Nature* **446**, 52 (2007).

[123] R. Zallen and H. Scher, Percolation on a continuum and the localization-delocalization transition in amorphous semiconductors, *Phys. Rev. B* **4**, 4471 (1971).

[124] A. L. Efros, Metal-non-metal transition in heterostructures with thick spacer layers, *Solid State Commun.* **70**, 253 (1989).

[125] E. Abrahams, P. W. Anderson, D. C. Licciardello, and T. V. Ramakrishnan, Scaling theory of localization: absence of quantum diffusion in two dimensions, *Phys. Rev. Lett.* **42**, 673 (1979).

[126] E. Abrahams, S. V. Kravchenko, and M. P. Sarachik, Metallic behavior and related phenomena in two dimensions, *Rev. Mod. Phys.* **73**, 251 (2001).

[127] S. V. Kravchenko and M. P. Sarachik, Metal-insulator transition in two-dimensional electron systems, *Rep. Prog. Phys.* **67**, 1 (2004).

[128] S. Das Sarma and E. H. Hwang, The so-called two dimensional metal-insulator transition, *Solid State Commun.* **135**, 579 (2005).

[129] J. M. Baranowski and M. Grynberg, in *Handbook on Semiconductors*, Vol. 1, edited by P. T. Landsberg (Elsevier, Amsterdam, 1992), Chap. 5.

[130] P. Van Mieghem, Theory of band tails in heavily doped semiconductors, *Rev. Mod. Phys.* **64**, 755 (1992).

[131] B. E. Kane, A silicon-based nuclear spin quantum computer, *Nature* **393**, 133 (1998).

[132] G. Bastard, Hydrogenic impurity states in quantum well: A simple model, *Phys. Rev. B* **24**, 4714 (1981).

[133] S. Chaudhuri and K. K. Bajaj, Effect of nonparabolicity on the energy levels of hydrogenic donors in GaAs-$Ga_{1-x}Al_xAs$ quantum-well structures, *Phys. Rev. B* **29**, 1803 (1984).

[134] C. Priester, G. Allan, and M. Lannoo, Resonant impurity states in quantum-well structures, *Phys. Rev. B* **29**, 3408 (1984).

[135] A. Blom, M. A. Odnoblyudov, I. N. Yassievich, and K.-A. Chao, Donor states in modulation-doped Si/SiGe heterostructures, *Phys. Rev. B* **68**, 165338 (2003).

[136] B. S. Monozon and P. Schmelcher, Resonant impurity and exciton states in a narrow quantum well, *Phys. Rev. B* **71**, 085302 (2005).

[137] N. C. Jarosik, B. D. McCombe, B. V. Shanabrook, J. Comas, J. Ralston, and G. Wicks, Binding of shallow donor impurities in quantum-well structures, *Phys. Rev. Lett.* **54**, 1283 (1985).

[138] B. V. Shanabrook, J. Comas, T. A. Perry, and R. Merlin, Raman scattering from electrons bound to shallow donors in GaAs-$Al_xGa_{1-x}As$ quantum-well structures, *Phys. Rev. B* **29**, 7096 (1984).

[139] T. A. Perry, R. Merlin, B. V. Shanabrook, and J. Comas, Observation of resonant impurity states in semiconductor quantum-well structures, *Phys. Rev. Lett.* **54**, 2623 (1985).

[140] B. V. Shanabrook and J. Comas, Photoluminescence from spike doped hydrogenic donors in $Al_{0.3}Ga_{0.7}As$-GaAs quantum wells, *Surf. Sci.* **142**, 504 (1984).

[141] B. V. Shanabrook, The properties of hydrogenic donors confined in GaAs-AlGaAs multiple quantum wells, *Surf. Sci.* **170**, 449 (1986).

[142] D. C. Reynolds, K. K. Bajaj, C. W. Litton, P. W. Yu, W. T. Masselink, R. Fischer, and H. Morkoc, Sharp-line photoluminescence spectra from GaAs-GaAlAs multiple-quantum-well structures, *Phys. Rev. B* **29**, 7038 (1984).

[143] X. Liu, A. Petrou, B. D. McCombe, J. Ralston, and G. Wicks, Photoluminescence study of confined donors in GaAs/$Al_xGa_{1-x}As$ quantum wells, *Phys. Rev. B* **38**, 8522 (1988).

[144] X. L. Yang, S. H. Guo, F. T. Chan, K. W. Wong, and W. Y. Ching, Analytic solution of a two-dimensional hydrogen atom. I. Nonrelativistic theory, *Phys. Rev. A* **43**, 1186 (1991).

[145] A. M. Yakunin, A. Yu. Silov, P. M. Koenraad, J. H. Wolter, W. Van Roy, J. De Boeck, J.-M. Tang, and M.-E. Flatté, Spatial structure of an individual Mn acceptor in GaAs, *Phys. Rev. Lett.* **92**, 216806 (2004).

[146] G. Mahieu, B. Grandidier, D. Deresmes, J. P. Nys, D. Stiévenard, and Ph. Ebert, *Phys. Rev. Lett.* **94**, 026407 (2005).

[147] A. M. Yakunin, A. Yu. Silov, P. M. Koenraad, J.-M. Tang, M.-E. Flatté, J.-L. Primus, W. Van Roy, J. De Boeck, A. M. Monakhov, K. S. Romanov, I. E. Panaiotti, and N. S. Averkiev, Warping a single Mn acceptor wavefunction by straining the GaAs host, *Nature Mat.* **6**, 512 (2007).

[148] G. W. Gobeli and F. G. Allen, Photoelectric properties of cleaved GaAs, GaSb, InAs, and InSb surfaces; Comparison with Si and Ge, *Phys. Rev.* **137**, A245 (1965).

[149] N. W. Ashcroft and N. D. Mermin, *Solid State Physics* (Brooks/Cole, 1976), Chaps. 12 and 29.

[150] C. Metzner, M. Hofmann, and G. H. Döhler, Intersubband transitions of a quasi-two-dimensional electron gas in the strong disorder regime, *Phys. Rev. B* **58**, 7188 (1998).

[151] J. Bardeen, Tunnelling from a many-particle point of view, *Phys. Rev. Lett.* **6**, 57 (1961).

[152] J. Tersoff and D. R. Hamann, Theory and application for the scanning tunneling microscope, *Phys. Rev. Lett.* **50**, 1998 (1983).

[153] J. Tersoff and D. R. Hamann, Theory of the scanning tunneling microscope, *Phys. Rev. B* **31**, 805 (1985).

[154] N. D. Lang, Spectroscopy of single atoms in the scanning tunneling microscope, *Phys. Rev. B* **34**, 5947 (1986).

[155] R. M. Feenstra, Tunneling spectroscopy of the (110) surface of direct-gap III-V semiconductors, *Phys. Rev. B* **50**, 4561 (1994).

[156] C. Hilsum and A. C. Rose-Innes, *Semiconducting III-V compounds* (Pergamon Press, Oxford, 1961).

[157] E. O. Kane, Band structure of indium antimonide, *J. Phys. Chem. Solids* **1**, 249 (1957).

[158] E. O. Kane, in *Semiconductors and semimetals*, edited by R. K. Willardson and A. C. Beer (Academic, New York, 1975), Vol. 1, Chap. 3.

[159] J. Bardeen, Surface states and rectification at a metal semi-conductor contact, *Phys. Rev.* **71**, 717 (1947).

[160] V. Heine, Theory of surface states, *Phys. Rev.* **138**, A1689 (1965).

[161] J. Tersoff, Schottky barrier heights and the continuum of gap states, *Phys. Rev. Lett.* **52**, 465 (1984).

[162] H. Hasegawa and H. Ohno, Unified disorder induced gap state model for insulator - semiconductor and metal - semiconductor interfaces, *J. Vac. Sci. Technol. B* **4**, 1130 (1986).

[163] W. Walukiewicz, Mechanism of Fermi-level stabilization in semiconductors, *Phys. Rev. B* **37**, 4760 (1988).

[164] G. M. Guichar, C. A. Sebenne, and G. A. Garry, Intrinsic and defect-induced surface states of cleaved GaAs(110), *Phys. Rev. Lett.* **37**, 1158 (1976).

[165] L. M. Terman, An investigation of surface states at silicon/silicon oxide interface employing metal-oxide-silicon diodes, *Solid State Electron.* **5**, 285 (1962).

[166] M. Tabib-Azar, S. Kang, A. N. MacInnes, M. B. Power, A. R. Barron, P. P. Jenkins, and A. F. Hepp, Electronic passivation of n- and p-type GaAs using chemical vapor deposited GaS, *Appl. Phys. Lett.* **63**, 625 (1993).

[167] P. P. Jenkins, A. N. MacInnes, M. Tabib-Azar, and A. R. Barron, Gallium arsenide transistors: realization through a molecularly designed insulator, *Science* **263**, 1751 (1994).

[168] M. Passlack, M. Hong, J. P. Mannaerts, R. L. Opila, S. N. G. Chu, N. Moriya, F. Ren, and J. R. Kwo, Low D_{it}, thermodynamically stable Ga_2O_3 - GaAs interfaces: fabrication, characterization, and modeling, *IEEE Trans. Electron. Devices* **44**, 214 (1997).

[169] M. Hong, J. Kwo, A. R. Kortan, J. P. Mannaerts, and A. M. Sergent, Epitaxial cubic gadolinium oxide as a dielectric for gallium arsenide passivation, *Science* **283**, 1897 (1999).

[170] R. M. Feenstra and J. A. Stroscio, Tunneling spectroscopy of the GaAs(110) surface, *J. Vac. Sci. Technol. B* **5**, 923 (1987).

[171] R. Dombrowski, Chr. Steinebach, Chr. Wittneven, M. Morgenstern, and R. Wiesendanger, Tip-induced band bending by scanning tunneling spectroscopy of the states of the tip-induced quantum dot on InAs(110), *Phys. Rev. B* **59**, 8043 (1999).

[172] R. M. Feenstra, G. Meyer, F. Moresco, and K. H. Rieder, Low-temperature scanning tunneling spectroscopy of *n*-type GaAs(110) surfaces, *Phys. Rev. B* **66**, 165204 (2002).

[173] R. M. Feenstra, Electrostatic potential for a hyperbolic probe tip near a semiconductor, *J. Vac. Sci. Technol. B* **21**, 2080 (2003).

[174] J. D. Jackson, *Classical electrodynamics*, 2nd edition (Wiley, New York, 1975).

[175] Y. Yafet, R. W. Keyes, and E. N. Adams, Hydrogen atom in a strong magnetic field, *J. Phys. Chem. Solids*, **1**, 137 (1956).

[176] R. W. Keyes and R. J. Sladek, Effect of a magnetic field on donor impurity levels in InSb, *J. Phys. Chem. Solids*, **1**, 143 (1956).

List of publications

The work presented in this dissertation has led to the following publications:

- S. Perraud, K. Kanisawa, Z. Z. Wang, and T. Fujisawa, Direct measurement of the binding energy and Bohr radius of a single hydrogenic defect in a semiconductor quantum well (submitted to *Phys. Rev. Lett.*).

- S. Perraud, K. Kanisawa, Z. Z. Wang, and T. Fujisawa, Imaging the percolation of localized states in a multisubband two-dimensional electronic system subject to a disorder potential, *Phys. Rev. B* **76**, 195333 (2007).

- S. Perraud, K. Kanisawa, Z. Z. Wang, and Y. Hirayama, Unpinning of the Fermi level at (111)A clean surfaces of epitaxially grown n-type $In_{0.53}Ga_{0.47}As$, *Appl. Phys. Lett.* **89**, 192110 (2006).

- S. Perraud, K. Kanisawa, Z. Z. Wang, and T. Fujisawa, Bound states induced by a single donor in a semiconductor quantum well: a scanning tunneling spectroscopy study, *Physica E* (in press).

- S. Perraud, K. Kanisawa, Z. Z. Wang, and Y. Hirayama, Dramatic dependence of the Fermi level pinning strength on crystal orientation at clean surfaces of n-type $In_{0.53}Ga_{0.47}As$ grown by molecular beam epitaxy, *J. Cryst. Growth* **301-302**, 148 (2007).

- S. Perraud, K. Kanisawa, Z. Z. Wang, and Y. Hirayama, Low-temperature scanning tunneling spectroscopy of two dimensional electron systems confined in semiconductor heterostructures, *J. Phys.: Conf. Ser.* **61**, 926 (2007).

In addition, a collaboration with Kyoichi Suzuki on the study of InAs/GaSb heterostructures has led to the following publications:

- K. Suzuki, K. Kanisawa, C. Janer, S. Perraud, K. Takashina, T. Fujisawa, and Y. Hirayama, Spatial imaging of two-dimensional electronic states in semiconductor quantum wells, *Phys. Rev. Lett.* **98**, 136802 (2007).

- K. Suzuki, K. Kanisawa, S. Perraud, M. Ueki, K. Takashina, and Y. Hirayama, Observation of subband standing waves in superlattices by low-temperature scanning tunneling spectroscopy, *J. Appl. Phys.* **101**, 081705 (2007).

- K. Suzuki, K. Kanisawa, S. Perraud, M. Ueki, K. Takashina, and Y. Hirayama, Imaging of subbands in InAs/GaSb double quantum wells by low-temperature scanning tunneling spectroscopy, *J. Cryst. Growth* **301-302**, 97 (2007).

- K. Suzuki, K. Kanisawa, S. Perraud, M. Ueki, K. Takashina, and Y. Hirayama, Imaging of interference between incident and reflected electron waves at an InAs/GaSb heterointerface by low-temperature scanning tunneling spectroscopy, *Jpn. J. Appl. Phys.* **46**, 2618 (2007).

- K. Suzuki, K. Kanisawa, S. Perraud, M. Ueki, K. Takashina, and Y. Hirayama, Imaging of electron standing waves in InAs/GaSb superlattices by low-temperature scanning tunneling spectroscopy, *Phys. Stat. Sol. (c)* **3**, 643 (2006).